A Diffusion-Viscous Analysis and Experimental Verification of the Drying Behavior in Nanosilver-Enabled Low-Temperature Joining Technique

Kewei Xiao

Dissertation submitted to the faculty of the Virginia Polytechnic Institute and State University in partial fulfillment of the requirements for the degree of

Doctor of Philosophy

In

Materials Science and Engineering

Guo-Quan Lu, Chair

Alexander O. Aning

Gary R. Pickrell

Khai D. Ngo

12/05/2013

Blacksburg, VA

Keywords: low-temperature joining, drying of silver paste, internal stress, bond-line defect formation.

Copyright 2013, Kewei Xiao

A Diffusion-Viscous Analysis and Experimental Verification of the Drying Behavior in Nanosilver-Enabled Low-Temperature Joining Technique

Kewei Xiao

ABSTRACT

The low-temperature joining technique (LTJT) by silver sintering is being implemented by major manufacturers of power electronics devices and modules for bonding power semiconductor chips. A common die-attach material used with LTJT is a silver paste consisting of silver powder (micron- or nano-size particles) mixed in organic solvent and binder formulation. It is believed that the drying of the paste during the bonding process plays a critical role in determining the quality of the sintered bond-line. In this study, a model based on the diffusion of solvent molecules and viscous mechanics of the paste was introduced to determine the stress and strain states of the silver bond-line. A numerical simulation algorithm of the model was developed and coded in the C++ programming language. The numerical simulation allows determination of the time-dependent physical properties of the silver bond-line as the paste is being dried with a heating profile. The properties studied were solvent concentration, weight loss, shrinkage, stress, and strain. The stress is the cause of cracks in the bond-line and bond-line delamination. The simulated results were verified by complementary experiments in which the formation of cracks in bond-line and interface delamination was observed during the pressure-free drying of a die-attach nanosilver paste. Furthermore, the

important drying parameters, such as drying pressure, low temperature drying time and temperature ramp rate of nanosilver LTJT process, are experimentally studied and analyzed with the numerical simulation. The simulated results were consistent with the experimental findings that the quality of sintered silver bond-line increases with increasing external drying pressure, with increasing low temperature drying time, and with decreasing temperature ramp rate. The insight offered by this modeling study can be used to optimize the process profile that enable pressure-free, low-temperature sintering of the die-attach material to significantly lower the cost of implementing the LTJT in manufacturing.

Acknowledgements

I own sincere appreciation to my advisor and committee chair: Dr. Guo-Quan Lu, for his valuable time, energy, advice, guidance, and support throughout my research. His smart ideas and brilliant suggestions always enlighten me when I come to a technical problem, and he sets a good example to me by his professional attitude to academic research as well as his expertise of practical application. Without his guidance, support, and encouragement, this thesis would never come into existence.

I am sincerely grateful to my doctoral committee members: Dr. Khai Ngo, Dr. Alex Aning, and Dr. Gary Pickrell, for their valuable time, supports and help.

Special thanks to Dr. Guangyin Lei, Dr. Jesus Calata, and Dr. Xiao Cao, for the sharing of expertise, academic support, enlightening discussion and great friendship. I would also like to thank my colleagues in the research group of electronics packaging: Yiying Yao, Li Jiang, David Berry, Hanguang Zheng, Yi Yan, Yunhui Mei, Tao Wang, Meihua Zhao, Tao Tao, Woochan Kim, Jayashree Vijay, and Mudassar Khatib, for their helpful discussion and great friendship.

I would like to thank Dr. Wenli Zhang at packaging lab of Center for Power Electronics Systems (CPES), Dr. Stephen McCartney and Dr. Jerry Hunter at Nanoscale Characterization and Fabrication Laboratory (NCFL) of Institute for Critical Technology and Applied Science (ICTAS), for their advice, suggestions, and technical assistance in experiments.

It has been a great pleasure to study and work in MSE department and CPES. I would acknowledge to the administrative and management staff, Ms. Kimberry Grandstaff, Ms. Amy Hill, Ms. LeeAnn Ellis, and Ms. Teresa Shaw for their countless help. I would also

acknowledge to the National Science Foundation for the financial support to my research (Award Number CBET-1048621).

Finally, I am deeply indebted to my parents: Dr. Xiaoting Xiao and Ms. Yijuan Liao, for their unconditional support, understanding, encouragement and love. They are always providing me the strength to realize the important goals in life.

Table of Contents

Acknowledgements iv

Table of Contents vi

List of Figures x

List of Tables xvii

Chapter 1. Introduction 1

1.1. Overview of semiconductor chip attachment techniques 1

1.1.1. Solder reflow 1

1.1.2. Electrically conductive adhesives 4

1.1.3. Low temperature joining technique 6

1.2. Current concerns in LTJT 9

1.2.1. Pressure-aided heating process of LTJT 9

1.2.2. Drying process of LTJT 9

1.3. Theories to analyze the drying behavior of LTJT 11

1.3.1. Liquid removal during drying 11

1.3.2. Stress induced by drying 12

1.4. Objectives and significance of the study 13

1.5. Structure of the dissertation 13

1.6. Publications 15

Chapter 2. Modeling of the drying behavior in nanosilver LTJT 17

2.1. Introduction 17

2.2. Model of nanosilver paste drying 17

2.2.1. Composition of nanosilver paste 17

2.2.2. Viscous model for stress analysis 21
2.2.3. Kinetics of solvent movement in paste 26
2.2.4. Internal stresses evolution of nanosilver paste during drying 29
2.3. Algorithm and flow chat for stress evolution 30
2.4. Summary 36
Chapter 3. Experiments verification of the predicted drying behavior in nanosilver LTJT 37
3.1. Introduction 37
3.2. Weight loss profile of nanosilver paste 37
3.3. Shrinkage profile of nanosilver paste 40
3.4. Stress evolution of nanosilver paste in the chip attachment 42
3.5. Summary 46
Chapter 4. Design of experiments (DOE) study on nanosilver LTJT 47
4.1. Introduction 47
4.2. Experimental procedures 47
4.2.1. Sample preparation 47
4.2.2. Die-shear testing 51
4.2.3. X-ray CT characterization 52
4.3. Results and discussion 54
4.3.1. Bonding strength of sintered silver joints 54
4.3.2. Structure of the sintered silver bond-line 57
4.3.3. Development of nanosilver LTJT process 64
4.4. Summary 65

Chapter 5. Effect of external applied pressure during drying on sintered silver bond-line 66
5.1. Introduction 66
5.2. Experimental procedures 66
5.2.1. Sample Preparation 66
5.2.2. Die-shear testing 68
5.2.3. Microstructure Characterization 68
5.2.4. Numerical simulation of stress evolution 69
5.3. Results and Discussion 70
5.3.1. Die-shear strength 70
5.3.2. Microstructure of sintered silver joint 70
5.3.3. Simulation of internal stress evolution 78
5.4. Summary 82
Chapter 6. Effects of temperature ramp rate and drying time on sintered silver bond-line 84
6.1. Introduction 84
6.2. Experimental procedures 84
6.2.1. Sample preparation 84
6.2.2. Die-shear testing 88
6.2.3. Numerical simulation of the stress and strain evolution 89
6.3. Results and discussion 90
6.3.1. Die-shear strength of chip attachments 90
6.3.2. Simulation of internal stress and shrinkage of nanosilver paste 93

6.4. Summary ... 107
Chapter 7. Summary and conclusions ... 109
7.1. Summary of the study ... 109
7.2. Suggestions for future work ... 111
References ... 113
Appendix A: C++ code and input format for numerical simulation of nanosilver paste drying in the chip attachment ... 125
C++ source code of the main modules ... 125
Input file format ... 130
Appendix B: Mechanical properties and creep behavior of sintered nanosilver joint layer ... 133
Experimental Procedures ... 133
Experimental Results ... 135
Stress-strain curves at different temperatures ... 135
Creep behavior of sintered paste at different temperatures ... 136
Conclusions ... 138
Appendix C: Nondestructive characterization of the bonding of silicon device attachments by curvature measurement ... 140
Theory ... 140
Experiments ... 142

List of Figures

Fig. 1.1. Recommended heating profile for 37Pb63Sn solder. 2

Fig. 1.2. Cross-sectional image of 37Pb63Sn solder bond-line after thermal cycling........ 3

Fig. 1.3. Schematic illustration of (a) isotropic conductive adhesives and (b) anisotropic conductive adhesives. 5

Fig. 1.4. Schematic of heating profile of LTJT process... 7

Fig. 1.5. Cross-sectional image of sintered silver bond-line after thermal cycling. 8

Fig. 1.6. X-ray transmission image of a chip attachment (a) after drying with an inappropriate profile (direct heated at 180°C for 30 minutes), and (b) followed by sintering at 275°C for 30 minutes with an uniaxial pressure of 3 MPa. 10

Fig. 2.1. Schematic of composition evolution of nanosilver paste during drying process. 18

Fig. 2.2. Relationship between volume ratio (V/V^0) and solvent concentration (C_S/C_S^0).20

Fig. 2.3. Schematic of (a) a unit cell in at position (x, y, z) in paste, and (b) the principle stresses and principle strains generated in the unit cell. 21

Fig. 2.4. Load condition of chip, showing external applied pressure P_{apply} and reaction stress of paste σ_z 23

Fig. 2.5. Curve fitting of viscosity-concentration data. 25

Fig. 2.6. Paste deposits between the chip and the substrate, which causes solvent only leaving from the edges. 26

Fig. 2.7. TGA plot of nanosilver paste under early drying condition at heating rate of 5 ℃/min. 28

Fig. 2.8. Curve fitting for the rate of weight loss of solvent in the paste.......................... 29

Fig. 2.9. Schematic of stress evolution and defect formation caused by the drying of nanosilver paste in constrained chip attachment. 30
Fig. 2.10. Meshing of paste structure for numerical simulation. 31
Fig. 2.11. Flow chart of the internal stress evolution outputs with different drying profile file inputs. 33
Fig. 2.12. Flow chart for new concentration of solvent calculation for a small time increment dt. 34
Fig. 2.13. Flow chart for internal stresses calculation at time t. 35
Fig. 3.1. Heating profiles for weight loss measurements. Profile 1 is constant ramp rate heating and profile 2 is ramp-soak combined heating. 38
Fig. 3.2. Experimental and simulated weight loss profile for nanosilver paste in chip attachment with 5 mm chip length at heating profile 1 (constant heating rate). 39
Fig. 3.3. Experimental and simulated weight loss profile for nanosilver paste in chip attachment with 5 mm chip length at heating profile 2 (ramp-soak heating). 39
Fig. 3.4. Experimental results of thickness shrinkage for nanosilver paste in 1×1 mm^2, 3×3 mm^2 and 5×5 mm^2 chip attachments with heating profile 2 (ramp-soak heating). 41
Fig. 3.5. Simulation results of thickness shrinkage of nanosilver paste in 1×1 mm^2, 3×3 mm^2, and 5×5 mm^2 chip attachments with heating profile 2 (ramp-soak heating). 42
Fig. 3.6. Distribution of vertical internal stress of nanosilver paste in a 10×10 mm^2 chip attachment at 180 ℃ drying under zero external pressure for (a) 0 min, (b) 20 min, (c) 40 min, (d) 60 min, (e) 80 min, and (f) 100 min. 44

Fig. 3.7. Distribution of x-y in-plane internal stress of nanosilver paste in a 10 × 10 mm^2 chip attachment at 180 ℃ drying under zero external pressure for (a) 0 min, (b) 20 min, (c) 40 min, (d) 60 min, (e) 80 min, and (f) 100 min. 44

Fig. 3.8. Nanosilver paste under a glass chip showing defect formation during 180 ℃ drying. (a)-(f) are from the beginning to the end of drying, respectively. 45

Fig. 4.1. Left is the schematic of samples structure, and right is the top view of a fabricated sample. 48

Fig. 4.2. Flowchart of the double print process for the fabrication of test samples under different applied pressures and sintering times. 49

Fig. 4.3. Heating profiles for nanosilver 1st layer drying and final drying/sintering in attachment process. 50

Fig. 4.4. The schematic of chip attachment in fixture for die-shear testing. 51

Fig. 4.5. (a) is the fixture to hold and shear chip attachment samples, and (b) is ComTen 95 series tester for die-shearing. 52

Fig. 4.6. (a) is the MicroXCT 400 (Xradia) equipment used for X-ray imaging of sintered samples, and (b) is the major components inside X-ray equipment chamber. .. 53

Fig. 4.7. Plot of average die-shear strength corresponding to different drying time, drying pressure, sintering time and sintering pressure, showing the main effect of each factor on die-shear strength. 55

Fig. 4.8. Interaction plot between factors of drying time ($\mathbf{t_D}$), drying pressure ($\mathbf{P_D}$), sintering time ($\mathbf{t_S}$) and sintering pressure ($\mathbf{P_S}$), in which no strong interaction was detected between any two process parameters. 56

Fig. 4.9. X-ray transmission images of sintered sample from groups A to H, showing different microstructures of sintered silver layers: few tiny cracks are showing in group D and H; big cracks and voids are showing in group A, and F; moderate cracks are showing in group B, C, E, and G. 62

Fig. 4.10. X-ray reconstructed images of sintered silver joint layers from samples in (a) group F, (b) group E and (c) group E, showing big cracks/voids, moderate cracks and tiny cracks/voids, respectively. Light color regions in the images represent silver layers and dark color regions represent voids and cracks. 64

Fig. 5.1. Heating profile of chip attachment after chip mounting to substrate. 67

Fig. 5.2. Hot press used for applying uniaxial pressure during assembly heating........... 68

Fig. 5.3. Die-shear strength of samples fabricated under different drying pressures. Drying time and sintering time were set for 5 minutes and 10 minutes, respectively. No pressure was applied during the sintering stage. 70

Fig. 5.4. X-ray transmission images of sintered sample under different external applied drying pressures of (a) 0 MPa, (b) 1 MPa, (c) 3 MPa, (d) 5 MPa, and (e) 10 MPa. 73

Fig. 5.5. SEM images of corss-sectioned sintered silver joints fabricated with (a) zero drying pressure, (b) 3 MPa drying pressure, and (c) 10 MPa drying pressure. . 75

Fig. 5.6. Relative density of sintered nanosilver joint vs. drying pressure. 76

Fig. 5.7. Distribution of x-y in-plane internal stress of nanosilver paste between 10 $\times$ 10 mm^2 chip and substrate at 180 ℃ drying under 0 to 10 MPa external pressure for 1 to 5 minutes. 79

Fig. 5.8. Distribution of vertical internal stress of nanosilver paste between 10 × 10 mm^2 chip and substrate at 180 ℃ drying under 0 to 10 MPa external pressure for 1 to 5 minutes. 80

Fig. 6.1. (a) Schematic of thickness control for initial nanosilver paste bond-line and (b) the custom built thickness controller setup. 86

Fig. 6.2. Schematic of heating profile for nanosilver chip attachment fabrication 87

Fig. 6.3. Nordson DAGE 4000 Multipurpose Bondtester. 88

Fig. 6.4. Die-shear strength vs. temperature ramp rate for (a) 3 × 3 mm^2 and (b) 6 × 6 mm^2 chip attachments. 91

Fig. 6.5. The top plot is the maximum x-y in-plane internal stress and maximum vertical internal stress of nanosilver paste in a 3 × 3 mm^2 chip attachment during heating profile A (heat from room temperature to 180°C with temperature ramp rate 1°C/min). The bottom figures show the distribution of internal stresses of nanosilver paste at the time points of (I), (II), (III), and (IV). 94

Fig. 6.6. The top plot is the maximum x-y in-plane internal stress and maximum vertical internal stress of nanosilver paste in a 3 × 3 mm^2 chip attachment during heating profile B (heat from room temperature to 180°C with temperature ramp rate of 3°C/min, and hold at 180°C for 104 minutes). The bottom figures show the distribution of internal stresses of nanosilver paste at the time points of (I), (II), (III), and (IV). 95

Fig. 6.7. The top plot is the maximum x-y in-plane internal stress and maximum vertical internal stress of nanosilver paste in a 3 × 3 mm^2 chip attachment during heating profile C (heat from room temperature to 180°C with temperature ramp rate of

7.5°C/min, and hold at 180°C for 135 minutes). The bottom figures show the distribution of internal stresses of nanosilver paste at the time points of (I), (II), (III), and (IV). 96

Fig. 6.8. The top plot is the maximum x-y in-plane internal stress and maximum vertical internal stress of nanosilver paste in a 3 $\times$3 mm^2 chip attachment during heating profile D (after room temperature treatment for 24 hours, then heat from room temperature to 180°C with temperature ramp rate of 3°C/min, and hold at 180°C for 104 minutes). The bottom figures show the distribution of internal stresses of nanosilver paste at the time points of (I), (II), (III), and (IV)........................ 97

Fig. 6.9. The top plot is the maximum x-y in-plane internal stress and maximum vertical internal stress of nanosilver paste in a 6 $\times$6 mm^2 chip attachment during heating profile E (heat from room temperature to 180°C with temperature ramp rate 1°C/min). The bottom figures show the distribution of internal stresses of nanosilver paste at the time points of (I), (II), (III), and (IV). 100

Fig. 6.10. The top plot is the maximum x-y in-plane internal stress and maximum vertical internal stress of nanosilver paste in a 6 $\times$6 mm^2 chip attachment during heating profile F (heat from room temperature to 180°C with temperature ramp rate of 3°C/min, and hold at 180°C for 104 minutes). The bottom figures show the distribution of internal stresses of nanosilver paste at the time points of (I), (II), (III), and (IV). 101

Fig. 6.11. The top plot is the maximum x-y in-plane internal stress and maximum vertical internal stress of nanosilver paste in a 6 $\times$6 mm^2 chip attachment during heating profile G (heat from room temperature to 180°C with temperature ramp rate of

7.5°C/min, and hold at 180°C for 135 minutes). The bottom figures show the distribution of internal stresses of nanosilver paste at the time points of (I), (II), (III), and (IV). 102

Fig. 6.12. The top plot is the maximum x-y in-plane internal stress and maximum vertical internal stress of nanosilver paste in a 6 $\times$ 6 mm^2 chip attachment during heating profile H (after room temperature treatment for 24 hours, then heat from room temperature to 180°C with temperature ramp rate of 3°C/min, and hold at 180°C for 104 minutes). The bottom figures show the distribution of internal stresses of nanosilver paste at the time points of (I), (II), (III), and (IV)...................... 103

Fig. 6.13. Die-shear strength (experiment) vs. relative green density (simulation) of nanosilver chip attachment with different drying parameter combinations (case A to H). 107

Fig. B.1. Drying and sintering profile of open-faced nanosilver paste.......................... 133

Fig. B.2. Sintered nanosilver paste films on alumina substrate, the inset shows the final samples used in the mechanical properties testing. 134

Fig. B.3. Stress-Strain relationships at different temperatures. 135

Fig. B.4. Young's modulus of sintered silver layers at different temperatures. 136

Fig. B.5. Ultimate stress and strain of sintered silver layers at different temperatures. . 136

Fig. B.6. Strain-time curve during creep under 10MPa constant stress at 75 ℃ 137

Fig. B.7. Curve fitting for determining the activation energy of sintered silver layer.... 138

Fig. C.1. Structure of a silicon chip bonded on a DBC substrate. 142

Fig. C.2. Correlation of curvature with die-shear strength. 144

List of Tables

Table 1.1: Comparison of processing parameters and physical properties of various attachment materials. 6

Table 2.1: Relationship between viscosity E and concentration of solvent of paste C_S 24

Table 4.1: Designed combinations of process parameters. 51

Table 4.2: Die-shear strengths of samples fabricated under different process profiles. ... 54

Table 4.3: Analysis of Variance (ANOVA) computation of the significance of individual factors and interactions. 57

Table 5.1: Input parameters of nanosilver chip attachment during drying 69

Table 5.2: Minimum and maximum x-y in-plane internal stress (in MPa) of the paste in the chip attachment during drying under different external applied pressures. 81

Table 5.3: Minimum and maximum vertical internal stress (in MPa) of the paste in the chip attachment during drying under different external applied pressures. 82

Table 6.1: Parameter combinations of different pre-drying time, temperature ramp rate and holding time in drying stage. 87

Table 6.2: Input parameters of nanosilver chip attachment during drying. 89

Table 6.3: Die-shear strength of nanosilver chip attachments fabricated with different heating parameter combinations. 90

Table 6.4: Simulated final shrinkage with estimated green density of nanosilver chip attachments after drying with different heating parameter combinations. ... 105

Table B.1: Data from constant stress tension creep tests of sintered nanosilver layers.. 137

Table C.1: Curvature of silicon attachments and die-shear strength of alumina attachments with different fabricating process parameters........................... 143

Chapter 1. Introduction

1.1. Overview of semiconductor chip attachment techniques

Semiconductor chip attachment is an important process in electronics packaging. The joint layer, which is often referred to as the bond-line, serves as mechanical bond, electrical connection and heat transfer media. Therefore, the quality of bond-line in the chip attachment is crucial to the performance and reliability of electronic modules.

Currently, there are three major chip attachment materials/techniques: solder reflow, electrically conductive adhesive and low temperature joining technique.

1.1.1. Solder reflow

Solders are metal alloys that consist of two or more metallic elements. In the soldering process, the solder either in the paste form or in the preform form is placed between the chip and the substrate which need to be bonded. The assembly will then be heated with a specific designed heating profile. With the heat treatment, solder will melt to liquid phase and wet the surfaces that need to be bonded. Intermetallic phases are usually formed at the interfaces between the chip, the solder joint and the substrate [1-3]. After cooling down, the bond can be formed.

The most widely used solder material in electronics packaging is a lead-tin solder (37Pb63Sn). And this solder is a standard to which all other interconnect materials are compared. 37Pb63Sn solder has a melting point of 183°C, which is a mild temperature for processing. A typical heating profile of 37Pb63Sn solder is shown in Fig. 1.1 [4, 5]. Because of the relatively low cost of solder materials and simple processing method, 37Pb63Sn solder is commonly used in traditional electronics industries.

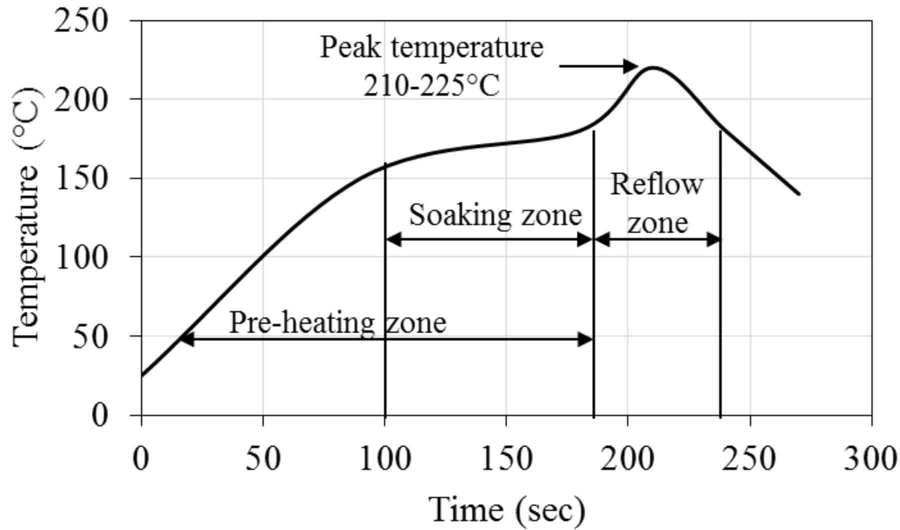

Fig. 1.1. Recommended heating profile for 37Pb63Sn solder.

Another commonly used solder is 95Pb5Sn. 95Pb5Sn is a lead-based solder which melts at the temperature of 300°C. The high melting point of the solder indicates that once the joint is formed, it can undergo at relatively high temperature without obvious decrease of performance, i.e., the mechanical properties and electrical properties. Therefore, 95Pb5Sn is mainly used in high temperature applications of which requires operation temperature of electronic above 200°C, such as under-the-hood automotive, air-craft, aerospace, and well-logging industries.

However, as the large amount of lead usage raises serious environment concerns, the use of lead-based solder is being restricted. Lead-free solder is becoming the first-hand choice in varies of electronics industries. Most common lead-free solder are tin-based, with potential ternary additions of antimony, silver, bismuth, or copper [6-8]. The typical melting temperature of lead-free solders ranges from 210℃ to 234℃, which is comparable to lead-based solders. The mechanical and electrical performances of the

lead-free solder joints are similar to that of lead-tin solders joints, and lead-free solder joints performs slightly higher thermal reliability than that of lead-tin solder joints [8]. For both lead-based and lead-free soldering, the alloy starts out as spheres immersed in a flux. The flux serves to clean the surfaces to be bonded before the solder particles melt. The bond is established through the formation of intermetallic compounds in the alloy and takes place relatively quickly. The entire reflow process can be completed in a few minutes. The biggest advantage of soldering is the low cost of materials and simple bonding process. However, the formation of an intermetallic layer during soldering is a big concern. Since intermetallics are usually much harder than the solder, large thermal stresses due to the mismatch of coefficient of thermal expansion will be induced during thermal cycling. Research indicates that solder joints usually fail at the interface between the intermetallic compound and the solder alloy [9-11]. Fig. 1.2 shows a typical failure at the interface between the solder and the substrate.

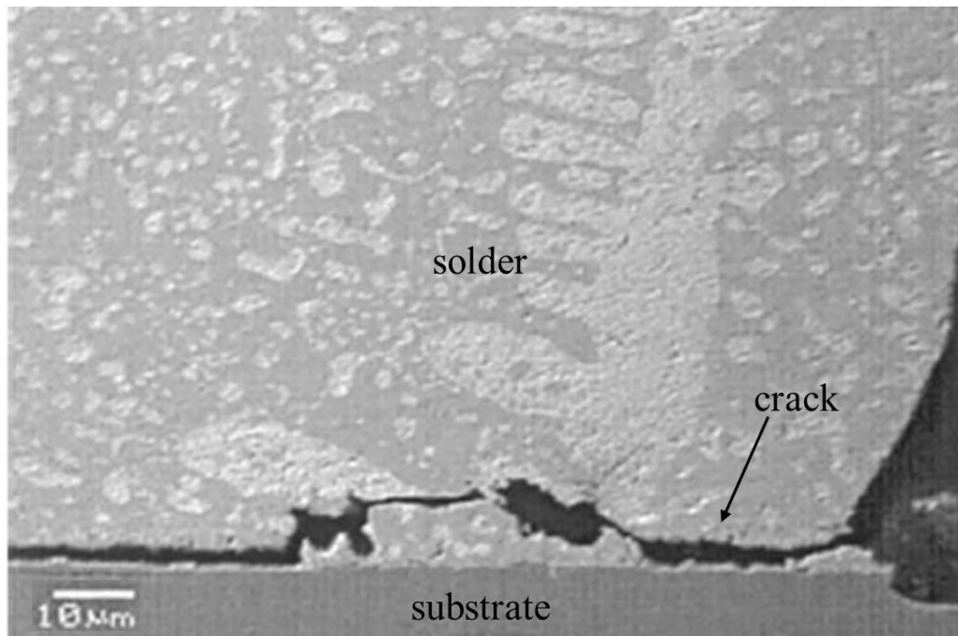

Fig. 1.2. Cross-sectional image of 37Pb63Sn solder bond-line after thermal cycling.

1.1.2. Electrically conductive adhesives

An electrically conductive adhesive (ECA) is a glue that offers a relatively low temperature, mild processing condition for electronics attachment. Because of the increasing environment concern, the use of the lead-based solders has been constrained, which has stimulated the development of the environment friendly alternatives ECAs [12, 13]. Apart from the environmental concern, ECAs offer advantages over conventional solder technology such as, lower sensitivity to thermo-mechanical stresses, and higher flexibility [14].

An ECA consists of a dielectric curable polymer resin (commonly an epoxy) and metallic conductive particles. The polymer resin is an adhesive material which provides the properties such as adhesion and mechanical strength. The metallic particles are in contact with each other and serving as the electrical current pathways.

The metallic particles can be silver, copper, gold, palladium, graphite, carbon fiber, nickel, etc. The typical forms of particles are spheres, plates, rod, and flakes. Among the various conductive metal particles, silver is most commonly used thanks to its moderate cost, low reactivity with oxygen, good electrical conductivity, and chemical durability. If the silver particles are directly exposed to a humid or corrosive environment, silver can be ionized and can cause silver migration, which will lead to electrical shorts in the electronics modules. However, because in ECA joints the silver is encapsulated inside the polymer, it is difficult for the corrosion to occur. Although many tests implies that silver migration was never observed [15, 16], silver migration has been reported to occur in the ECA joints by other researchers [17].

Gold, nickel, and copper are also being used as the metallic particles in ECAs. Being compared with silver, gold has advantages of better physical properties, excellent boding surface and nearly negligible oxide rate, but the high cost of material constrains its applications. Nickel is less expensive, but has lower electrical conductivity and can easy be oxidized under the humid environment. Copper, although very cheap, has rapid oxidization rate, which limits its applications [18].

Traditionally, there are two types of ECAs: isotropic conductive adhesives and anisotropic conductive adhesives [19]. Isotropic conductive adhesives, with typical 1-10 μm sized conductive fillers, conduct electricity equally to all directions. Anisotropic conductive adhesives, with 3-5 μm sized conductive fillers, conduct electricity along only one direction. Fig. 1.3 shows the schematic of isotropic and anisotropic conductive adhesives.

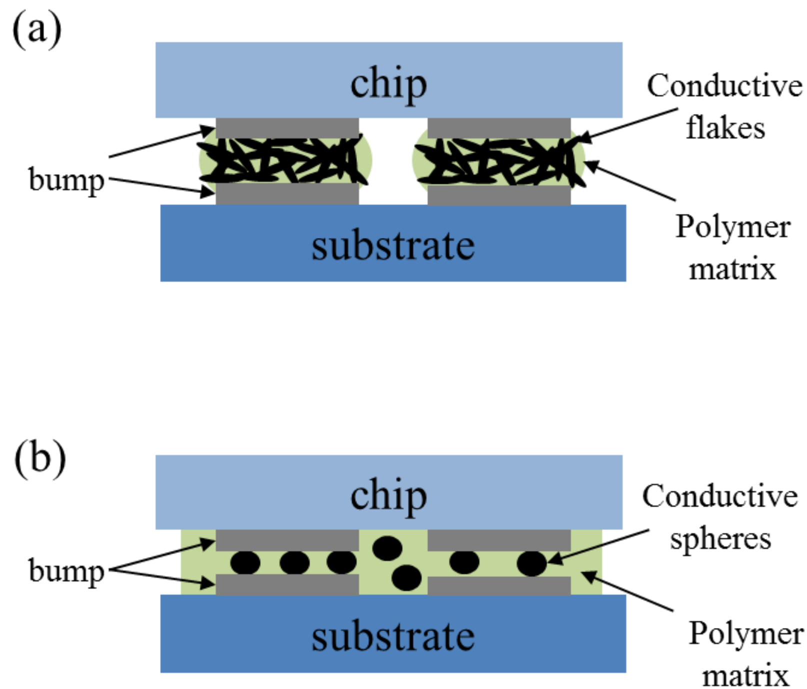

Fig. 1.3. Schematic illustration of (a) isotropic conductive adhesives and (b) anisotropic conductive adhesives.

The process of chip attachment by ECAs is relatively simple. However, being compared with solder, ECA joints have disadvantages such as lower electrical conductivity, longer curing times, lower application temperature, undetermined durability in various climatic environments, conductivity fatigue in reliability testing, limited current-carrying capability and poor impact strength. Therefore, ECAs are usually restricted to the low temperature and light duty applications.

1.1.3. Low temperature joining technique

Low temperature joining technique (LTJT) by silver sintering, has been extensively studied and used as an alternative to solder or epoxy for the fabrication of power electronic devices and modules [20-26]. This technology has been applied to a few developmental and commercial products [27, 28].

The excellent physical properties of silver, such as high melting point, high thermal and electrical conductivities, as well as its high ductility, make sintered silver a promising die-attach material. Table 1.1 compares the processing parameters and physical properties of solders, silver epoxy, and LTJT sintered silver. Because the LTJT silver bond-line is formed not by melting but by sintering, the joint layer will not melt below 961°C, which implies that the LTJT has great advantage in high temperature applications.

Table 1.1: Comparison of processing parameters and physical properties of various attachment materials.

	Processing temperature	Max. use temperature	Electrical conductivity 10^5 $(\Omega\ cm)^{-1}$	Thermal conductivity (W/K cm)	Die-shear Strength (MPa)
Lead-tin solder	217°C	< 183°C	0.69	0.51	35
Lead-free solder	260°C	< 225°C	0.75	0.70	35

Gold-tin solder	310°C	< 280°C	0.625	0.58	30 - 60
Silver epoxy	100 – 200°C	< 200°C	0.1	0.1	10 – 40
High-Pb solder	340°C	< 280°C	0.45	0.23	15
LTJT sintered silver	< 275°C	< 961°C	3.8	2.4	20 – 40

A bond formed by sintering is significantly different from that obtained by the solder reflow process. Sintering, particularly solid state sintering as in the case of silver, is a slower process and depends on temperature-activated diffusion mechanisms. As a result, the attachment process of LTJT is different from solder reflow and involves a longer timescale. Additional process parameters such as drying time, temperature, and externally applied pressure, need to be considered. Fig. 1.4 shows a schematic of heating profile of LTJT process, which consists of 2 major stages: drying stage and sintering stage. The whole heating process generally requires 30 minutes or longer.

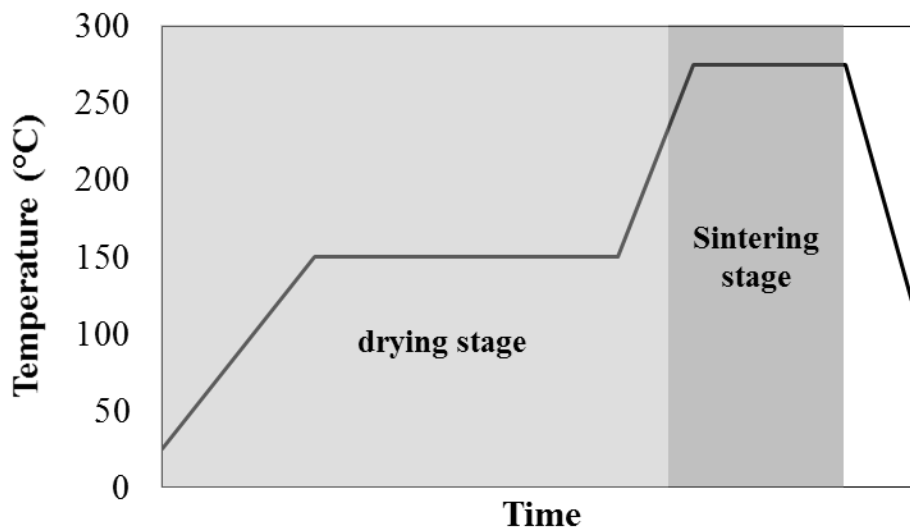

Fig. 1.4. Schematic of heating profile of LTJT process.

Some applications show that LTJT sintered silver joint layer can work in excess of 250 ℃, which is significantly higher than the working temperatures of most traditional solder-based or epoxy-based materials [29, 30]. The sintered silver joint in chip attachments has different failure mechanism from the solder joints. Because there is no intermetallic layers formed during the bonding process, no serious stress concentration occurs at the interface between bond surfaces and joint layer. During thermal cycling, the sintered silver joint can release the thermal stresses by generating vertical cracks rather than interfacial delamination [31], as shown in Fig. 1.5. Those vertical cracks have limited influence on the electrical and thermal performances, and the sintered silver joints show higher thermal reliability than traditional solders [28, 31-34].

Because of the excellent performance and much improved reliability of the LTJT sintered silver joints, the LTJT has drawn great attention from industries.

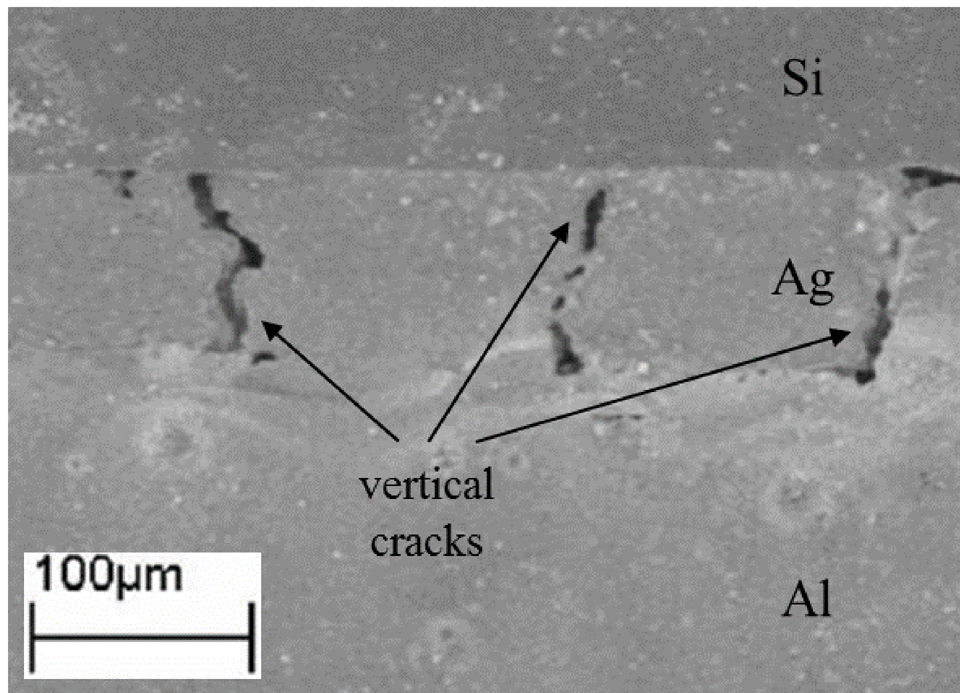

Fig. 1.5. Cross-sectional image of sintered silver bond-line after thermal cycling.

1.2. Current concerns in LTJT

1.2.1. Pressure-aided heating process of LTJT

In the conventional LTJT, the use of micron-size silver powders requires manufacturers to develop a “hot-pressing process” at over 30 MPa and 250 ℃ to form the sintered silver joints. Such level of pressure adds complexity and cost to the manufacturing process. The introduction of a nanosilver paste die-attach material [35] significantly lowers the applied pressure to achieve a bond strength comparable with that obtained in the LTJT manufacturing process. For small chips (< 10 mm^2), bonding with the nanosilver paste can be achieved with a simple heating profile with no external pressure [26, 35-38]. However, for bonding large-area chips, e.g., insulated-gate bipolar transistor (IGBT) chips larger than 100 mm^2, a uniaxial pressure of a few MPa was found to be necessary during the sintering stage of the bonding process, which is carried out at temperatures below 275 ℃ [38]. Pressing at temperatures above 200 ℃ can cause significant wear and tear on the processing equipment, particularly on the cushioning material that provides conformal contact with the die, resulting in high maintenance cost.

1.2.2. Drying process of LTJT

Moreover, the drying process of LTJT also plays a crucial role in the final sintered silver joints. Inappropriate process, especially at the drying stage before silver sintering, will increase defects (such as cracks, voids and delamination) in final sintered silver bond-line, and the defects can greatly decrease the performance and reliability of sintered joints. As shown in Fig. 1.6, once the defects (the bright part in the image) in the joint layer are formed after drying, they are hard to be removed by the following sintering process.

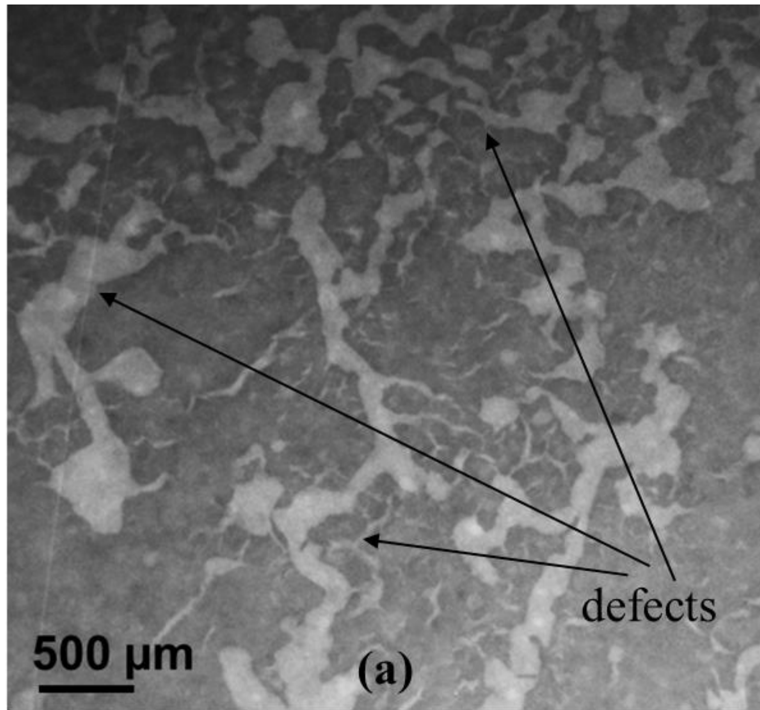

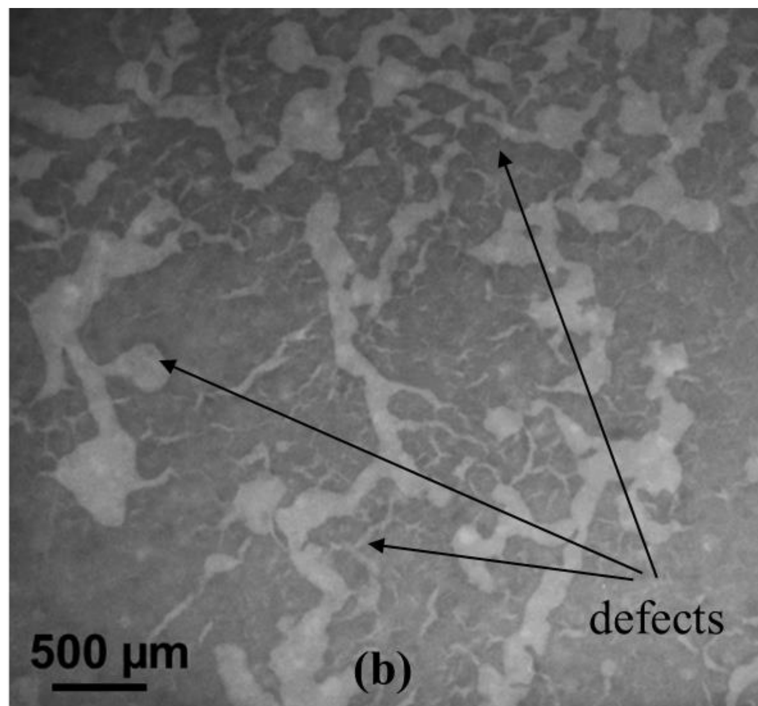

Fig. 1.6. X-ray transmission image of a chip attachment (a) after drying with an inappropriate profile (direct heated at 180°C for 30 minutes), and (b) followed by sintering at 275°C for 30 minutes with an uniaxial pressure of 3 MPa.

A reliable drying process is needed to obtain a strong, reliable, and defects-free LTJT sintered silver bond-line, and it requires the theoretical and experimental study of the drying process of LTJT.

1.3. Theories to analyze the drying behavior of LTJT

1.3.1. Liquid removal during drying

In LTJT, the drying of the paste during the bonding process plays a critical role in determining the quality of the sintered bond-line. Removal of solvent is particularly important in drying processing, as cracks and delamination may generate during this process. Therefore, liquid/moisture transport processes are significant in drying. So far there is no analytical study on the drying process of LTJT. However, the liquid/moisture transport during drying has been frequently studied in the fields of soil science, food science, wood science, and concrete science, etc. The stages of drying were thoroughly discussed [39-44]. Drying process can be divided into the constant rate period and the falling rate period. When the material is wet enough, the constant rate period occurs, at which the evaporation rate is close to that from an open dish of liquid [41]. The falling rate period occurs as the concentration of moisture falls out, and it is the major period during the whole drying process [42]. During the falling rate period, if the liquid phase is in continuous (i.e., interconnected) condition, Darcy's law can be applied [45-51], which states that the flux of liquid is proportional to the gradient in pressure in the liquid, as the capillary pressure gradient is the driving force. On the other hand, if the liquid phase is not in continuous condition (i.e., isolated in pockets), liquid evaporates and the vapor is removed out of the main body by diffusion, of which the driving force is the moisture

concentration gradient [52-55]. Diffusion equations have been widely used in the analysis of drying for porous materials such as clay, concrete, gels, and agricultural product, etc [56-59]. The linear diffusion equation, which assumes a constant diffusion coefficient, has been proved to be not good enough to fit the experimental data [60-62]. Nonlinear diffusion equation, of which assumes that the diffusivity is dependent on one or more factors such as pore humidity and temperature, can provide a better fit of the experimental data of drying [56, 57].

1.3.2. Stress induced by drying

As liquid leaving from the main body, the material shrinks. The strain and stress will generate because of the shrinkage. For the drying process of LTJT, the induced high stress is the root cause of the formation of cracks and delamination in the sintered silver bond-line. Therefore, it is crucial to find out the stress evolution during the drying process. The stress-strain relationship during the drying is being studied and several models were applied.

The model of linear elasticity can be applied in the porous elastic solid, at which liquid does not affect the stress [63, 64]. The model of viscous strain proposed the constitutive equation in the terms of strain rates, supposing the stress induces the strain rate [65, 66]. The model of linear viscoelasticity takes account of the instantaneous behavior as elasticity and time-dependent behavior as viscosity at the same time [67]. Viscoelastic analogy has been used to solve for the stress in viscoelastic materials and the solution has been used by many researchers to solve mechanical and thermal stress problems [68, 69]. From the point of mathematics, the linearly viscoelastic analysis looks correct with assumption of constant moduli. However, during the heat related processes such as

drying or sintering, the elastic modulus changes with time, temperature, and strain. Therefore, the material is no longer linearly viscoelastic during these processes, and it makes the linearly viscoelastic analogy not work effectively [65, 66]. It has been found by many researchers that the elastic strain is negligible compared to the viscous strain during densification, and the stress at the end of the elastic period is the same as that from a purely viscous analysis [70-72]. Therefore, it is reasonable to neglect the elastic response and only conduct the viscous deformation analysis for the heat related processes. Viscous analogy has been used by many researchers to explain the stress evolution of porous materials during sintering [73-79] .

1.4. Objectives and significance of the study

A major issue of LTJT is that the process which requires hot-pressing at high temperature is too complicate. To simplify the process is always in demand. Based on this reason, the objectives in this study are shown below:

(1). To better understand the behavior of nanosilver paste in a chip-attachment during drying process by developing an analytical model. The influence of process parameters (temperature, time, and external pressure) on the nanosilver paste behavior should be evaluated.

(2). To develop a simplified nanosilve-enabled LTJT process for bonding large-area chips which limits the hot-pressing at a temperature below 200 ℃.

1.5. Structure of the dissertation

Based on the objectives, this study is divided into the following chapters:

Chapter 2: Modeling of the drying behavior in nanosilver LTJT. A model based on diffusion theory and viscous mechanics was developed to describe the internal stresses and strain evolution of nanosilver paste in a chip attachment during the drying process, and an algorithm for numerical simulation of the evolution of internal stresses in nanosilver paste during drying was realized.

Chapter 3: Experiments verification of the predicted drying behavior in nanosilver LTJT. The behavior such as weight loss profile, shrinkage and defect formation of nanosilver paste in a chip attachment during drying were demonstrated by numerical simulation and compared with experiment results.

Chapter 4: Design of experiments (DOE) study on nanosilver LTJT. A fractional factorial design of experiments was used to identify the effects and interaction of various processing parameters, such as pressure, temperature, and time, on the resulting bond. Based on the results, a nanosilver enabled LTJT process for bonding large-area chips with hot-pressing below 200 ℃ was developed.

Chapter 5: Effect of external applied pressure during drying on sintered silver bond-line. The effect of drying pressure on bonding quality of the sintered silver bond-line was demonstrated by experiments and analyzed using the diffusion-viscous model by numerical simulation.

Chapter 6: Effects of temperature ramp rate and drying time on sintered silver bond-line. The effects of different room temperature pre-drying time and different temperature ramp rates on the bonding quality of the sintered nanosilver chip attachment were demonstrated by experiments and analyzed using the diffusion-viscous model by numerical simulation.

1.6. Publications

- Kewei Xiao, Khai D.T. Ngo, and Guo-Quan Lu, "A diffusion-viscous analysis and experimental verification of defect formation in sintered silver bond-line". Submitted to *Journal of Materials Research*
- Kewei Xiao, Jesus N. Calata, Hanguang Zheng, Khai D.T. Ngo, and Guo-Quan Lu, "Simplification of the nanosilver sintering process for large-area semiconductor chip bonding: reduction of hot-pressing temperature below 200°C". *IEEE transactions on Components, Packaging and Manufacturing Technology*, 2013. 3(8): p. 1271-1278
- Kewei Xiao, Susan Luo, Khai D.T. Ngo, and Guo-Quan Lu, "Low-temperature sintering of a nanosilver paste for attaching large-area power chips". *15th IEEE International Symposium on Advanced Packaging Materials (APM)*, 2013: p. 192-202
- Kewei Xiao, Jesus N. Calata, Hanguang Zheng, Khai D.T. Ngo, and Guo-Quan Lu, "Improved process for high temperature large-area sintered nanosilver device attachment", Presented at *International Conference and Exhibition on High Temperature Electronics (HiTEC) 2012*, Albuquerque, New Mexico, USA, (May 8-10, 2012)
- Kewei Xiao, Jesus Calata, Khai Ngo, Dimeji Ibitayo, and G-Q. Lu, "Large-area chip attachment by sintering nanosilver paste: process improvement by nondestructive characterization". *Transactions of The Japan Institute of Electronics Packaging*, 2011. 4(1): p. 101-109

- Kewei Xiao, Jesus Calata, and G-Q Lu, "Low-temperature sintering of nanosilver paste for attaching large-area silicon devices". Presented at *The International Conference on Electronics Packaging (ICEP) 2011*, Nara, Japan, (April 13-15, 2011)

Chapter 2. Modeling of the drying behavior in nanosilver LTJT

2.1. Introduction

In order to improve the drying process of nanosilver paste in chip attachment, the drying behavior combined with the internal stresses evolution of the nanosilver paste was analyzed in this chapter. A diffusion-viscous model was developed to show the internal stresses in the nanosilver paste in chip attachment during drying process. Based on the model, an algorithm was developed to simulate the drying behavior such as weight loss, shrinkage, and the stress evolution of the nanosilver paste in LTJT.

2.2. Model of nanosilver paste drying

2.2.1. Composition of nanosilver paste

Nanosilver paste is a lead-free material consisting of silver nanoparticles mixed with organic binders and solvents. The model of the paste consists of two parts: the solid part (silver particles, organic binders) and the liquid part (solvents). During the drying, the liquid part decreases and the solid part remains constant. The total volume of the paste shrinkages. Because the solid silver particles cannot be 100% dense, and, in fact, pores are generated during drying. Fig. 2.1 shows a schematic of the evolution of paste composition during drying.

At the initial stage, the total volume, total mass, and density of a unit cell of the paste are V^0, m^o, and ρ^o, respectively. The solid part has a volume of V_S^0 and mass of m_S^0, and the solvent has a volume of V_L^0, mass of m_L^0, and density of ρ_L. Thus,

$$V^0 = V_S^0 + V_L^0 \quad \text{(Eq. 2.1)}$$

$$m^0 = m_S^0 + m_L^0 \qquad \text{(Eq. 2.2)}$$

$$\rho^0 = m^0 / V^0 \qquad \text{(Eq. 2.3)}$$

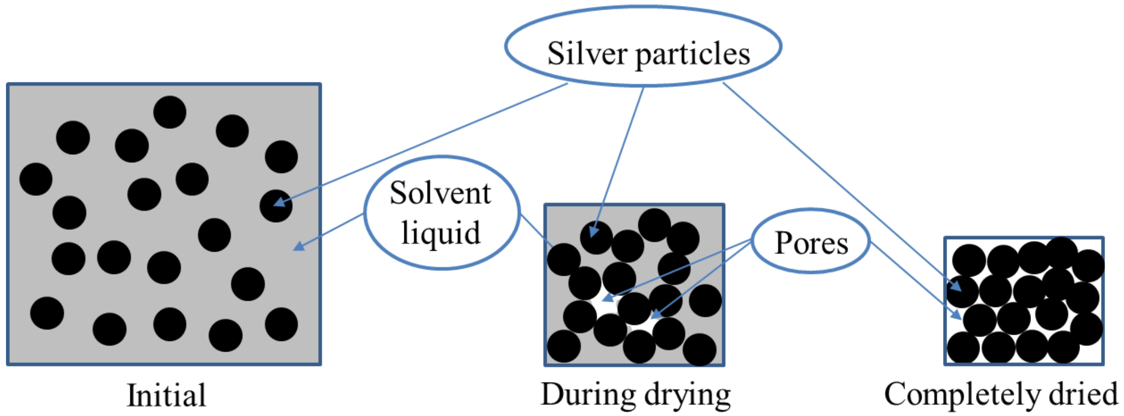

Fig. 2.1. Schematic of composition evolution of nanosilver paste during drying process.

At a given stage of drying, the solvent is partially evaporated and some pores are generated. The total volume and total mass of the unit cell are V and m, respectively. The volume V_S^0 and mass m_S^0 of the solid part remain the same. The solvent now has a volume of V_L and mass of m_L, and the pores have a total volume of V_P and mass of 0 (the pores are considered as vacuum). Thus,

$$V = V_S^0 + V_L + V_P \qquad \text{(Eq. 2.4)}$$

$$m = m_S^0 + m_L \qquad \text{(Eq. 2.5)}$$

$$\rho_L = m_L^0 / V_L^0 = m_L / V_L \qquad \text{(Eq. 2.6)}$$

$$\frac{V}{V^0} = \frac{V_S^0 + V_L + V_P}{V^0} = \frac{V^0 - V_L^0}{V^0} + \frac{V_L}{V^0} + \frac{V_P}{V^0} \qquad \text{(Eq. 2.7)}$$

The concentration of the solvent in a unit cell is $c = \frac{m_L}{V^0} = \frac{m_L \cdot \rho^0}{m^0}$ (with the unit of kg/m^3), and the normalized concentration of the solvent can be defined as a ratio of two masses, instantaneous solvent mass in a unit cell over the original total mass of the unit cell: $C_S = \frac{c}{\rho^0} = \frac{m_L}{m^0}$ (dimensionless). From here on, all concentrations are normalized concentrations (mass fraction).

The terms of Eq. 2.7 can be expressed as a function of the concentration of the solvent:

$$\frac{V^0 - V_L^0}{V^0} = 1 - \frac{m_L^0}{\rho_L} \cdot \frac{\rho^0}{m^0} = 1 - \frac{\rho^0}{\rho_L} \cdot C_S^0 \quad \text{(Eq. 2.8)}$$

$$\frac{V_L}{V^0} = \frac{m_L}{\rho_L} \cdot \frac{\rho^0}{m^0} = \frac{\rho^0}{\rho_L} \cdot C_S \quad \text{(Eq. 2.9)}$$

where $C_S^0 = \frac{m_L^0}{m^0}$ is the initial concentration of the solvent.

An empirical formula for $\frac{V_P}{V_0}$ is applied [80-82]:

$$\frac{V_P}{V_0} = a_1 (C_S^0 - C_S)^{a_2} \quad \text{(Eq. 2.10)}$$

where a_1 and a_2 are model parameters.

Substituting Eq. 2.8 to Eq. 2.10 into Eq. 2.7, we have:

$$\frac{V}{V^0} = 1 + \frac{\rho^0}{\rho_L} \cdot (C_S - C_S^0) + a_1 \cdot (C_S^0 - C_S)^{a_2} \quad \text{(Eq. 2.11)}$$

The nanosilver paste (nanoTach®, type K) used in this study was provided by NBE technologies, LLC. For the fresh paste, the initial density ρ^0 is 4.0 g/cm^3, and the

density of the solvent ρ_L is 1.0 g/cm^3. C_S^0 is calculated to be 17%. Based on experience, the parameters a_1 and a_2 are set to 35 and 3, respectively.

Fig. 2.2 shows the variation of volume (with or without pores) with solvent concentration. When the concentration of solvent is high, few pores are generated in the volume and the volume change is almost proportional to the solvent loss. When the concentration of solvent is low, pores become significant in the volume.

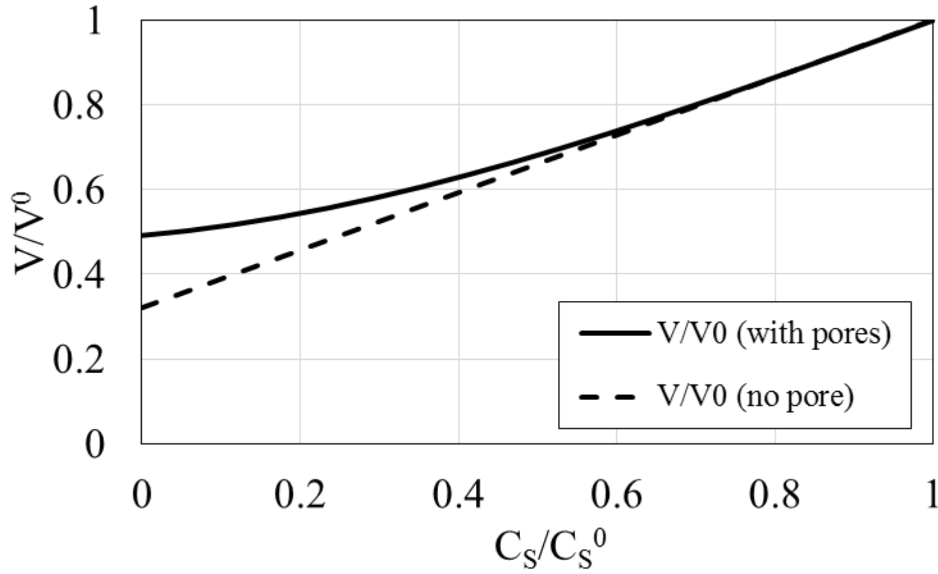

Fig. 2.2. Relationship between volume ratio (V/V^0) and solvent concentration (C_S/C_S^0).

The free strain is defined as follows:

$$\varepsilon_f = \frac{1}{3}\cdot\frac{\Delta V}{V^0} = \frac{1}{3}\cdot\frac{(V - V^0)}{V^0} = \frac{1}{3}\left[\frac{\rho^0}{\rho_L}\cdot(C_S - C_S^0) + a_1\cdot(C_S^0 - C_S)^{a_2}\right] \qquad \text{(Eq. 2.12)}$$

So far, the volume change ($\frac{V}{V^0}$), porosity change ($\frac{V_P}{V^0}$), and free strain ε_f of the paste in a unit cell during drying can be expressed as a function of concentration of solvent (C_S).

2.2.2. Viscous model for stress analysis

Nanosilver paste is soft and is in a viscous form before it sinters to metallic silver. Therefore, elastic or elastoplastic models are not suitable in the case of nanosilver paste drying. A model with the consideration of viscosity should be more appropriate. Here, a viscous model for stress analysis is applied.

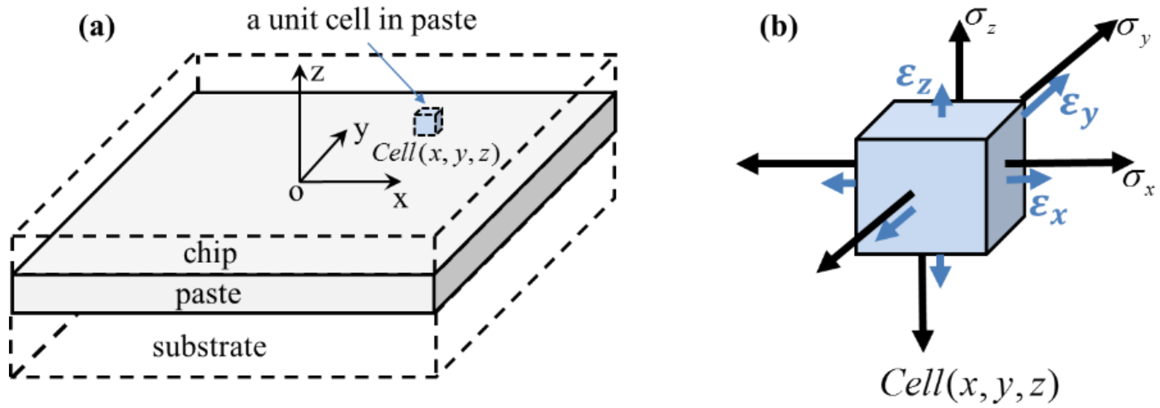

Fig. 2.3. Schematic of (a) a unit cell in at position (x, y, z) in paste, and (b) the principle stresses and principle strains generated in the unit cell.

As shown in Fig. 2.3, the principal stresses and principal strains generated in a unit cell $Cell(x,y,z)$ of the paste are $(\sigma_x,\sigma_y,\sigma_z)$ and $(\varepsilon_x,\varepsilon_y,\varepsilon_z)$, respectively. Assuming that the paste material is isotropic, we can express the constitutive stress-strain relationship as follows [65, 66]:

$$\begin{cases} \dot{\varepsilon}_x = \dot{\varepsilon}_f + \frac{1}{E}\left[\sigma_x - \upsilon\left(\sigma_y + \sigma_z\right)\right] \\ \dot{\varepsilon}_y = \dot{\varepsilon}_f + \frac{1}{E}\left[\sigma_y - \upsilon\left(\sigma_z + \sigma_x\right)\right] \\ \dot{\varepsilon}_z = \dot{\varepsilon}_f + \frac{1}{E}\left[\sigma_z - \upsilon\left(\sigma_x + \sigma_y\right)\right] \end{cases} \quad \text{(Eq. 2.13)}$$

where $\dot{\varepsilon}_i = \frac{\partial \varepsilon_i}{\partial t}, (i = x, y, z)$ is the rate of principle strain; and $\dot{\varepsilon}_f$ is the rate of free linear strain of unconstrained paste. E and υ are uniaxial viscosity and viscous Poisson's ratio of paste, respectively.

During the drying process, the paste is constrained on the x-y plane by the chip and substrate. The chip and substrate are both assumed to be rigid bodies undergoing no deformation. Therefore, for the paste, the rate of strain on the x-y plane is always zero; furthermore, the rate of strain in the z-direction is independent of locations on the x-y plane at any given time. These can be expressed as Eq. 2.14:

$$\begin{cases} \dot{\varepsilon}_x = \dot{\varepsilon}_y \equiv 0 \\ \frac{\partial \dot{\varepsilon}_z}{\partial x} = \frac{\partial \dot{\varepsilon}_z}{\partial y} \equiv 0 \end{cases} \quad \text{(Eq. 2.14)}$$

By solving Eq. 2.13 and Eq. 2.14, the principal stresses $(\sigma_x, \sigma_y, \sigma_z)$ can be expressed as functions of $\dot{\varepsilon}_f$ and $\dot{\varepsilon}_z$:

$$\sigma_x = \sigma_y = \frac{E}{(1-2\upsilon)(1+\upsilon)}[\upsilon\dot{\varepsilon}_z - (1+\upsilon)\dot{\varepsilon}_f] \quad \text{(Eq. 2.15)}$$

$$\sigma_z = \frac{E}{(1-2\upsilon)(1+\upsilon)}[(1-\upsilon)\dot{\varepsilon}_z - (1+\upsilon)\dot{\varepsilon}_f] \quad \text{(Eq. 2.16)}$$

From here on, we express σ_x (or σ_y) as x-y in-plane internal stress, and σ_z as vertical internal stress.

Fig. 2.4 shows the load condition of the chip. P_{apply} represents the external applied pressure on chip, and σ_z is the reaction stress of paste along Z direction.

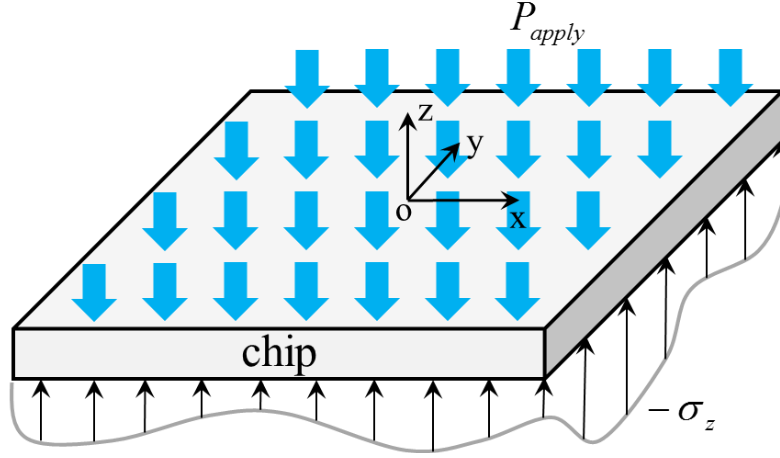

Fig. 2.4. Load condition of chip, showing external applied pressure P_{apply} and reaction stress of paste σ_z.

To analysis the chip, because of the force equilibrium along Z direction:

$$\sum F_z = -\iint_A \sigma_z dA - P_{apply} A = 0 \qquad \text{(Eq. 2.17)}$$

where A is the area of paste covered by chip and substrate.

By substituting Eq. 2.16 into Eq. 2.17, we can derive:

$$\dot{\varepsilon}_z = [\iint_A \frac{E}{(1-2\upsilon)} \dot{\varepsilon}_f dA - P_{apply} A] / \iint_A \frac{E(1-\upsilon)}{(1-\upsilon-2\upsilon^2)} dA \qquad \text{(Eq. 2.18)}$$

Substituting Eq. 2.18 into Eq. 2.15 and Eq. 2.16, we can express the principal stresses σ_x, σ_y, and σ_z as functions of the uniaxial viscosity (E), Poisson's ratio (υ), the free strain rate ($\dot{\varepsilon}_f$), and the external applied pressure (P_{apply}).

In principle, at any given time, if the values of E, υ, $\dot{\varepsilon}_f$ and P_{apply} are known, the x-y in-plane internal stress (σ_x or σ_y) and vertical internal stress (σ_z) of the paste can be calculated.

Uniaxial viscosity (E): Viscosity is a material property of the paste. Practically, it is related to the solvent concentration. The higher the concentration, the lower the viscosity. The viscosity of the undried paste is 700,000 cP, and it increases to as high as 10^{15} cP for a completely dried (but not sintered) paste. It is reasonable to assume that viscosity is a monotonically decreasing function of solvent concentration. The relationship between the viscosity and concentration of the solvent of the paste is shown in Table 2.1.

Table 2.1: Relationship between viscosity E and concentration of solvent of paste C_S

C_S (%)	E (cP)	E (Pa s)
0	1×10^{15}	1×10^{12}
17	7×10^{5}	7×10^{2}
100 (pure solvent)	1	1×10^{-3}

It is assumed there is a reciprocal relationship between viscosity and concentration of solvent. The equation format is set as Eq. 2.19:

$$\ln(E) = \frac{1}{A\cdot C_S + B} + C \qquad \text{(Eq. 2.19)}$$

The curve fitting for viscosity-concentration relationship is shown in Fig. 2.5, and the parameters are determined to be: A=0.1673, B=0.02517, and C=-12.10.

Therefore, the viscosity can be described as a function of concentration of solvent:

$$E = \exp\left(\frac{1}{0.1673\cdot C_S + 0.02517} - 12.10\right) \qquad \text{(Eq. 2.20)}$$

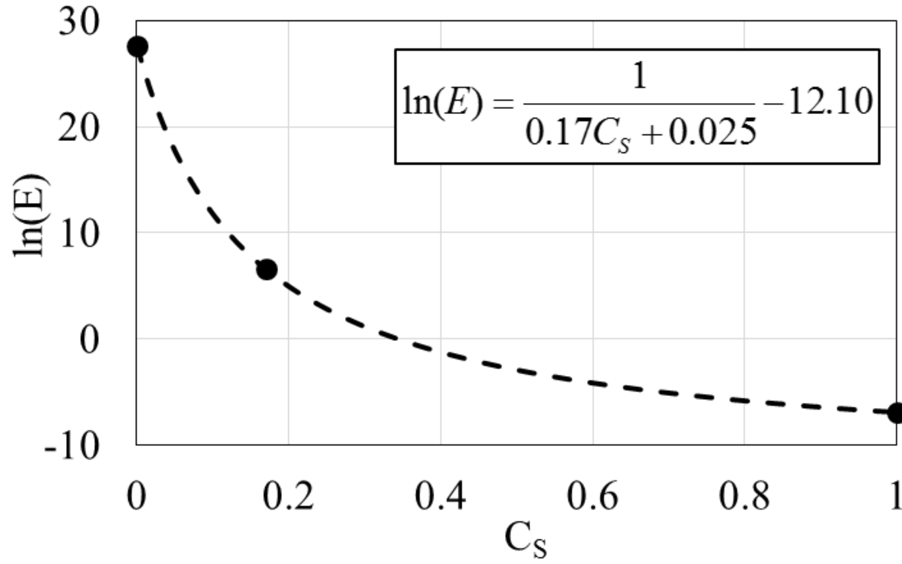

Fig. 2.5. Curve fitting of viscosity-concentration data.

Poisson's ratio (υ): The viscous Poisson's ratio is related to volume fraction of liquid and porosity. Unfortunately, at the moment we do not have a functional form of the relationship for the paste material. Since the Poisson's ratio of silver is 0.37, and for most engineering materials, Poisson's ratio varies from 0.3-0.4. In this model, a constant value of Poisson's ratio of 0.37 is used to simplify the analysis.

Free strain rate ($\dot{\varepsilon}_f$): As shown in Eq. 2.12, the free strain is a function of concentration of solvent. Taking the derivative of the free strain with respect to time, we obtain:

$$\dot{\varepsilon}_f = \frac{\partial \varepsilon_f}{\partial t} = \frac{1}{3}\left[\frac{\rho^0}{\rho_L} - a_1 \cdot a_2 (C_S^0 - C_S)^{a_2 - 1}\right]\frac{\partial C_S}{\partial t} \qquad \text{(Eq. 2.21)}$$

Therefore, the free strain rate is a function of the concentration (C_S) and the rate of change of concentration ($\frac{\partial C_S}{\partial t}$) of the solvent.

External applied pressure (P_{apply}): The external applied pressure is controlled manually in the drying process.

Since the internal stresses of the paste is related to the concentration and rate of change of concentration of the solvent, the internal stresses at a given location of the paste can be calculated if the concentration and rate of change of concentration of the solvent at that location are determined during the paste drying process.

The x-y in-plane internal stress is the reason for paste cracking, and the vertical internal stress is the reason for chip-paste debonding. The analysis of evolution of internal stresses during the paste drying process can provide a guideline to optimize the drying process by changing the drying process parameters.

2.2.3. Kinetics of solvent movement in paste

Fig. 2.6 shows the "sandwich" structure of the paste between the chip and the substrate. Because the top surface and bottom surface of the paste are covered by the chip and substrate, respectively, the solvent can escape only from the edges. Since no solvent can escape along the z-direction and the thickness of the paste is much smaller than the length or width, the movement of solvent along the z-direction can be ignored. Therefore, the solvent movement in the paste can be simplified to a 2D problem.

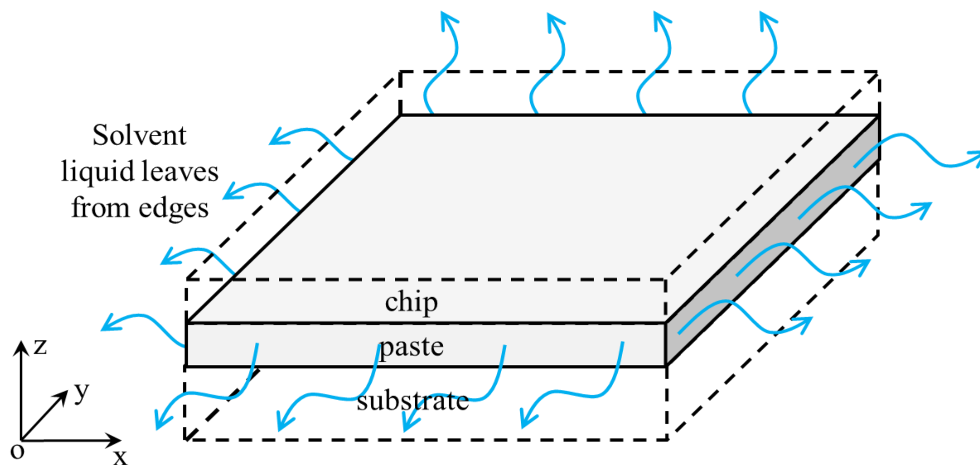

Fig. 2.6. Paste deposits between the chip and the substrate, which causes solvent only leaving from the edges.

There are two possible transport mechanisms for solvent to move inside a drying paste: fluid flow and diffusion. Fluid flow obeys Darcy's law, which requires the liquid phase to be interconnected and is driven by capillary pressure; diffusion follows Fick's law, and the driving force is the concentration gradient. During the drying of the nanosilver paste bond-line, the capillary pressure gradient developed along the bond-line edges, as the driving force for fluid flow, is negated by the resistance of a large area of the viscous paste trapped between the two plates. Effectively, this makes the silver paste bond-line behaves like a thick body that according to Scherer [39], the capillary pressure gradient should be negligible, thus preventing liquid flow by Darcy's law. Thus, the constrained-film configuration of the silver paste makes solvent diffusion as the predominant transport mechanism for the drying process. For diffusional solvent movement [55-58], we have:

$$\frac{\partial C_S(x,y;t)}{\partial t} = D(T)\left(\frac{\partial^2 C_S(x,y;t)}{\partial x^2} + \frac{\partial^2 C_S(x,y;t)}{\partial y^2}\right), \ -\frac{a}{2} < x, y < \frac{a}{2} \qquad \text{(Eq. 2.22)}$$

where $C_S(x,y;t)$ is the concentration of solvent, and $D(T)$ is the diffusivity of solvent in the paste. $C_S(x,y;t)$ is a function of position coordinates (x, y) and time (t). $D(T)$ is a function of temperature (T).

In the vicinity of room temperature, $D(T)$ was estimated by the following expression based on the experimental data of ethanol [83]:

$$D(T) = 3.80\times10^{-11}T - 1.02\times10^{-8} \qquad \text{(Eq. 2.23)}$$

In Eq. 2.23, T is in the unit K, and D is in the unit m^2/s.

The initial and boundary conditions of solvent movement can be described below:

$$\text{At } t=0,\ -\frac{a}{2}\le x, y\le\frac{a}{2}:\ C_S=C_S^0 \qquad \text{(Eq. 2.24)}$$

$$\text{At } t>0:\ D(T)\frac{\partial C_S}{\partial x}\bigg|_{x=\pm\frac{a}{2}}=-J/\rho^0,\ D(T)\frac{\partial C_S}{\partial y}\bigg|_{y=\pm\frac{a}{2}}=-J/\rho^0 \qquad \text{(Eq. 2.25)}$$

where J is the mass flux of solvent at the edges of the paste, and ρ^o is the initial density of the paste, as mentioned before. J is a function of temperature (T) and solvent concentration (C_S).An empirical equation for J can be used:

$$J=a_3\cdot\exp(-\frac{a_4}{T})\cdot C_L \qquad \text{(Eq. 2.26)}$$

where a_3 and a_4 are fitting parameters.

The rate of weight loss β of the solvent in the paste can be described by

$$\beta=\iint_{A_e} J\cdot dA_e \qquad \text{(Eq. 2.27)}$$

where A_e is the surface area of the paste through which the solvent can escape.

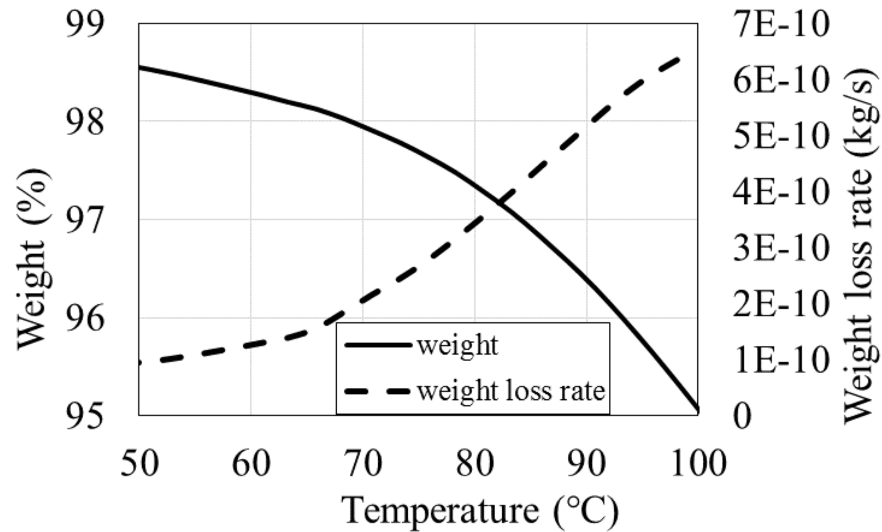

Fig. 2.7. TGA plot of nanosilver paste under early drying condition at heating rate of 5 ℃/min.

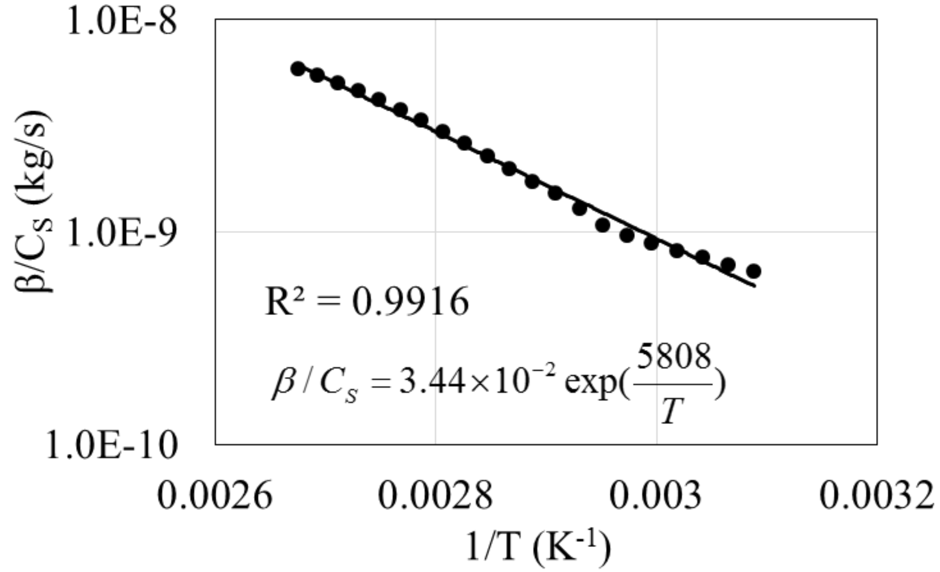

Fig. 2.8. Curve fitting for the rate of weight loss of solvent in the paste.

β can be obtained from thermogravimetric analysis (TGA). A nanosilver paste sample (5 mg) was heated in air from 50 ℃ to 100 ℃ at a rate of 5 ℃/min. Fig. 2.7 shows the TGA results, and Fig. 2.8 shows the fitting curve to determine the fitting parameters in Eq. 2.26.

The surface area through which the solvent can escape is approximately 5 mm^2, and the mass flux can be determined as

$$J = 6880 \times \exp(-\frac{5808}{T}) \times C_S \text{ [unit: kg/(s m}^2\text{)]} \qquad \text{(Eq. 2.28)}$$

From Eq. 2.22 to Eq. 2.25, the concentration (C_S) and the change rate of concentration ($\frac{\partial C_S}{\partial t}$) of the solvent at any location in the paste can be calculated at any given time. Therefore, the evolution of the internal stresses in the paste can be determined.

2.2.4. Internal stresses evolution of nanosilver paste during drying

Fig. 2.9 shows the schematic of internal stresses evolution and defect formation caused by the drying of nanosilver paste in the chip attachment. Because the solvent leaves from

the paste, the paste intends to shrink. However, the paste is constrained between the substrate and the chip plates, thus it cannot freely shrink. The internal stresses are generated by the constriction. Furthermore, the drying process can affect the tendency of paste shrinkage, which can also affect the stress distribution and stress evolution. If the internal stresses are too high, the unit cell will rupture, and it will cause the defect formation in the joint layer of nanosilver paste.

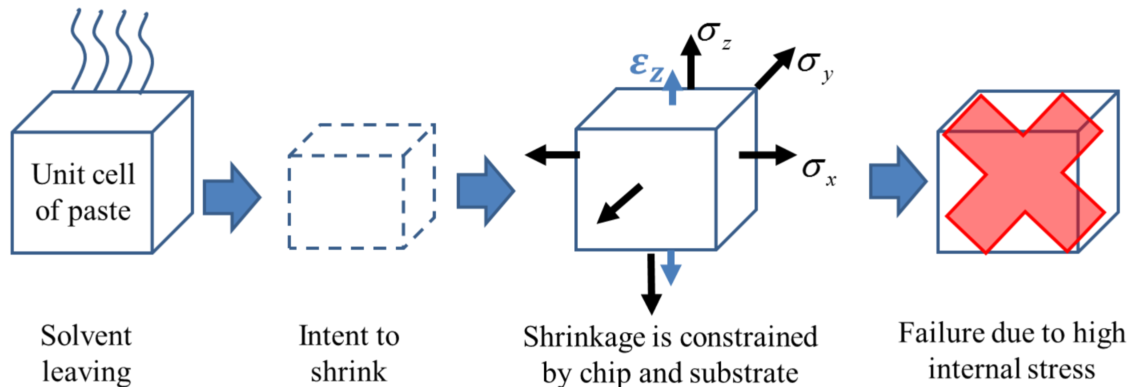

Fig. 2.9. Schematic of stress evolution and defect formation caused by the drying of nanosilver paste in constrained chip attachment.

Because the failure criterion of the paste is related to the concentration of the solvent and is hard to be accurately determined, the model does not consider paste failure during the drying process. The parameters used in the calculations are obtained from the literatures or empirical curve fitting as approximation. However, the trend of the internal stress evolution can provide a guidance for failure analysis of the paste in the chip attachment.

2.3. Algorithm and flow chat for stress evolution

Eq. 2.22 to Eq. 2.25 need to be solved to obtain the concentration of solvent. Analytical solutions for these equations are difficult to obtain, especially when the temperature changes with time, affecting the change of diffusivity and mass flux rate of the solvent.

Therefore, numerical simulation is a practical approach to solve Eq. 2.22 to 2.25 for the evolution of the solvent concentration. Furthermore, the evolution of internal stresses in the paste during the entire drying process can be simulated by solving Eq. 2.15 and Eq. 2.16.

In numerical simulation, the structure of the paste is divided into small grids. As shown in Fig. 2.10, a paste layer with the length of a is divided into small grids with the length dimensions of dx and dy. If the sizes of the grids are small enough, the material properties (E, C_S) and mechanical behaviors ($\sigma, \dot{\varepsilon}$) can be considered uniform within each grid. The location of each grid can be expressed as $Cell(i, j)$. Similarly, a period of time can be divided into many small increment steps dt, so that the properties and behaviors of the paste do not change within each step.

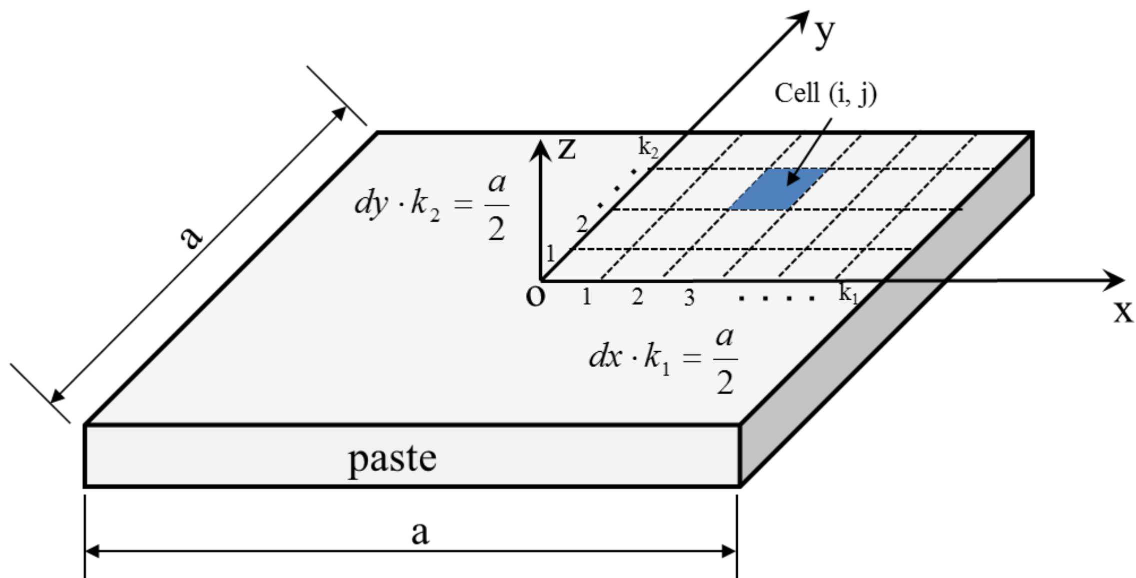

Fig. 2.10. Meshing of paste structure for numerical simulation.

All differential equations are rewritten in finite difference format. For example,

$$\begin{cases} \dfrac{\partial C_L(x,y;t)}{\partial t} = \dfrac{C_L(i,j;t+dt) - C_L(i,j;t)}{dt} \\ \dfrac{\partial C_L(x,y;t)}{\partial x} = \dfrac{C_L(i+1,j;t) - C_L(i,j;t)}{dx} \\ \dfrac{\partial C_L(x,y;t)}{\partial y} = \dfrac{C_L(i,j+1;t) - C_L(i,j;t)}{dy} \end{cases} \qquad \text{(Eq. 2.29)}$$

Since the calculation of internal stresses and strain of nanosilver paste in the chip attachment is based on the solvent movement, the accuracy of the numerical solution of solvent movement is crucial. In order to ensure the stability and accuracy of the explicit numerical solution for diffusional solvent movement simulation, a criterion between the time increment step (dt), the size of meshing grids (dx, dy), and the diffusivity ($D(T)$) is required to obey [84, 85]:

$$dt < \frac{\min(dx^2, dy^2)}{2 \cdot D(T)} \qquad \text{(Eq. 2.30)}$$

The details of the paste profiles, such as solvent distribution and internal stress distribution, increase with decreasing the grid dimensions. However, as shown in Eq. 2.30, time increment step decreases with decreasing the grid dimensions. It implies that the smaller of the grid size, the more computing loops are required to ensure the stability of numerical solution, which requires larger space storage and longer computing time. Since the typical sizes of the chip attachments vary from 1×1 mm^2 to 15×15 mm^2, the grid dimensions are typically set as 0.1×0.1 mm^2, which are good enough to show the details of stress and concentration distributions of nanosilver paste in a chip attachment without redundant long time computing.

The flow chart of internal stress outputs with different drying profile inputs is shown in Fig. 2.11, consisting of the following steps: (1) input the physical parameters of the paste

and the drying profile into the program; (2) mesh the paste structure into small grids according to the input parameters, and determine the time increment step; (3) set initial time point to start the simulation; (4) at a given time, find the temperature and external pressure according to the drying profile and the corresponding physical parameters of the paste; (5) calculate the change in solvent concentration within a time increment step; (6) calculate the internal stresses at that time; (7) set new time point as time increases; and (8) go back to step (4) before time ends.

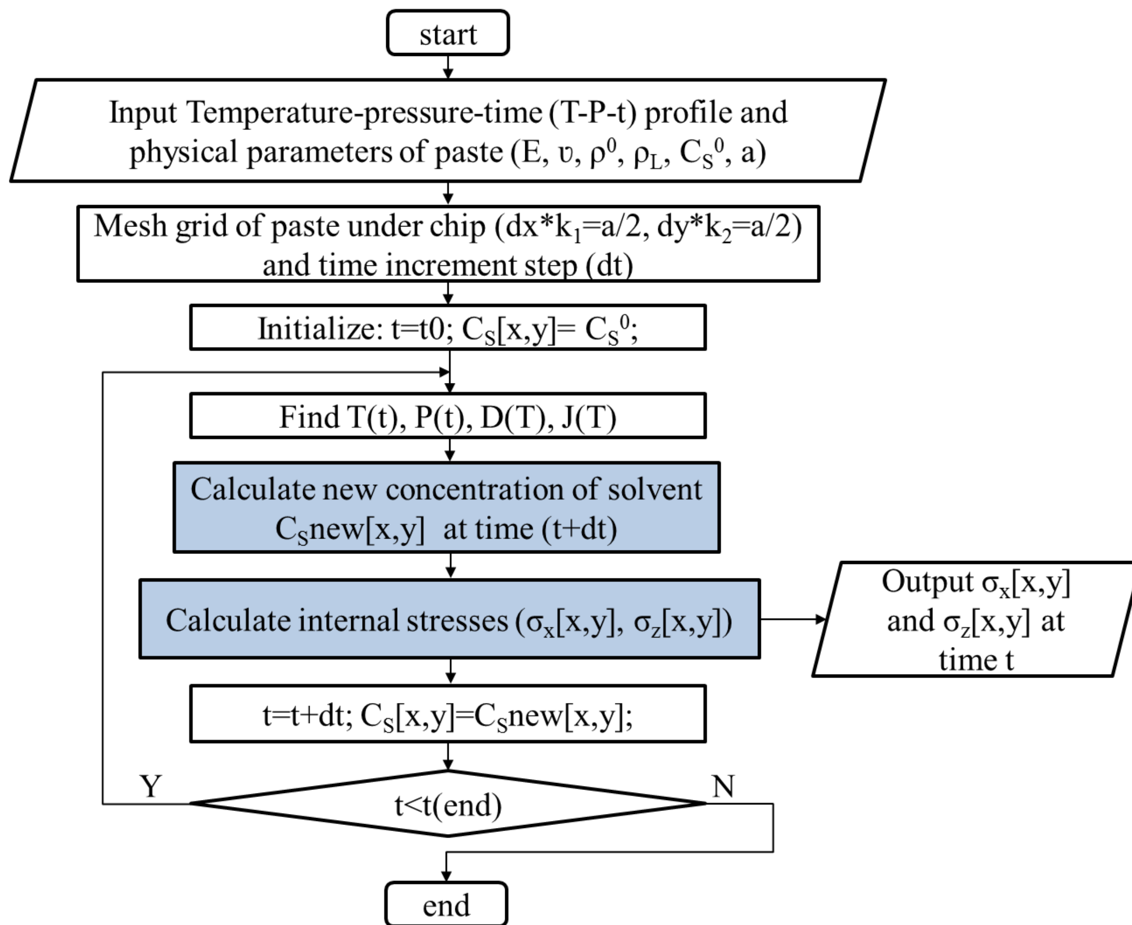

Fig. 2.11. Flow chart of the internal stress evolution outputs with different drying profile file inputs.

The algorithm of highlighted module “Calculate new concentration of solvent at time (t+dt)” is shown in Fig. 2.12. The inputs to the module are the dimensions of meshed

grids (dx, dy), number of meshed size in x and y directions (k1, k2), time increment step (dt), current solvent concentration profile ($C_S[x,y]$), current diffusivity (D(T)), current mass flux (J(T)), and the initial density of the paste (ρ^0). The new solvent concentration at the boundaries is firstly determined by the boundary conditions. Then the solvent concentration at the center part can be determined using the finite differential form of the equation of Fick's second law. The outputs are the profile of current change rate of solvent concentration, and the profile of new solvent concentration distribution.

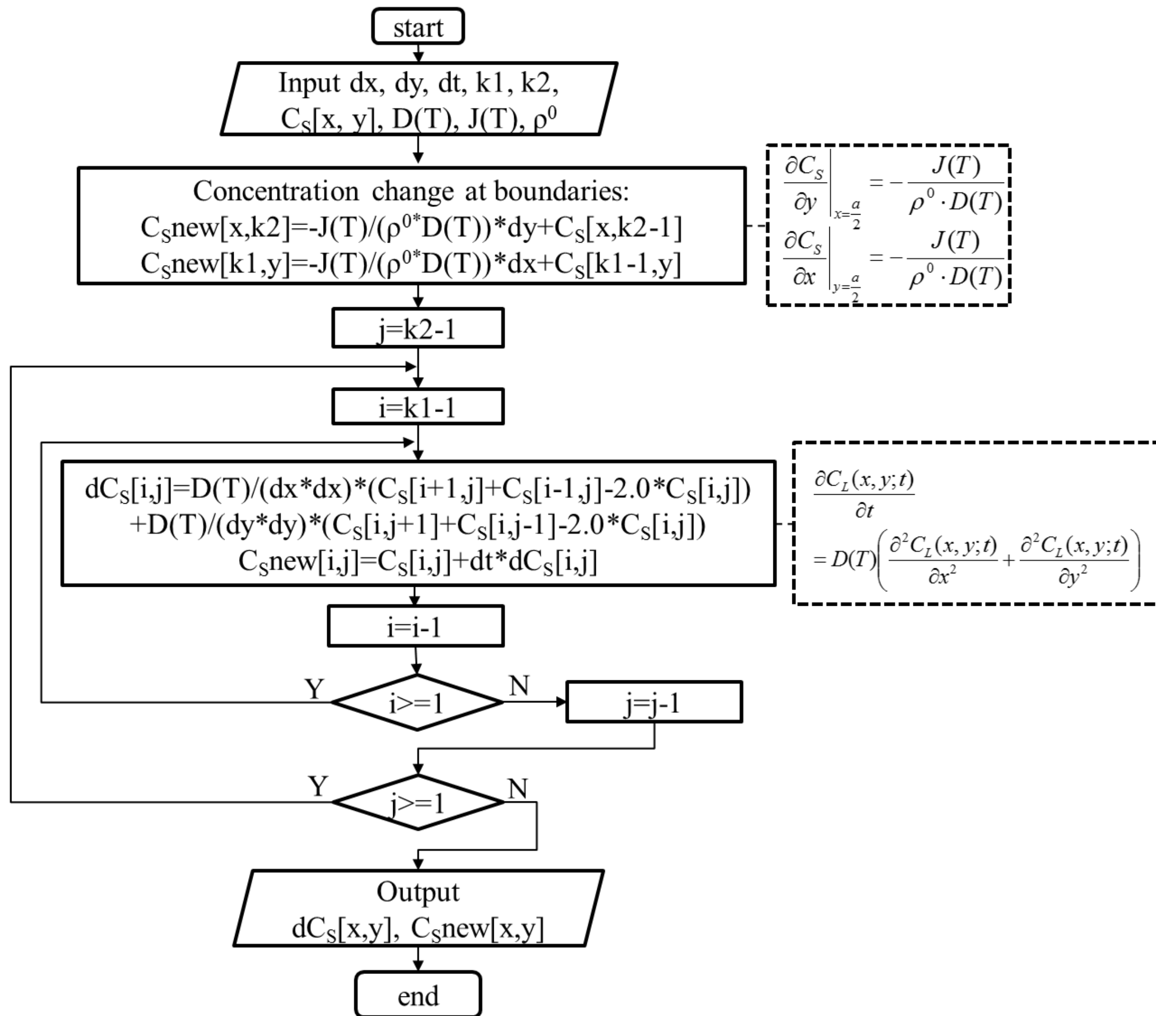

Fig. 2.12. Flow chart for new concentration of solvent calculation for a small time increment dt.

The algorithm of highlighted module “Calculate internal stresses” is shown in Fig. 2.13.

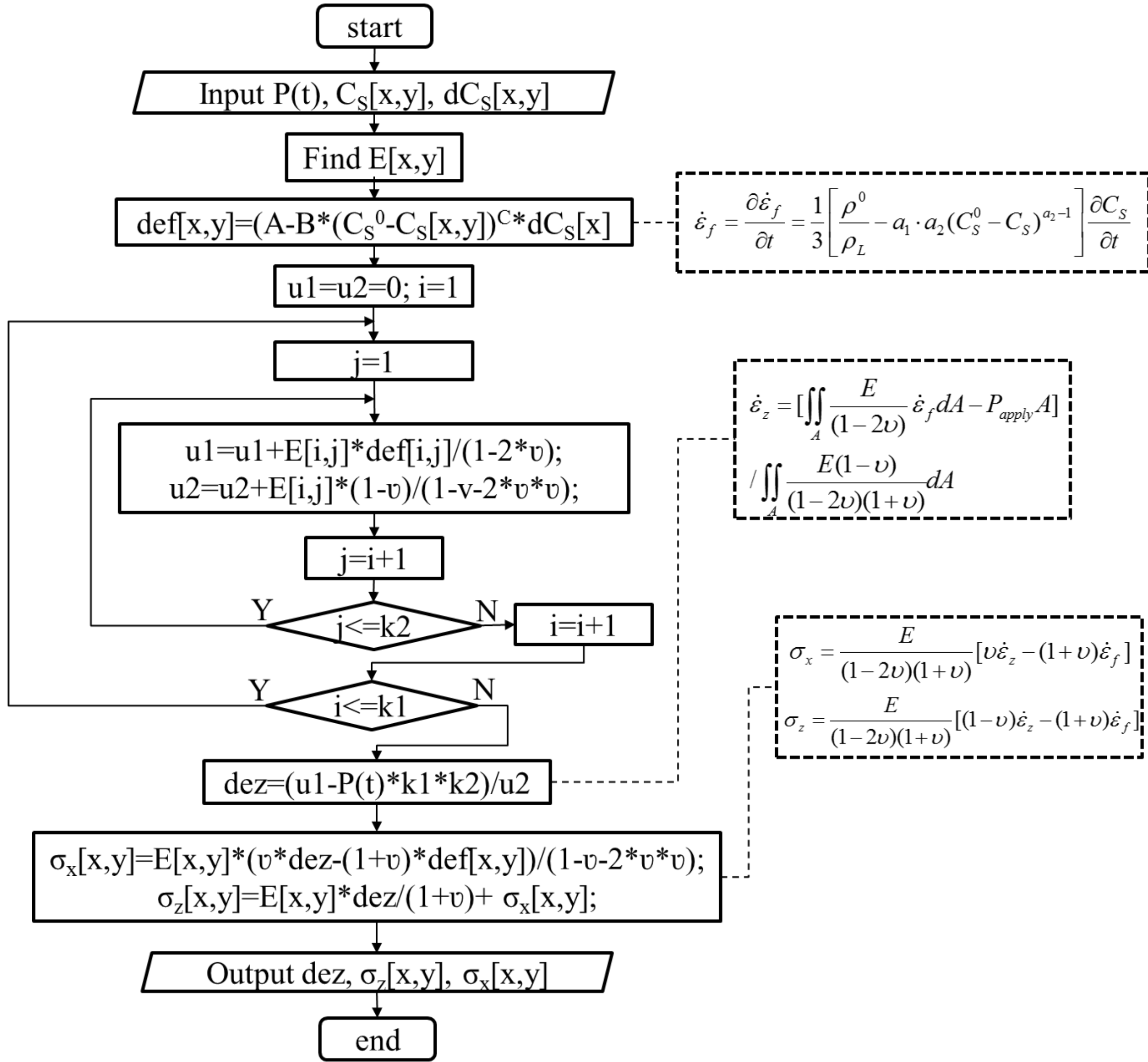

Fig. 2.13. Flow chart for internal stresses calculation at time t.

The inputs to the module are the external applied pressure (P(t)), profile of current change rate of solvent concentration ($dC_S[x,y]$), and the profile of the solvent concentration distribution ($C_S[x,y]$). First step is to determine the distributions of viscosity (E) and free strain rate (def[x,y]) at different locations of the paste in the chip attachment, and next step is to calculate the vertical strain rate (dez) of the paste according to Eq. 2.18. The final step is to calculate the distribution of x-y in-plane

internal stress and distribution of vertical internal stress via Eq. 2.15 and Eq. 2.16. The outputs are the vertical strain rate, x-y in-plane internal stress and vertical internal stress. A computational program is coded by C++ programming language to realize the algorithm. The source code and the input file format are shown in Appendix A.

2.4. Summary

In this chapter, the drying behavior combined with the internal stress evolution of the nanosilver paste was analyzed. A model that based on diffusion theory and viscous mechanics was developed to determine the stress evolution of nanosilver paste in a chip attachment during drying process. A numerical simulation algorithm of the model was developed and realized by a C++ program, which can simulate the 2D diffusion process of solvent moving with internal stress and strain evolution. With the help of program, the drying behavior of the paste, such as the evolution of solvent concentration distribution, internal stress distribution, and strain can be simulated for any drying profile with different combinations of time, temperature and external applied pressure.

Chapter 3. Experiments verification of the predicted drying behavior in nanosilver LTJT

3.1. Introduction

The internal stresses of the nanosilver paste can hardly to be directly measured. However, several methods can be used to test the model for nanosilver paste drying. Weight loss profile shows the solvent loss in the nanosilver paste, which is related to the solvent diffusion behavior in the model. Shrinkage profile shows the deformation of nanosilver paste layer, which is related to the stress-strain behavior in the model. The defect formation implies high localized internal stress, which is related to the internal stress distribution of paste in chip attachment.

3.2. Weight loss profile of nanosilver paste

The weight loss profile of nanosilver paste in a chip attachment can be simulated using the model presented above. By monitoring the concentration of solvent in the paste, the weight percentage of the paste can be calculated by Eq. 3.1:

$$W_{paste} = \frac{M_S^0 + M_L}{M_S^0 + M_L^0} = 1 - \frac{M_L^0}{M_S^0 + M_L^0} + \frac{M_L}{M_S^0 + M_L^0} = 1 - C_S^0 + \overline{C}_S \qquad \text{(Eq. 3.1)}$$

where W_{paste} is the weight percentage of the paste; $\overline{C}_S$ is the average concentration of solvent in the paste; M_S^0 and M_L^0 are the initial total masses of the solid part and liquid part of the paste, respectively; and M_L is the mass of the liquid part of the paste during drying.

In the simulation, the area of the paste between the chip and the substrate was 5 × 5 mm^2. A quarter of the structure was meshed to 625 (25 × 25) grids, and each grid had a length of 0.1 mm.

In the experiment, the weight loss of the nanosilver paste between the chip and the substrate was characterized by using a thermogravimetric analyzer (TGA, model STA 449 C Jupiter®, Netzsch-Gerätebau GmbH). Samples for TGA were prepared as follows: the nanosilver paste was applied to an alumina substrate by stencil printing. The wet print thickness was 50 μm. Then the paste layer was covered by an alumina chip. The area of the paste between alumina substrate and chip was 5 × 5 mm^2.

The samples were heated according to either a constant-rate or a ramp-soak temperature profile, as shown in Fig. 3.1. Profile 1 is a constant rate heating from 25 ℃ to 225 ℃ at the heating rate of 10 ℃/min, and profile 2 is a ramp-soak combined heating from 25 ℃ to 180 ℃, as the real drying profile in the nanosilver LTJT process.

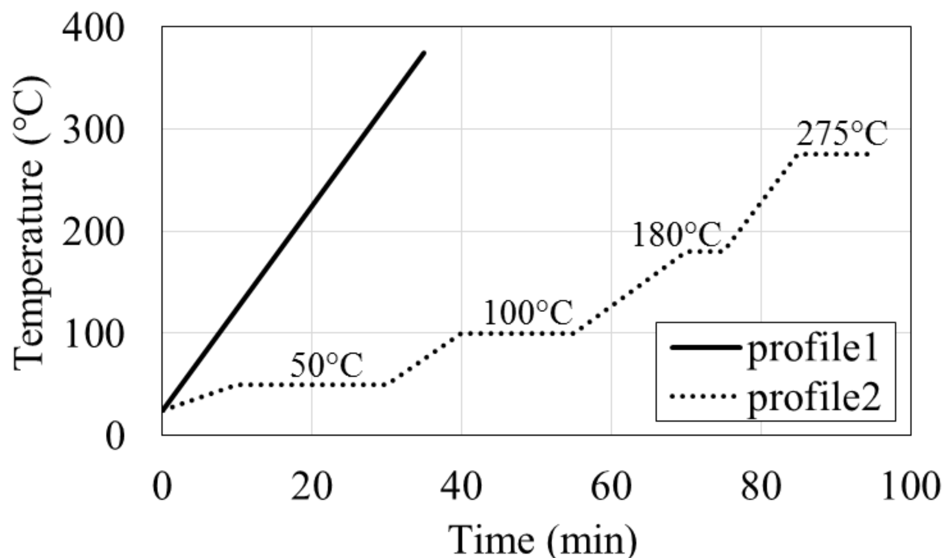

Fig. 3.1. Heating profiles for weight loss measurements. Profile 1 is constant ramp rate heating and profile 2 is ramp-soak combined heating.

Fig. 3.2 and Fig. 3.3 show the weight loss profiles of the nanosilver paste between the chip and the substrate according to constant ramp rate heating (profile 1) and ramp-soak combined heating (profile 2), respectively. In each figure, the experimental data were compared with the simulation results.

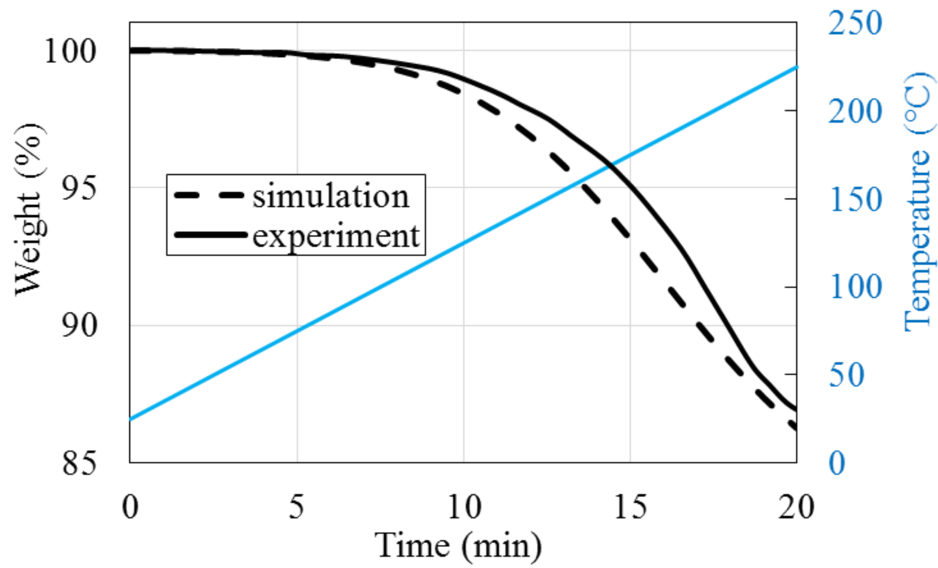

Fig. 3.2. Experimental and simulated weight loss profile for nanosilver paste in chip attachment with 5 mm chip length at heating profile 1 (constant heating rate).

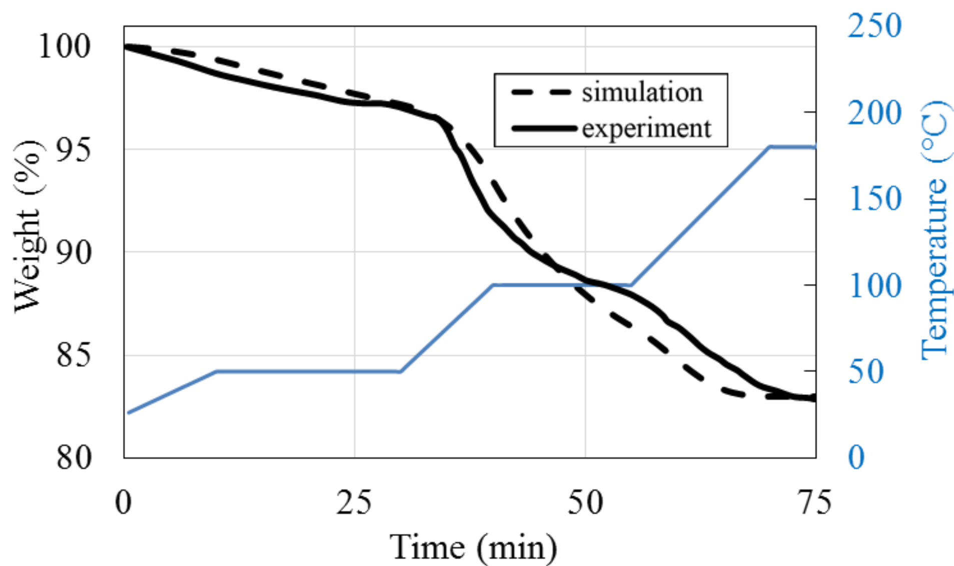

Fig. 3.3. Experimental and simulated weight loss profile for nanosilver paste in chip attachment with 5 mm chip length at heating profile 2 (ramp-soak heating).

Fig. 3.2 shows that the experimental and the simulated weight losses are small at temperatures below 100 ℃, but dramatic between 100 ℃ and 180 ℃. Fig. 3.3 shows that both the experimental and simulated weight losses are insignificant in the first 35 minutes (under 90 ℃). Both the experimental and simulated weight loss rates gradually decrease at the 100 ℃ soaking stage, but increase again as the temperature goes up. Both Fig. 12 and Fig. 13 show that the simulation results are in good agreement with the experimental data.

3.3. Shrinkage profile of nanosilver paste

The thickness percentage of paste is expressed below:

$$P_h = (1-\varepsilon_z)\times 100\% = (1-\int_0^t \dot{\varepsilon}_z dt)\times 100\% \qquad \text{(Eq. 3.2)}$$

where P_h is the thickness percentage, ε_z and $\dot{\varepsilon}_z$ are the vertical strain and vertical strain rate of paste along Z-direction, respectively. According to Eq. 3.2, the thickness percentage of paste can be simulated during heating by monitoring the vertical strain rate. In the model, the strain rate along the z-direction $\dot{\varepsilon}_z$ is related to the distribution of viscosity (E), free strain rate ($\dot{\varepsilon}_f$) and external applied pressure (P_{apply}). Furthermore, the viscosity and free strain rate are functions of concentration of solvent (C_S). Therefore, a comparison of experimental and simulation results of paste shrinkage can be used to validate the model.

Fig. 3.4 shows the experimental results of the shrinkage of nanosilver paste in 1 × 1 mm^2, 3 × 3 mm^2, and 5 × 5 mm^2 chip attachments during the ramp-soak combined heating [86], and Fig. 3.5 presents the simulation results of paste shrinkage with the same

configuration of chip size and heating profile. Both the experimental and the simulation results show the same trend for each sample: the shrinkage was small in the first 40 minutes of heating (below 100 ℃) and then increased during the 100 ℃ soaking. The shrinkage rate further increased with increasing temperature, and within 60-85 minutes, the thickness dropped to 60%-65% of the initial thickness, and the shrinkage rate decreased. The experimental data show further shrinkage as the temperature reaches 275 ℃, the result of sintering densification, not solvent removal. Because the mechanism of sintering densification is not included in the model, the further shrinkage of paste is not shown in the numerical simulation.

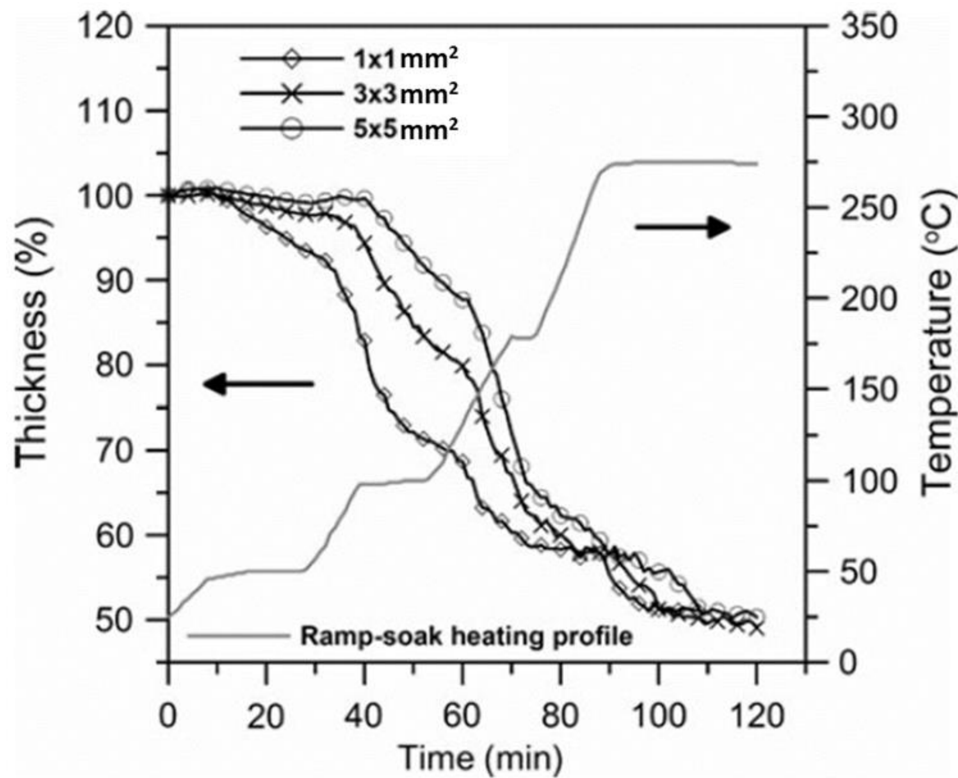

Fig. 3.4. Experimental results of thickness shrinkage for nanosilver paste in 1 × 1 mm^2, 3 × 3 mm^2 and 5 × 5 mm^2 chip attachments with heating profile 2 (ramp-soak heating).

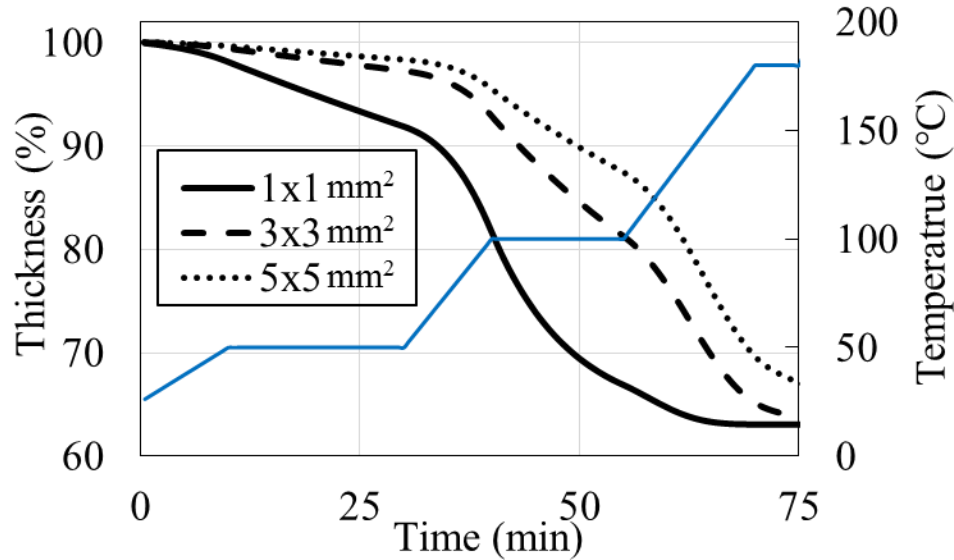

Fig. 3.5. Simulation results of thickness shrinkage of nanosilver paste in 1 × 1 mm^2, 3 × 3 mm^2, and 5 × 5 mm^2 chip attachments with heating profile 2 (ramp-soak heating).

The following conclusions can be drawn from the comparison:

(1). Both the experiments and the simulation results indicate the thickness change rate decreases with increasing the size of chip attachment.

(2). Both the experiments and simulation results show that the final thickness after drying (at 180 ℃) increases with increasing the size of chip attachment.

(3). The simulation shows the same trend as experiments below 180 ℃ during drying, indicating the model can reasonably simulate the paste drying process.

3.4. Stress evolution of nanosilver paste in the chip attachment

There are two different types of defects of nanosilver paste bond-line in the chip attachment: cracks in paste and delamination at the interface between the paste layer and the chip. Cracks are generated by the x-y in-plane internal stress σ_x or σ_y, and delamination is generated by the vertical internal stress σ_z. Through the analysis of

internal stresses, it is possible to determine the evolution of internal stress distribution of the nanosilver paste between the chip and the substrate during heating process. Though accurate failure criteria of cracking or debonding are not known yet, the evolution of stress distribution will help analyze and predict the possible locations at which the paste will crack or debond.

The drying of the nanosilver paste between a 10×10 mm^2 chip and substrate at 180 ℃ was simulated. Only a quarter of the paste was considered for the simulation thanks to symmetry. In the simulation, the quarter of paste was meshed to 50×50 grids, each 0.1×0.1 mm^2 in area. The evolution of the x-y in-plane and vertical internal stresses was monitored. The results are shown in Fig. 3.6 and Fig. 3.7. At the beginning of drying, the internal stresses at all locations were low. Because corners and edges were the locations at which the solvent can easily escape and deformation tend to occur, high stresses were generated first close to these locations. Then the high stresses were shifting to the center while the gradient of solvent concentration at the center increased because of diffusion. The internal stresses of the paste would finally relax to zero as all the paste was completely dried (no more change of strain) according to the viscous model.

Because the values of some of the model parameters used to calculate the internal stresses were only approximate, the simulated values of internal stresses were not very accurate. But the trend of stress evolution was correct and should provide some guidance to the stress analysis of the paste.

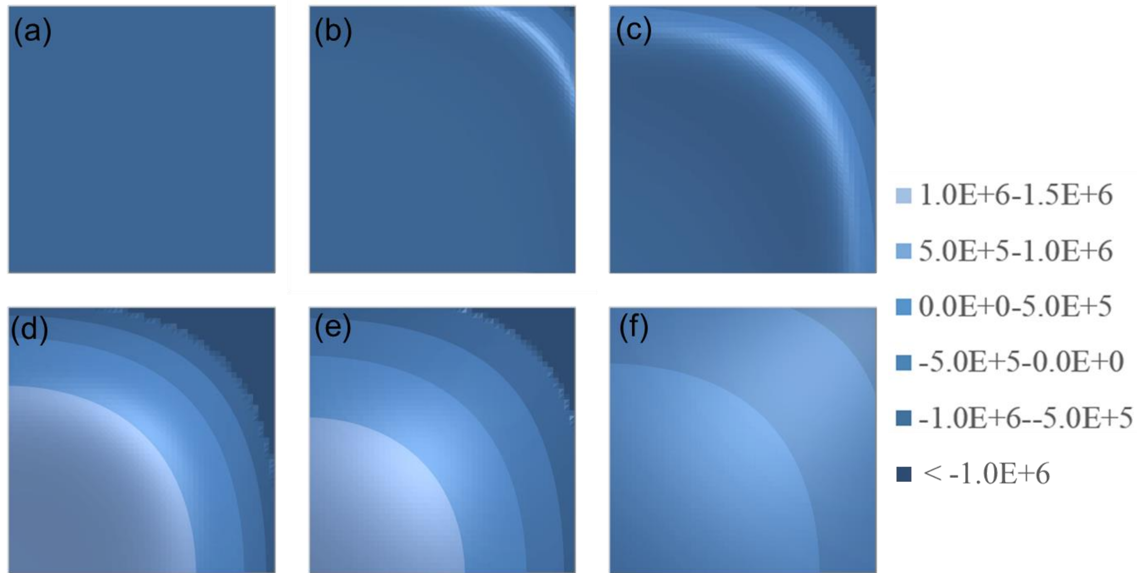

Fig. 3.6. Distribution of vertical internal stress of nanosilver paste in a 10×10 mm^2 chip attachment at 180 ℃ drying under zero external pressure for (a) 0 min, (b) 20 min, (c) 40 min, (d) 60 min, (e) 80 min, and (f) 100 min. For reason of symmetry, only a quarter of the paste is considered in the simulation. In each figure, the left bottom corner is the center of the chip and the right top corner is the corner of the chip.

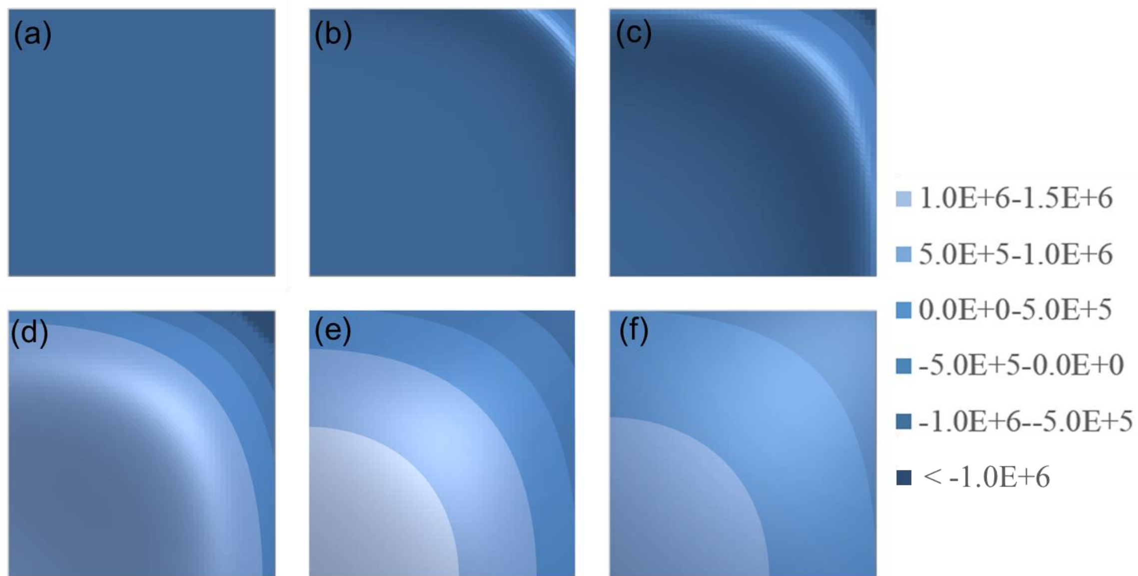

Fig. 3.7. Distribution of x-y in-plane internal stress of nanosilver paste in a 10×10 mm^2 chip attachment at 180 ℃ drying under zero external pressure for (a) 0 min, (b) 20 min, (c)

40 min, (d) 60 min, (e) 80 min, and (f) 100 min. For reason of symmetry, only a quarter of the paste is considered in the simulation. In each figure, the left bottom corner is the center of the chip and the right top corner is the corner of the chip.

The defect formation in the paste layer under a 10 × 10 mm^2 glass chip during 180 ℃ drying was shown in Fig. 3.8. Cracks are initially generated at the locations between a chip edge and the center and then moves to the center. Delamination also starts at the locations between a chip edge and the center, and the final delamination area covers most of the central area under the chip. These observations are in agreement with the predicted evolution of in-plane and vertical internal stresses.

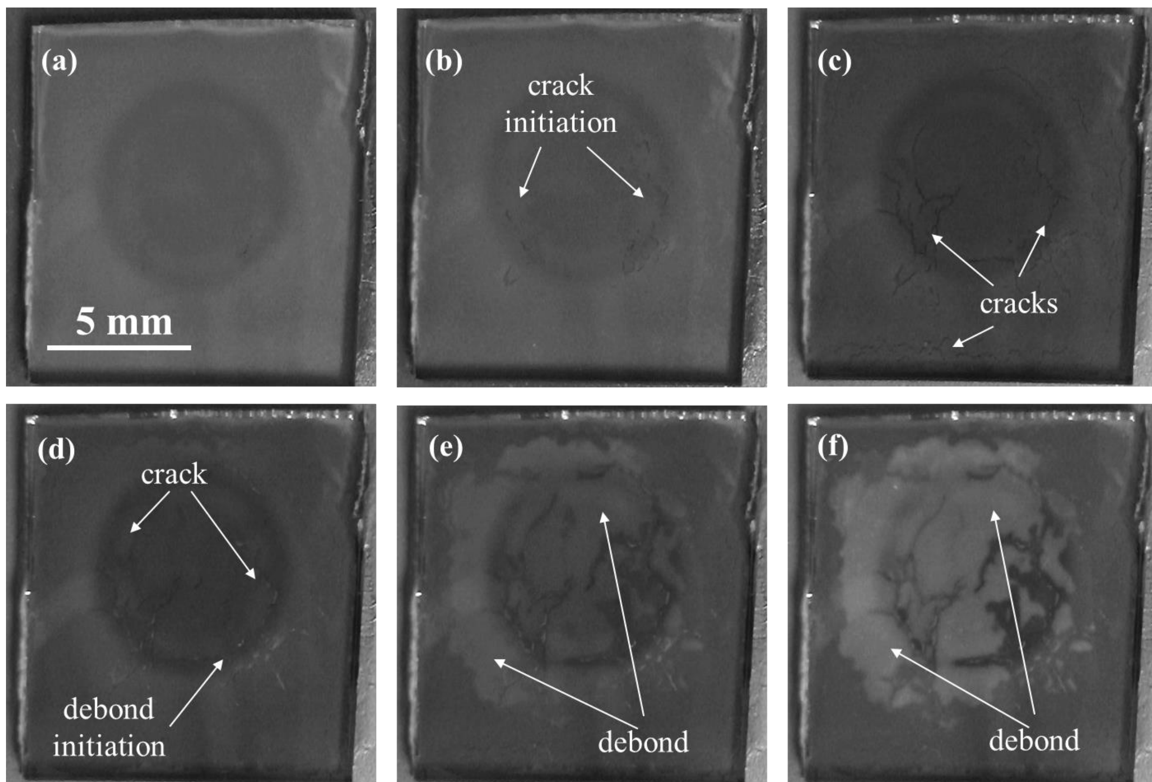

Fig. 3.8. Nanosilver paste under a glass chip showing defect formation during 180 ℃ drying. (a)-(f) are from the beginning to the end of drying, respectively.

3.5. Summary

In this chapter, the drying behavior of nanosilver paste in the chip attachment such as weight loss, shrinkage and internal stress evolution was demonstrated by numerical simulation based on the diffusion-viscous model for nanosilver paste drying. Several conclusions can be drawn:

The simulated weight loss profiles of nanosilver paste in the chip attachment under different drying process were in good agreement with the experiments, which verified the diffusion model of the drying behavior of nanosilver paste in chip attachment.

The simulated shrinkage profiles of nanosilver paste in the chip attachments with different chip sizes were in agreement with the experimental data during drying, which proved that the viscous model for stress-strain analysis of the nanosilver paste between the chip and the substrate is effectively accurate.

The simulated results showed that the evolution of the internal stress of nanosilver paste in the chip attachment, and the locations of high internal stress coincided with the locations of defect formation in experiment. It indicated that the model can effectively explain and predict the defect formation locations of nanosilver paste in the chip attachment during drying.

Chapter 4. Design of experiments (DOE) study on nanosilver LTJT

4.1. Introduction

The process parameters of nanosilver LTJT play important roles in the bonding quality of the large-area chip attachment. Therefore, the evaluation of different process parameters of naosilver LTJT is crucial for optimizing the process profile of nanosilver LTJT. In this chapter, a fractional factorial design of experiments was applied to evaluate the effects of pressure, temperature and time on the bonding quality of sintered nanosilver chip attachments. The experiments helped to identify the importance and interaction of various processing parameters on the bonding strength and microstructure of sintered nanosilver joints. Based on the experiments, an improved process profile of nanosilver LTJT for large-area chip attachment was developed.

4.2. Experimental procedures

4.2.1. Sample preparation

Samples were fabricated by bonding alumina mechanical chips on an alumina direct-bond-copper (DBC) substrate by using the nanosilver paste that can be sintered at low temperature. The silver paste, known as nanoTach, was supplied by NBE Technologies, LLC, Blacksburg, Virginia. The copper layer thickness on the DBC substrate was 200 μm, and the sandwiched alumina thickness was 380 μm. The thickness of the mechanical chips was 1000 μm, which was preferred for ease of die shearing. The surfaces of the DBC copper and the mechanical chips were metalized with silver of a few hundred nanometers thick. The lateral dimensions of a typical sample were 10×10 mm^2 for a

mechanical chip mounted on 14 $\times$ 14 mm^2 of DBC substrate. Chip-joint layer-substrate structure is shown in Fig. 4.1.

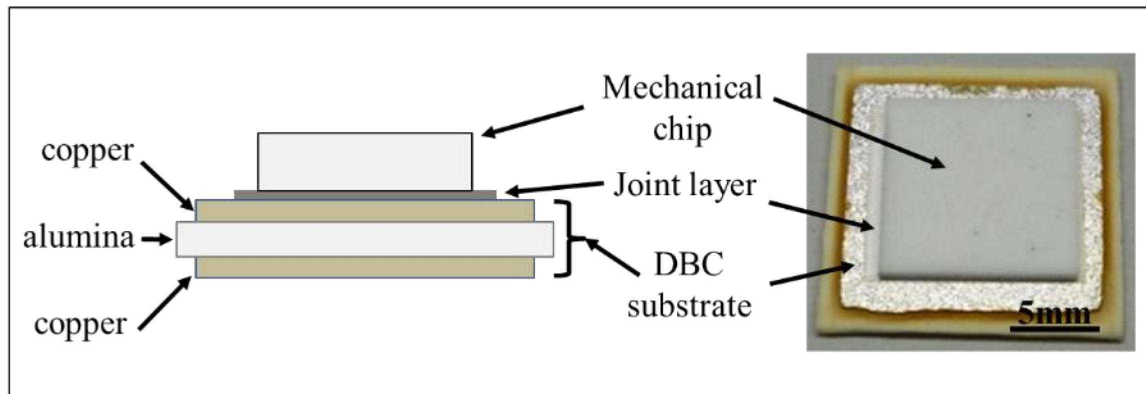

Fig. 4.1. Left is the schematic of samples structure, and right is the top view of a fabricated sample.

To assemble a sample, the silver paste was applied on a DBC substrate by a double print process. Fig. 4.2 shows the flowchart of the double print process for the fabrication of the test samples. Initially, a layer of the paste was stencil printed on the substrate by using a metal squeegee to a wet thickness of 50 μm and dried by heating at a ramp rate of 5 ℃/min to 180 ℃ with a dwell time of 5 minutes. After cooling down to room temperature, a second layer was printed on the dried layer by using a rubber squeegee to an estimated wet thickness of 5 μm. Then, a mechanical chip was mounted on the wet print. The assembled part was rapidly heated from room temperature to 180 ℃ on a preheated hot plate, followed by heating at 275 ℃ on another heated plate, to dry and sinter the paste, respectively. It took anywhere from 30 to 60 s for the sample to reach the preset temperature. Uniaxial pressure was applied simultaneously either during the drying or sintering phase of the LTJT process. The schematic view of the heating profiles is shown in Fig. 4.3. Typical sintered thickness of the silver layer is from 15 to 20 μm [87]. To evaluate the effect of processing pressure, temperature, and time on the sintered silver

joint, samples were fabricated with different drying and sintering pressure-time combinations as listed in Table 4.1. For each process parameter combination, three samples were fabricated.

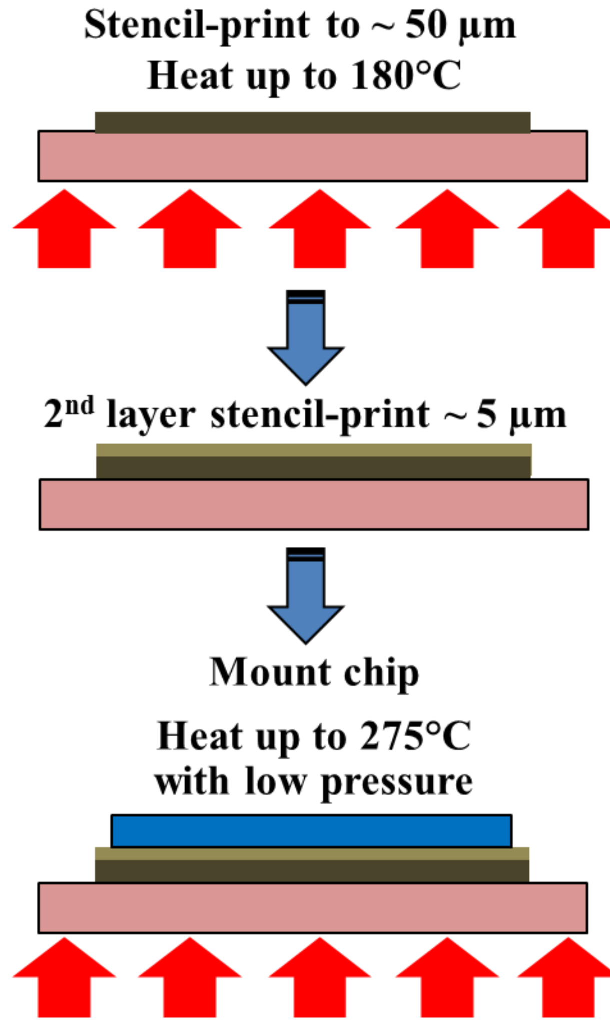

Fig. 4.2. Flowchart of the double print process for the fabrication of test samples under different applied pressures and sintering times.

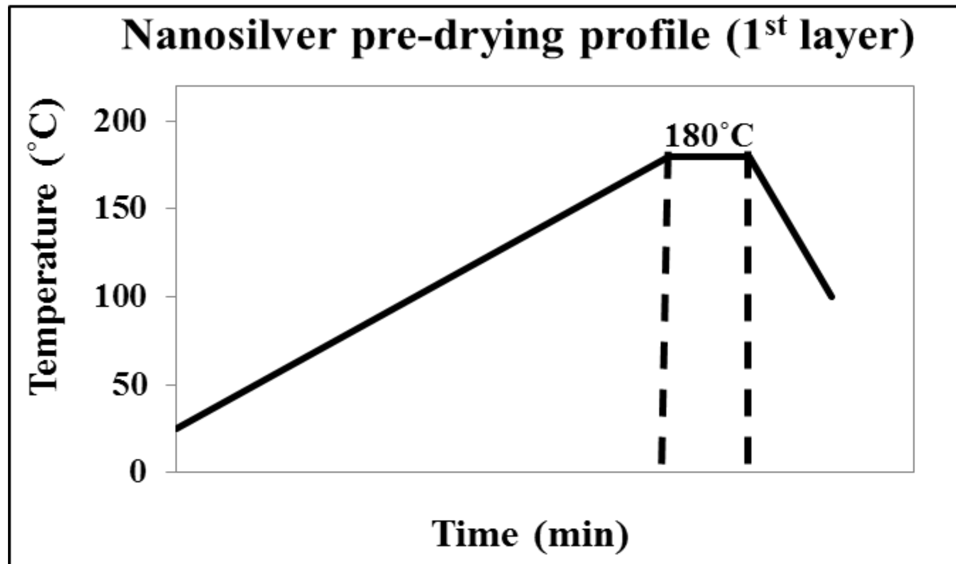

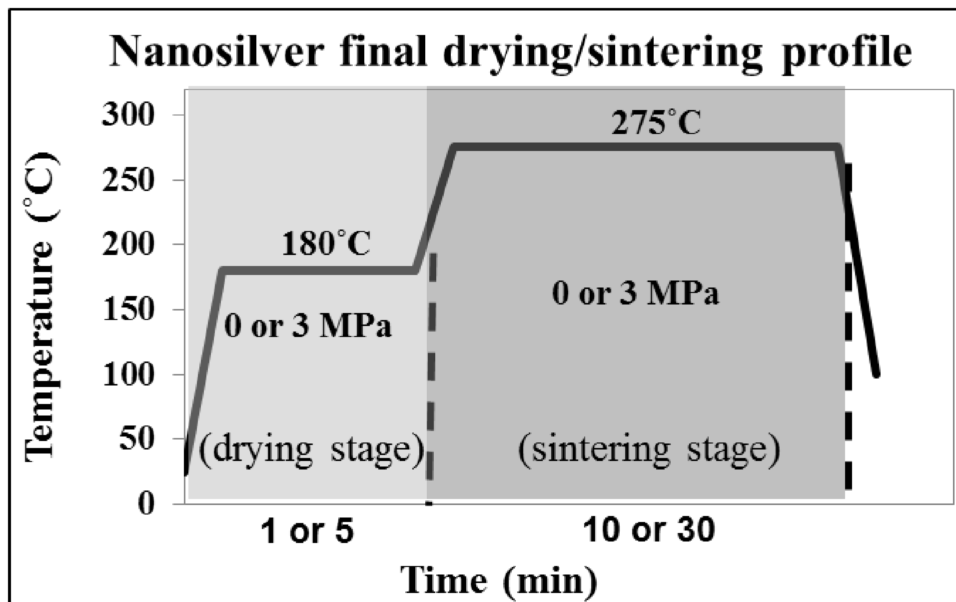

Fig. 4.3. Heating profiles for nanosilver 1st layer drying and final drying/sintering in attachment process.

Table 4.1: Designed combinations of process parameters.

Group No.	Drying time t_D (min)	Drying pressure P_D (MPa)	Sintering time t_S (min)	Sintering pressure P_S (MPa)
A	1	0	30	0
B	5	0	30	3
C	1	3	30	3
D	5	3	30	0
E	1	0	10	3
F	5	0	10	0
G	1	3	10	0
H	5	3	10	3

4.2.2. Die-shear testing

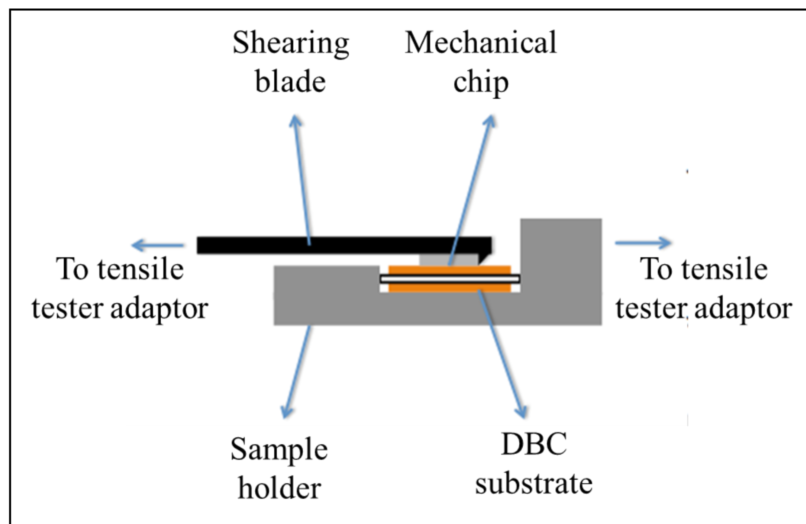

Fig. 4.4. The schematic of chip attachment in fixture for die-shear testing.

Mechanical properties of both the sintered nanosilver bare layer (as shown in Appendix B) and the sintered nanosilver bond-line in the chip attachment can be determined by the mechanical tests. In this study, a ComTen 95 series tester (ComTen Industries, Pinellas Park, FL) was applied for the die-shear test, and the test was conducted at a constant

shear speed rate of 8×10^{-5} m/s. Fig. 4.4 shows the schematic of chip attachment in the fixture for die-shear test, and Fig. 4.5 shows the die-shear fixture and die-shear tester.

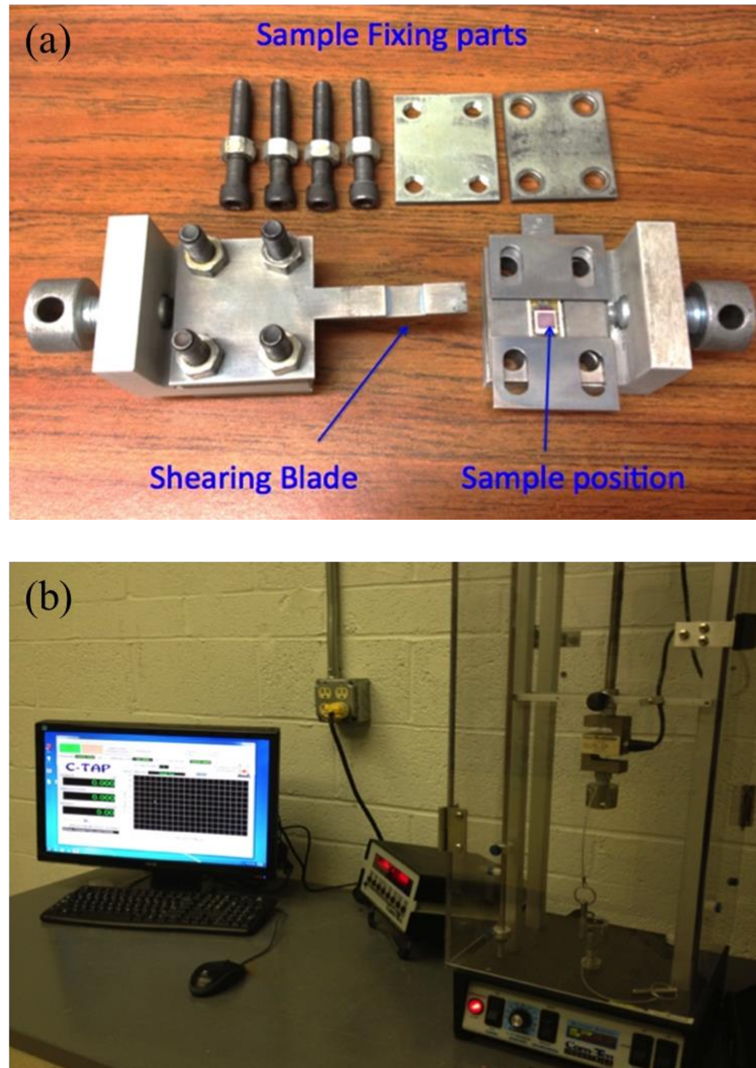

Fig. 4.5. (a) is the fixture to hold and shear chip attachment samples, and (b) is ComTen 95 series tester for die-shearing.

4.2.3. X-ray CT characterization

X-ray CT is an ancillary technique for nondestructive bonding characterization of chip attachment. Another nondestructive bonding characterization technique is curvature measurement, which was demonstrated in Appendix C. X-ray CT is a nondestructive

method for imaging the internal bond-line structure such as the voids/cracks in the attachments that may form in a sintered silver attachment layer. Three-dimensional virtual images of the bond-line layer can be obtained by reconstructing the transmission X-ray photos taken from different angles, thus enabling the determination of the exact locations and extent of defects within the silver layer. In this study, a MicroXCT 400 from Xradia Company was used for the X-ray CT scanning. Fig. 4.6 shows the test equipment. Both the transmission images showing the whole sample and virtual sliced images showing the localized interface area were obtained.

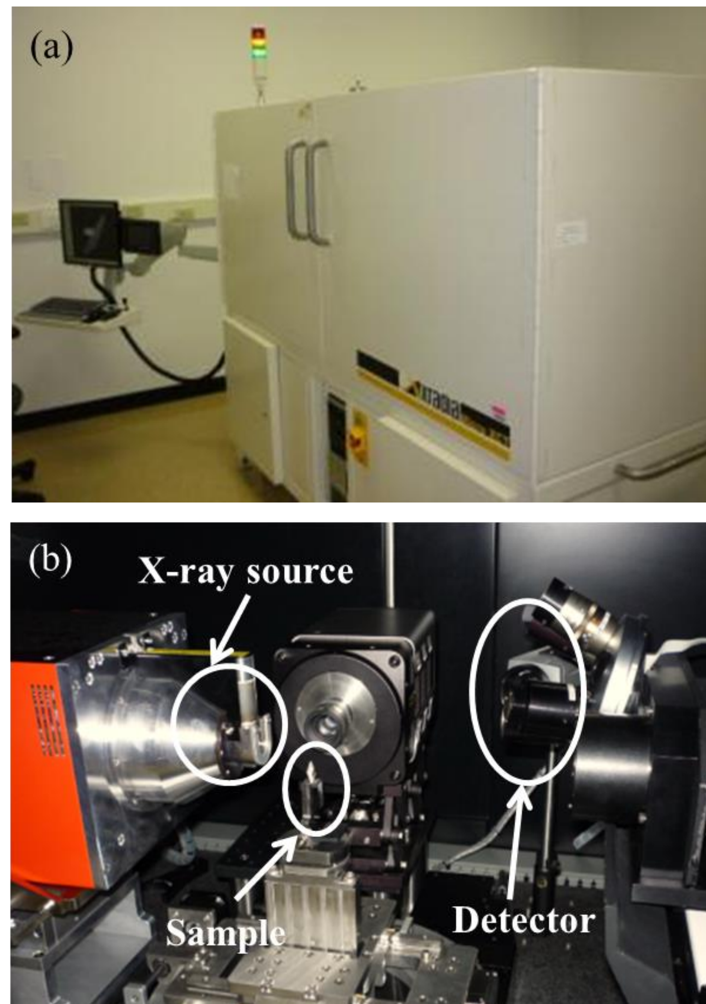

Fig. 4.6. (a) is the MicroXCT 400 (Xradia) equipment used for X-ray imaging of sintered samples, and (b) is the major components inside X-ray equipment chamber.

4.3. Results and discussion

4.3.1. Bonding strength of sintered silver joints

The die-shear testing results of samples processed in the processing combination groups are shown in Table 4.2. Since the processing parameter combinations were based on a fractional factorial design, it is possible to use the corresponding test results to analyze the statistical significance of each processing parameter on the bonding quality, as well as the interaction between the parameters.

Table 4.2: Die-shear strengths of samples fabricated under different process profiles.

Group No.	Drying time t_D (min)	Drying pressure P_D (MPa)	Sintering time t_S (min)	Sintering pressure P_S (MPa)	Die-shear Strength (MPa)		
A	1	0	30	0	5.3	16.5	11.3
B	5	0	30	3	30.1	31.1	31.6
C	1	3	30	3	32.8	39.0*	30.4
D	5	3	30	0	33.6*	35.6	34.2*
E	1	0	10	3	25.0*	11.2	14.0
F	5	0	10	0	6.6	5.1	4.7
G	1	3	10	0	5.6	19.9	10.7
H	5	3	10	3	35.5*	39.9*	32.1

"*" represents that the mechanical chip cracked during test.

Plot of main effect for each factor are shown in Fig. 4.7. The results show that die-shear strength of the sintered assembly is affected by drying time, drying pressure, sintering time and sintering pressure. For example, the average die-shear strength is 19 MPa for 1 minute drying, and 28 MPa for 5 minutes drying, which indicates that in the range investigated drying time is critical to obtaining high die-shear strength. A similar trend is observed for each of the other parameters, with the upper level producing higher die-

shear strength. The higher the pressure and the longer the time in either the drying or sintering stage, the higher the die-shear strength.

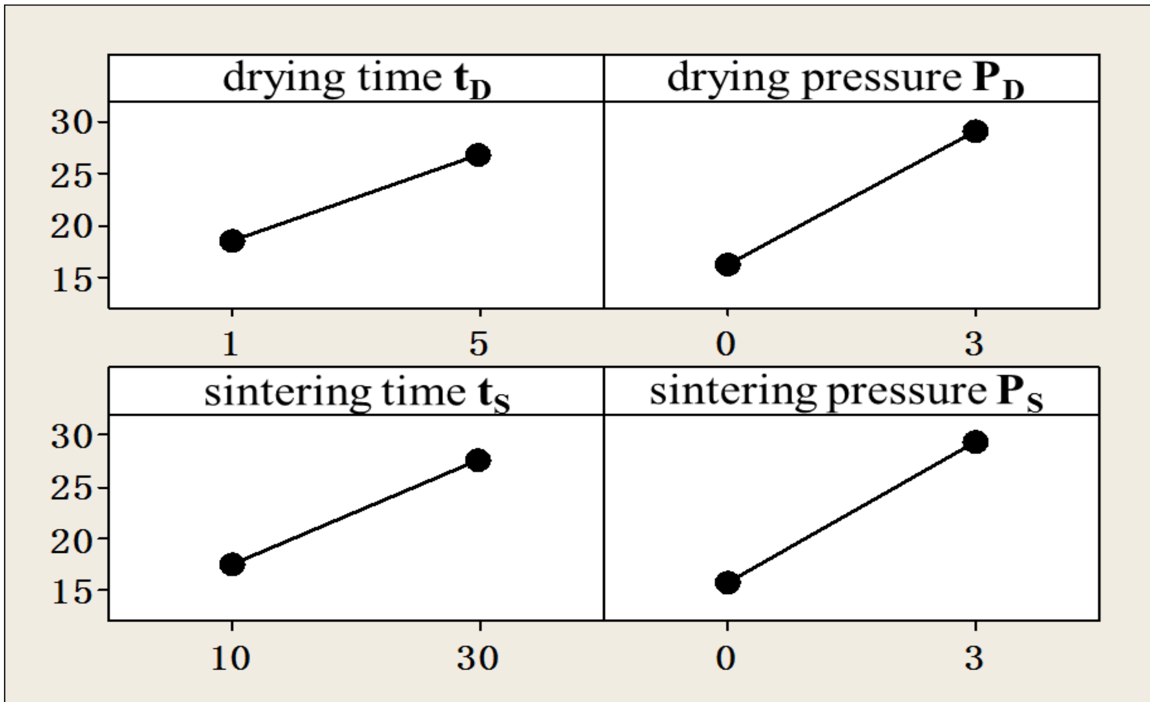

Fig. 4.7. Plot of average die-shear strength corresponding to different drying time, drying pressure, sintering time and sintering pressure, showing the main effect of each factor on die-shear strength.

Fig. 4.8 shows the interaction between different process parameters. Parallel lines of different parameters indicate no interaction, whereas a big angle formed between different lines of factors indicates strong interaction. For example, in the group of drying time (**t_D**) versus sintering time (**t_S**), increasing sintering time from 10 to 30 minutes under 1 minute drying time results in a 9.8 MPa increase in die-shear strength, whereas those under 5 minute drying time results in a 10.3 MPa increase. This gave two nearly parallel lines, indicating that statistically, sintering time and drying time have an insignificant effect on each other. Similarly, moderate interaction (caused ±7 MPa difference in die-

shear strength within the evaluated conditions) is found between drying pressure and drying time, as well as sintering pressure and sintering time. The interaction analysis indicates that no strong interaction is found between any two of these processing parameters. The implication is that changing one parameter while keeping the rest constant would produce changes to the die-shear strength that can be attributable to only that parameter. Therefore, assessing the effect of each parameter and deciding on how best to modify the sintered chip attachment process can be made simpler by the behavior exhibited by the sintered nanosilver paste.

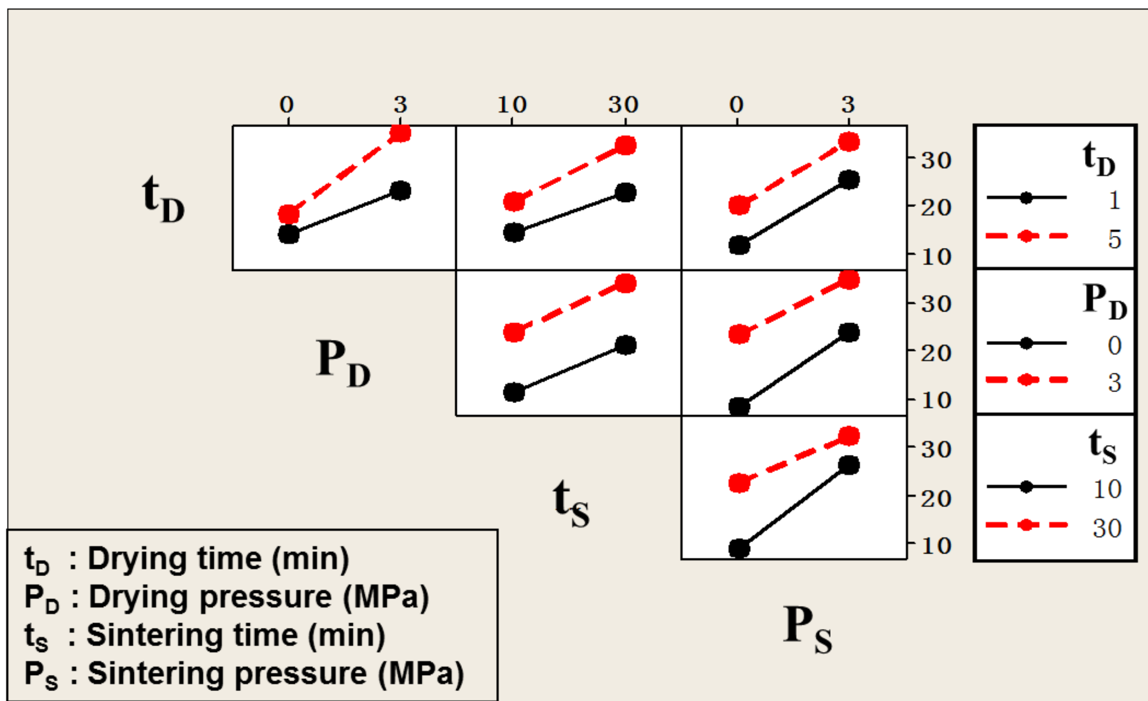

Fig. 4.8. Interaction plot between factors of drying time (**t_D**), drying pressure (**P_D**), sintering time (**t_S**) and sintering pressure (**P_S**), in which no strong interaction was detected between any two process parameters.

Another way to look at the significance of the processing parameters is the analysis of variance (ANOVA) approach by computing F as shown in Table 4.3. It can be seen that

the confidence levels for all the individual effects exceed 95%, as well as the interaction between drying time (**t_D**) and drying pressure (**P_D**), and between sintering time (**t_S**) and sintering pressure (**P_S**). All the others show less significant effect. Since the experiment was a fractional factorial design, some of the computed interaction values are the same.

Table 4.3: Analysis of Variance (ANOVA) computation of the significance of individual factors and interactions.

Source of variation	Degrees of freedom	Sum of squares	Mean square	F	Confidence level %
t_D	1	403.44	403.44	22.2257	99.96
P_D	1	1024.43	1024.43	56.4363	99.99
t_S	1	612.06	612.06	33.7187	99.99
P_S	1	1115.21	1115.21	61.4374	99.99
$t_D \times P_D$ (or $t_S \times P_S$)	1	90.48	90.48	4.9847	95.62
$t_D \times t_S$ (or $P_D \times P_S$)	1	22.81	22.81	1.2569	71.75
$t_D \times P_S$ (or $P_D \times t_S$)	1	0.28	0.28	0.0155	9.72
Error	13	235.98	18.15		
Total	23	3618.27			

4.3.2. Structure of the sintered silver bond-line

Transmission X-ray images of samples processed according to the parameters listed in Table 4.1 are shown in Fig. 4.9. In the transmission mode, the lighter areas in the image indicate the presence of voids, cracks, or material of lower density. A nearly crack/void free bond-line structure can be obtained for the samples in groups D and H. From the processing-microstructure-property relationships perspective, it is realized that with a

drying process at 180 ℃ under a pressure of over 3 MPa lasting 5 minutes, regardless of whether a pressure was applied or not during sintering, a uniform bond-line nearly crack/void free can be achieved. Since the die-shear strengths of these samples are all over 30 MPa, it can be conclude that a uniform structure without major defects will lead to high bonding strength. Two other different types of bond-line structures can be seen from Fig. 4.9: for samples in groups A and F, big and small cracks/voids are present throughout the layer; for samples in groups B, C, E and G, moderately cracked bond-line is present.

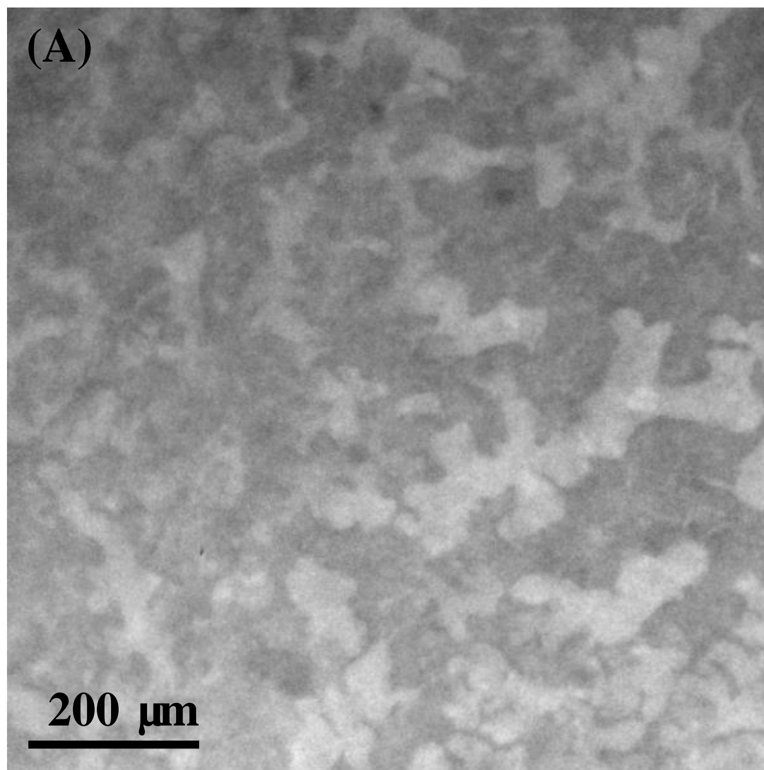

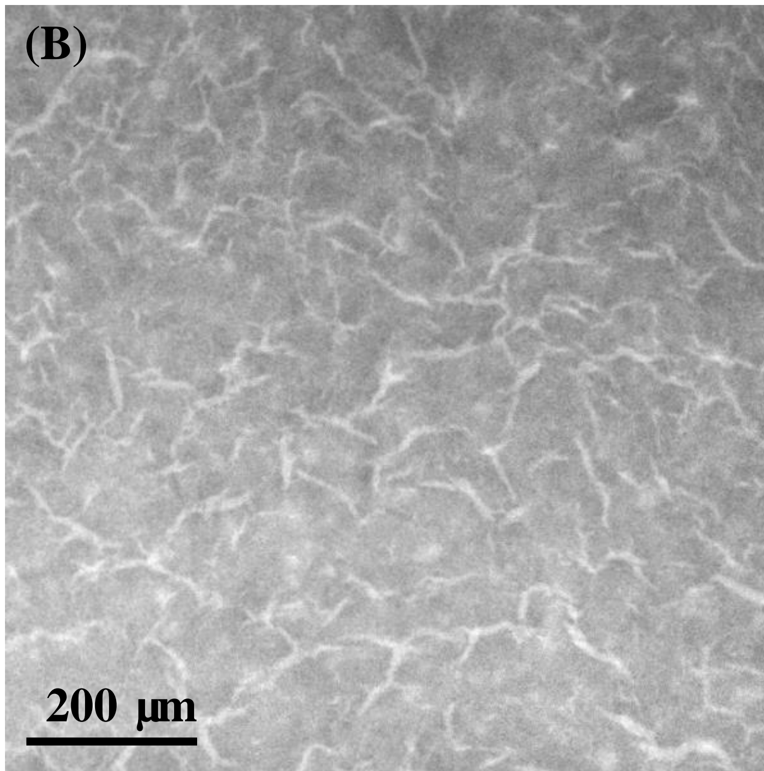
(B)
200 µm

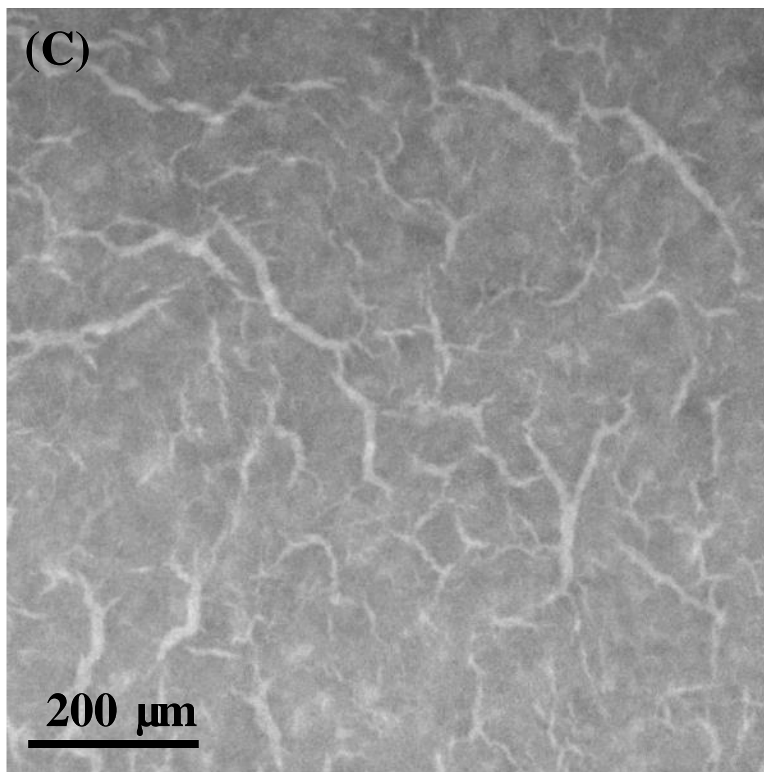
(C)
200 µm

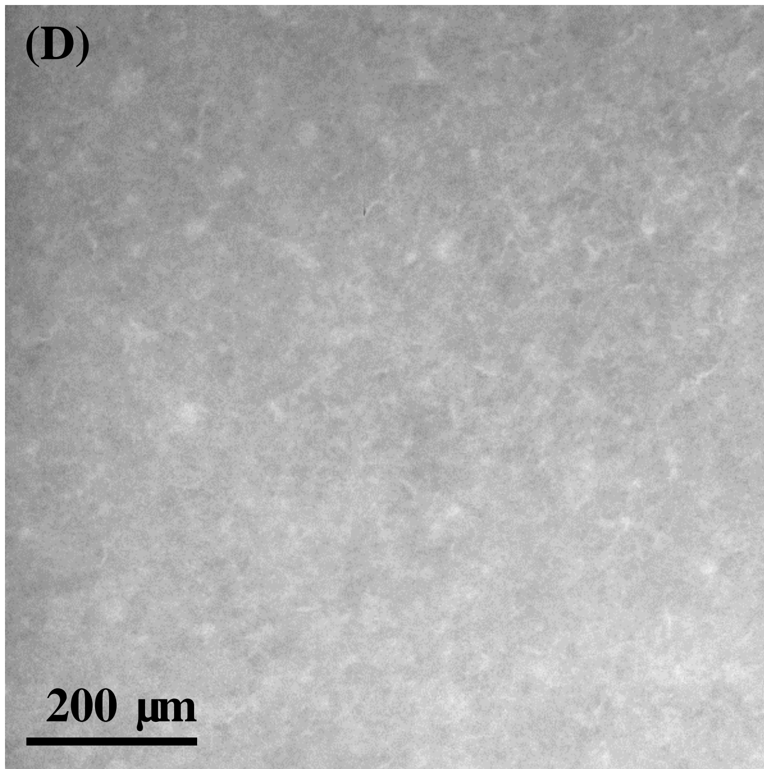
(D)
200 μm

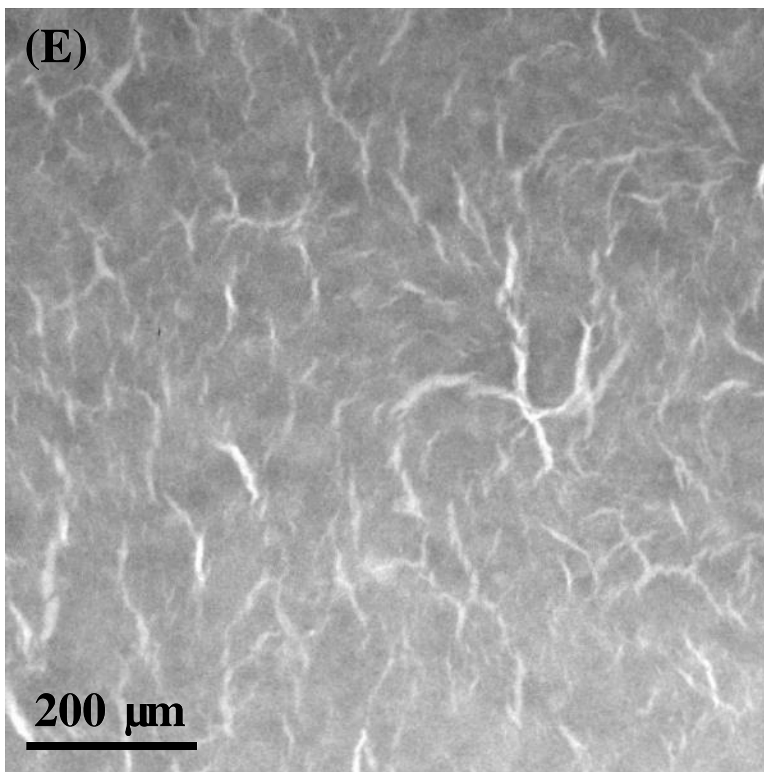
(E)
200 μm

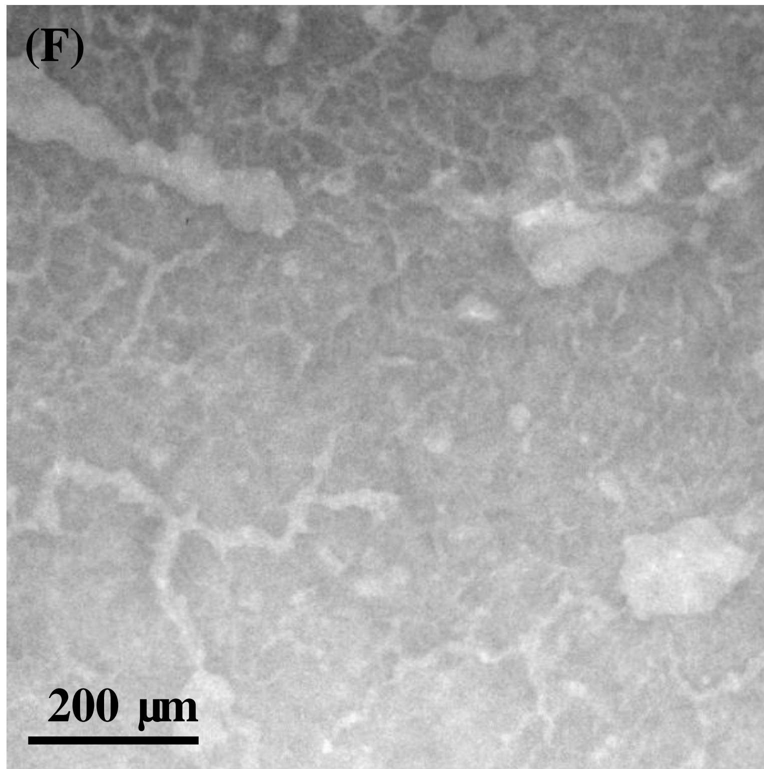
(F)
200 µm

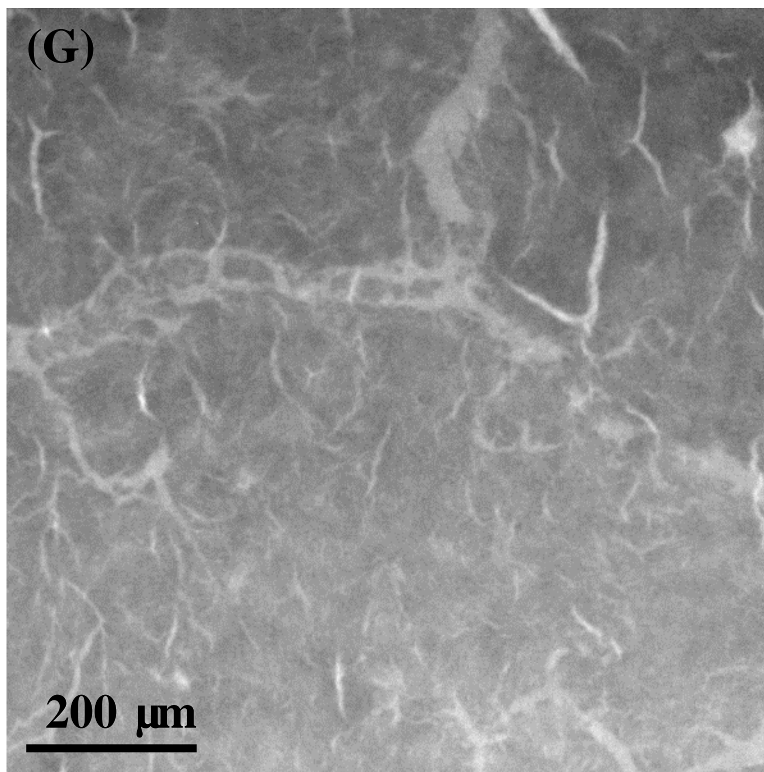
(G)
200 µm

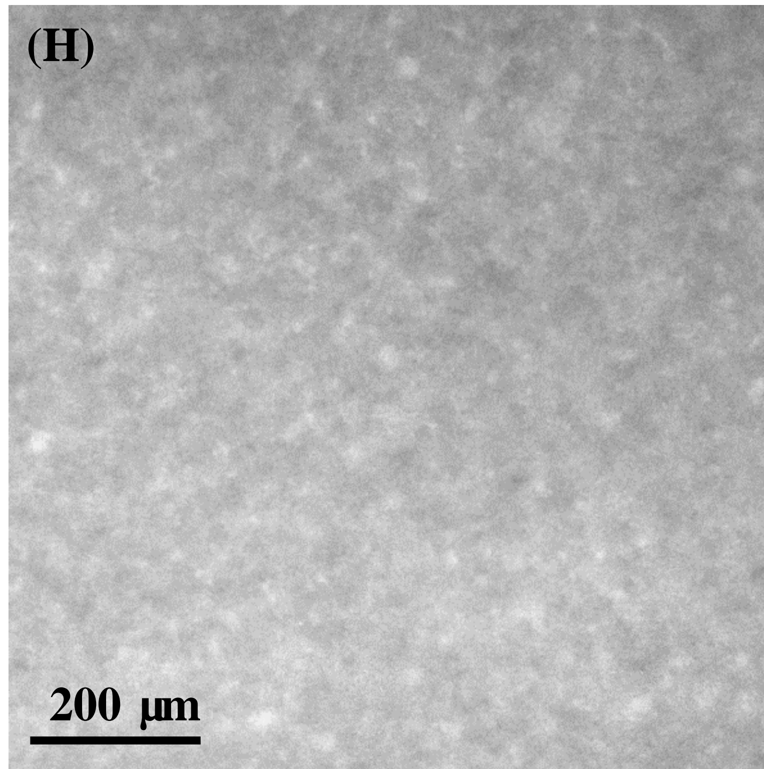

Fig. 4.9. X-ray transmission images of sintered sample from groups A to H, showing different microstructures of sintered silver layers: few tiny cracks are showing in group D and H; big cracks and voids are showing in group A, and F; moderate cracks are showing in group B, C, E, and G.

3D reconstructed X-ray images of samples in group F, E, and D were shown in Fig. 4.10 to further prove the difference of microstructures. A bond layer with a preponderance of defects is likely to have less intimate contact with the bonding surfaces, leading to weak sintered bonds. Unlike the soldering process where any trace of the initial structure is obliterated once the solder melts, during solid-state sintering, most of the large defects, such as drying cracks and printing or deposition voids, are retained in the final microstructure. Delamination of the joint layer before sintering is not fully reversed by the relatively low pressure applied during sintering.

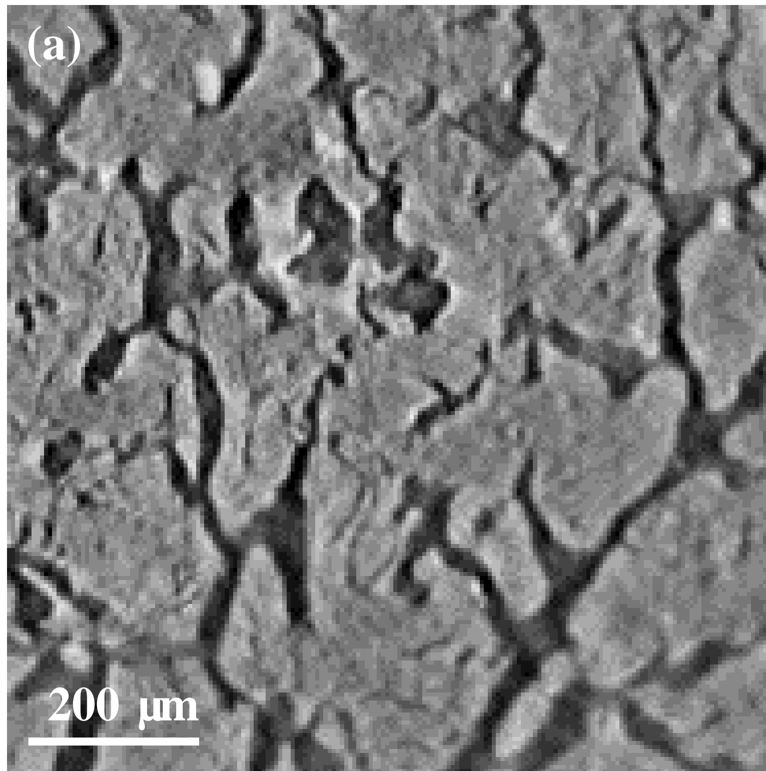
(a)
200 µm

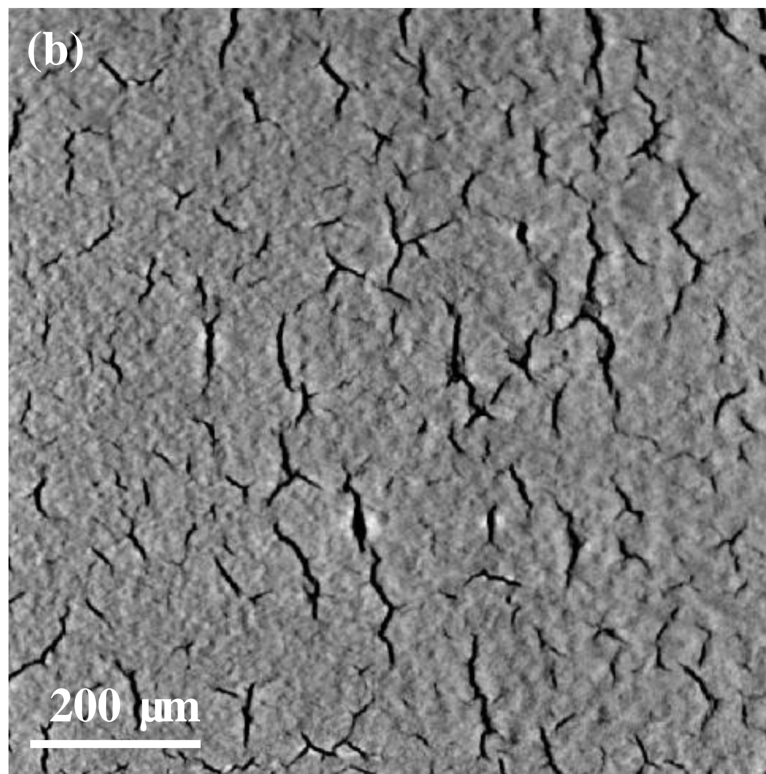
(b)
200 µm

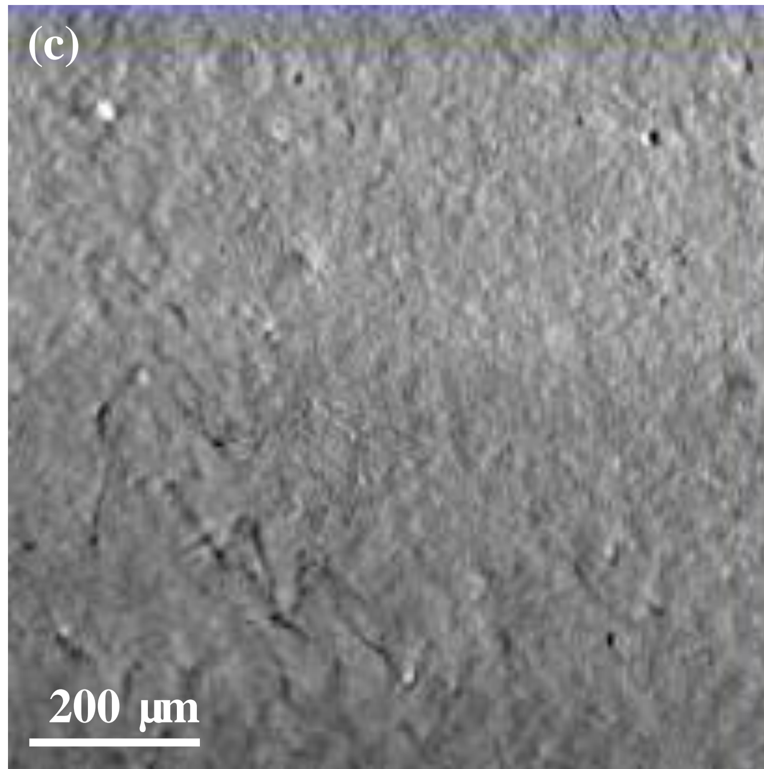

Fig. 4.10. X-ray reconstructed images of sintered silver joint layers from samples in (a) group F, (b) group E and (c) group E, showing big cracks/voids, moderate cracks and tiny cracks/voids, respectively. Light color regions in the images represent silver layers and dark color regions represent voids and cracks.

4.3.3. Development of nanosilver LTJT process

Based on the design of experiments study, it is indicated that long drying and sintering time with high drying and sintering pressure will lead to both high quality bond microstructure and bonding strength. Since there is no strong interaction between any of the two process parameters, the bonding quality can be controlled by simply changing one process parameter without affecting others. To compromise processability with qualitative bonding, it is determined that a nanosilver LTJT process consisting of pressure drying at 180 ℃ under 3 MPa for 5 minutes followed by pressureless sintering at

275 ℃ is sufficient to achieve a die-shear strength greater than 30 MPa with nearly perfect, crack- or void-free joint layer for chip sizes of up to 10 $\times$ 10 mm^2.

4.4. Summary

In this chapter, a design of experiments involving hot-pressing process parameters of nanosilver LTJT was carried out. The analysis shows that bonding quality increases with all evaluated process factors (drying time, drying pressure, sintering time, and sintering pressure), which means all the evaluated factors have significant effects on the bonding quality of sintered silver joints. No strong interaction is detected between any two factors. Based on the DOE study, an improved nanosilver LTJT process which limits the external applied pressure to a temperature below 200 ℃ was developed. A nearly perfect, crack/void free joint layer with over 30 MPa bonding strength can be obtained for large-area chip (up to 10 $\times$ 10 mm2) attachment with this process.

Chapter 5. Effect of external applied pressure during drying on sintered silver bond-line

5.1. Introduction

In Chapter 4, the design of experiments showed the preliminary results that the external applied pressure during drying helps increase the bonding strength of sintered nanosilver joint. In this chapter, a series of experiments that focuses on the external applied pressure during drying was carried out. Samples were fabricated with different drying pressures and sintered under no pressure in order to demonstrate the effects of drying pressure only. The experimental results were analyzed by the diffusion-viscous model and compared with the simulated results.

5.2. Experimental procedures

5.2.1. Sample Preparation

The test samples consisted of DBC substrate and alumina chips bonded together with sintered nanosilver paste. The silver paste was provided by NBE technologies, LLC, Blacksburg, Virginia, with the trade name of nanoTach®. The thickness of the copper and alumina layers of DBC were 200 μm and 380 μm, respectively. In lieu of actual devices, 1000 μm thick alumina chips were used. The DBC substrate had a coating of silver while the alumina chips were coated with a metallization consisting of 150 nm Cr, 200 nm Ni and 250 nm Ag in succession by physical vapor deposition (PVD). The silver coatings were necessary for adhesion to the sintered silver. The DBC substrates and alumina chips were cut into 14×14 mm^2 and 10×10 mm^2 pieces, respectively, for sample fabrication.

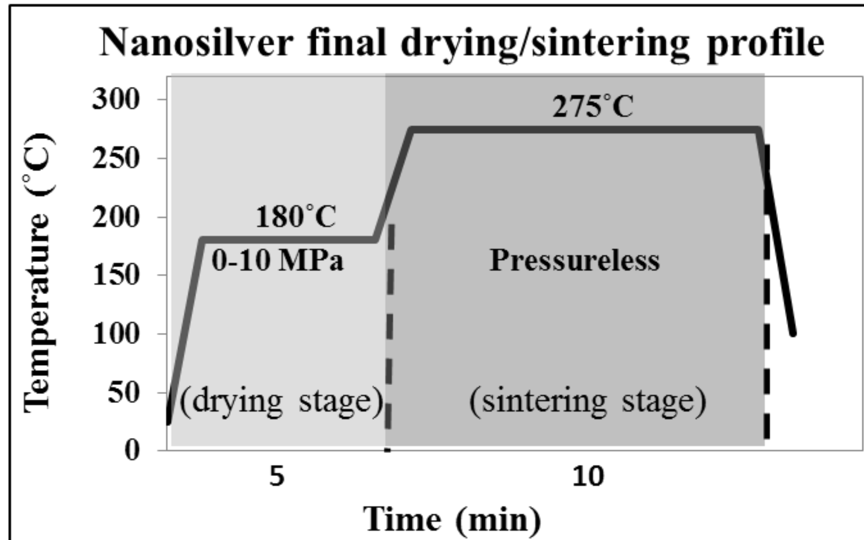

Fig. 5.1. Heating profile of chip attachment after chip mounting to substrate.

The silver paste attachment layer was deposited as a double print on the DBC substrate. An initial layer of nanosilver paste was printed with a wet print thickness of 50 μm and dried at 180 ℃ for 5 minutes after heating at a ramp rate of 5 ℃/min. The second layer was printed on the dried paste with an estimated wet print thickness of 5 μm. The alumina chip was mounted on the printed paste, and the assembly was heated at 180 ℃ for 5 minutes and then at 275 ℃ for 10 minutes. In order to evaluate the effect of external pressure during the drying stage on the quality of final bond-line, a uniaxial pressure from 0 to 10 MPa was applied at 180 ℃ heating. The schematic of heating profile is shown in Fig. 5.1. A press with a heated plate was used for pressure drying, as shown in Fig. 5.2. Four replicates were fabricated for each drying pressure condition, as three for die-shear testing, and one for SEM characterization.

Fig. 5.2. Hot press used for applying uniaxial pressure during assembly heating.

5.2.2. Die-shear testing

A ComTen 95 series tester (ComTen Industries, Pinellas Park, FL) was applied to measure the die-shear strength of the sintered assemblies. The test was conducted at a constant shear speed rate of 8×10^{-5} m/s. A die-shear fixture was used to hold the sample for shearing, as mentioned in Chapter IV. Fig. 4.5 shows the die-shear fixture and die-shear tester.

5.2.3. Microstructure Characterization

The Fabricated samples were firstly checked by X-ray CT to observe whether voids or cracks were generated in the sintered silver joints. A MicroXCT 400 from Xradia company were applied for the X-ray CT characterization. The microstructures of the

sintered joint layers were then obtained by SEM observations of cross sections of fractured samples. Sintered samples were mounted in the molding compound. After curing, the samples were cross-sectioned along the central line with a diamond saw. The exposed surfaces were polished with SiC sand papers down to 1200 grit and were further polished to 0.05 μm with a diamond suspension. A LEO 1550 FE-SEM from Zeiss was used for microstructure characterization.

5.2.4. Numerical simulation of stress evolution

Numerical simulation of internal stress evolution of nanosilver paste during drying process was applied. According to the sample preparation procedures of “double print”, the initial solvent concentration of nanosilver paste in the chip attachment was estimated to be 0.015. The input parameters nanosilver paste drying are shown in Table 5.1.

Table 5.1: Input parameters of nanosilver chip attachment during drying

	Case 1	Case 2	Case 3	Case 4	Case 5
Meshing of grids (quarter chip)	50×50	50×50	50×50	50×50	50×50
Chip dimension (mm^2)	10×10	10×10	10×10	10×10	10×10
Initial solvent concentration	0.015	0.015	0.015	0.015	0.015
Initial temperature (K)	453	453	453	453	453
Temperature ramp rate (K/s)	0	0	0	0	0
Initial pressure (Pa)	0	1×10^6	3×10^6	5×10^6	10×10^6
Pressure ramp rate (Pa/s)	0	0	0	0	0
Time duration (s)	300	300	300	300	300

5.3. Results and Discussion

5.3.1. *Die-shear strength*

The relationship between the die-shear strength of sintered silver joints and external applied pressure during drying process are shown in Fig. 5.3, the average die-shear strength increases almost linearly with increasing drying pressure. The die-shear strength of the samples fabricated under 0 MPa drying pressure is 5.8 MPa and increases nearly 10 times to 53.8 MPa under a drying pressure of 10 MPa during sample fabrication. The observed behavior indicates that the bonding strength can be manipulated by controlling the pressure during the drying stage.

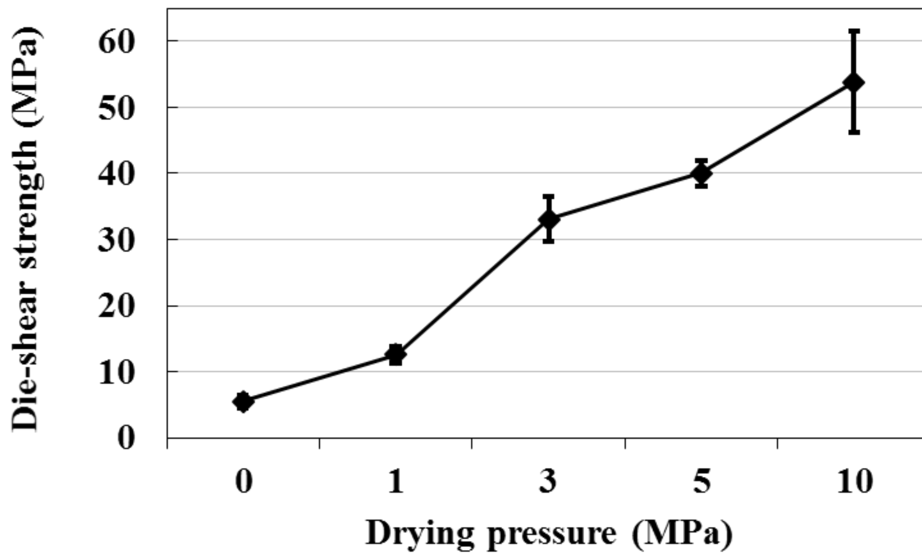

Fig. 5.3. Die-shear strength of samples fabricated under different drying pressures. Drying time and sintering time were set for 5 minutes and 10 minutes, respectively. No pressure was applied during the sintering stage.

5.3.2. *Microstructure of sintered silver joint*

Transmission X-ray images of samples processed with different drying pressure are shown in Fig. 5.4. In the transmission mode, the lighter areas in the image indicate the

presence of voids, cracks, or material of lower density. For samples fabricated with external applied pressure below 3 MPa during drying, defects of voids and cracks can be observed in the sintered silver bond-line. The portion of defects decreases with increasing the external applied pressure during drying. A nearly crack/void free bond-line structure can be obtained for the samples fabricated with external applied pressure above 3 MPa during drying.

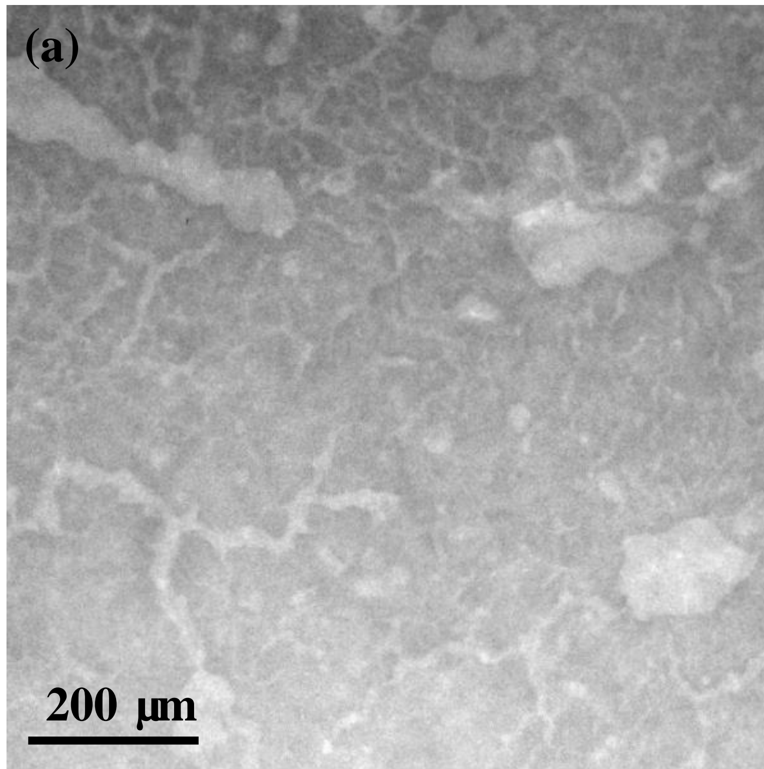

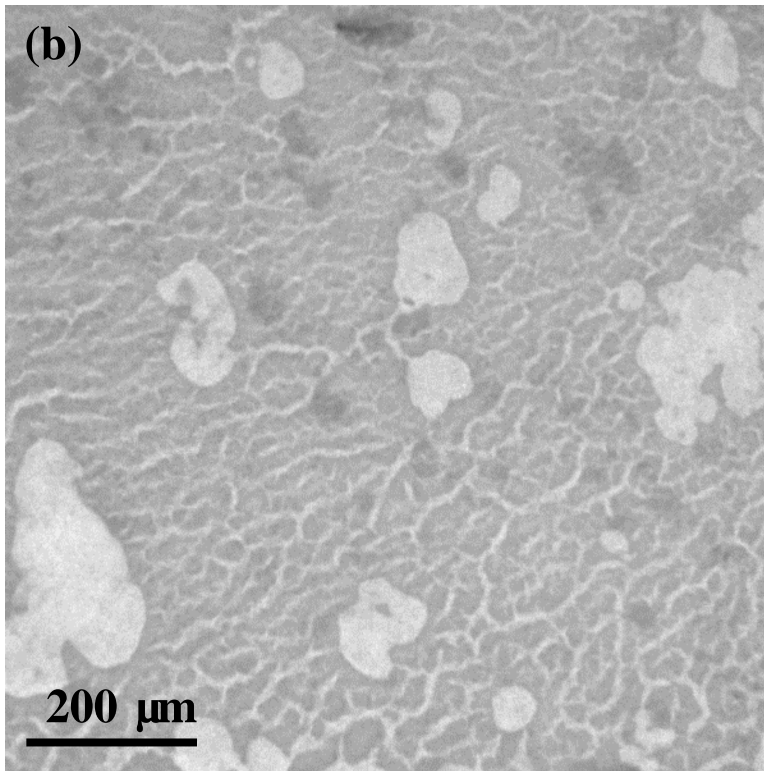
(b)
200 µm

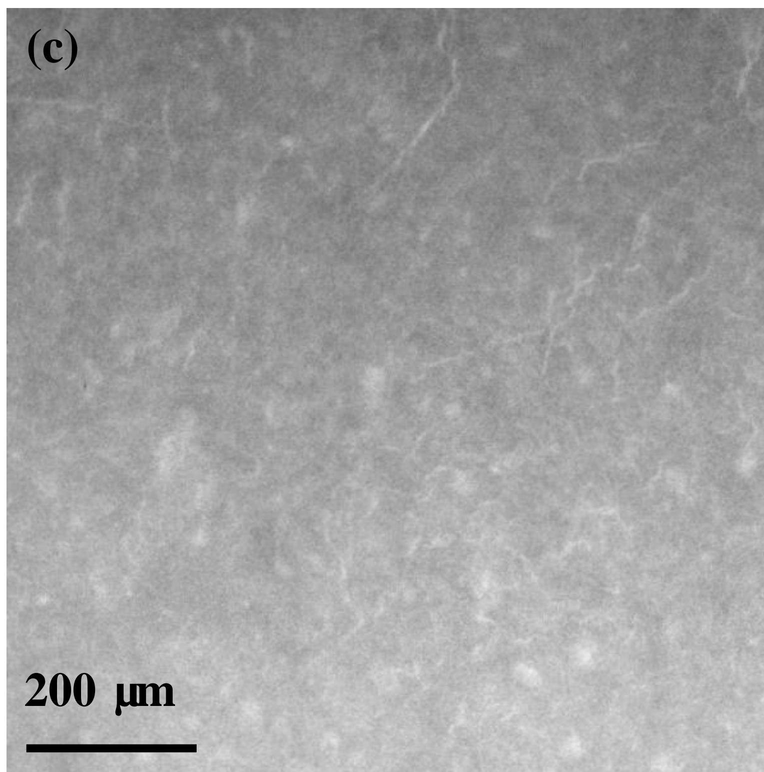
(c)
200 µm

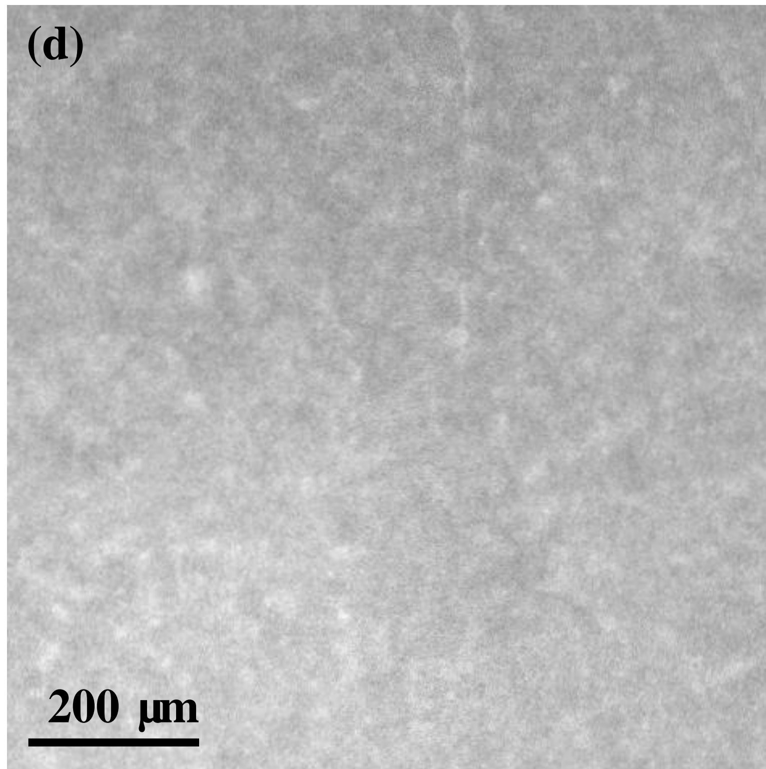

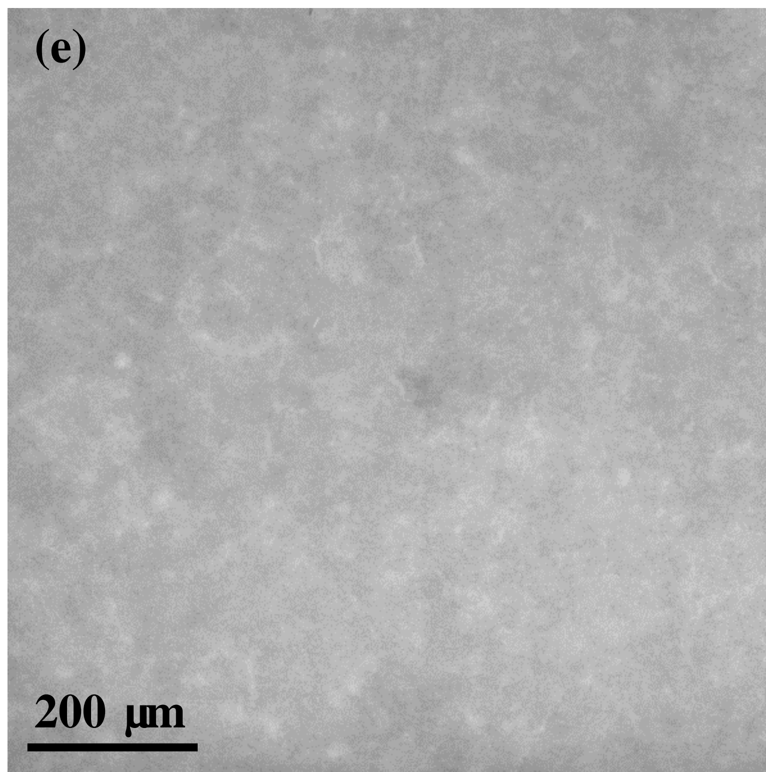

Fig. 5.4. X-ray transmission images of sintered sample under different external applied drying pressures of (a) 0 MPa, (b) 1 MPa, (c) 3 MPa, (d) 5 MPa, and (e) 10 MPa.

SEM images of cross sections of samples that were fabricated under drying pressures of 0 MPa, 3 MPa, and 10 MPa were taken to determine the relationship between drying pressure and the resulting microstructure of the sintered silver joints. Fig. 5.5 (a) - (c) show the representative microstructures of sintered silver joints fabricated under drying pressures of 0 MPa, 3 MPa, and 10 MPa, respectively. The difference in relative density between the joints fabricated at drying pressures of 0 and 3 MPa is very obvious, while that between the joints fabricated at drying pressures of 3 MPa and 10 MPa is more subtle. The application of pressure as early as in the drying stage has a profound effect on the sintered microstructure, which in turn affects the bonding strength, as demonstrated in Fig. 5.3.

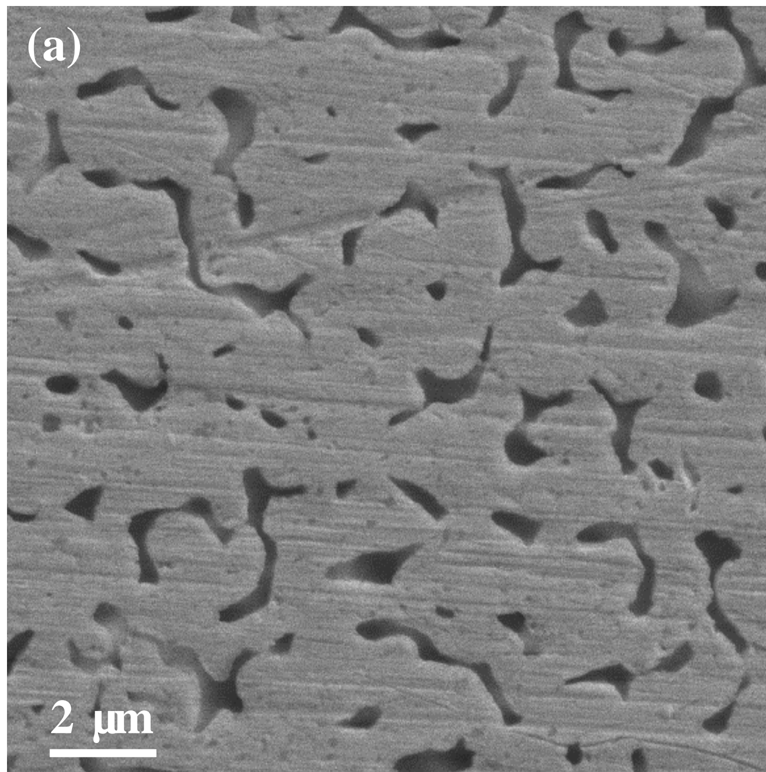

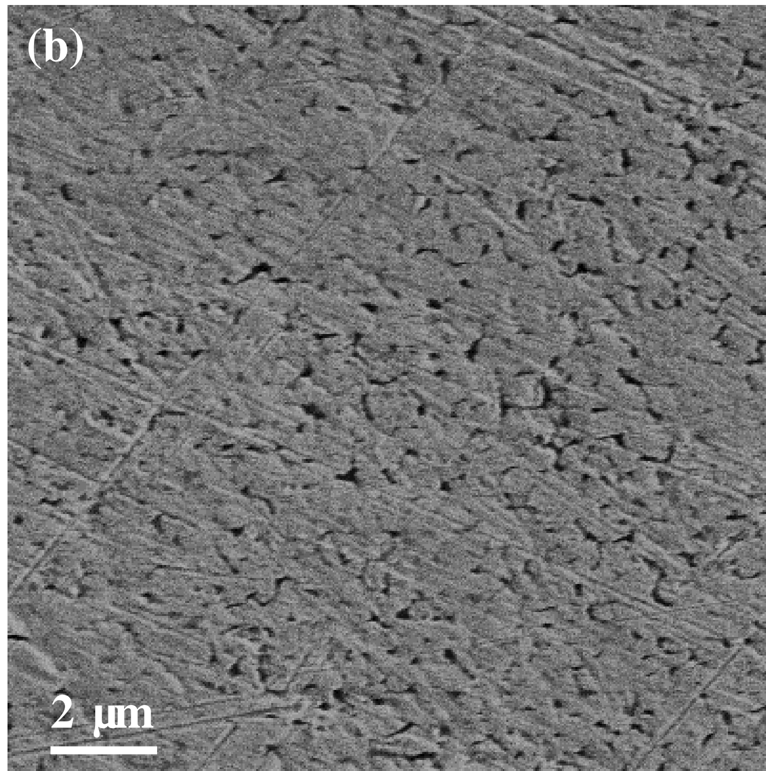

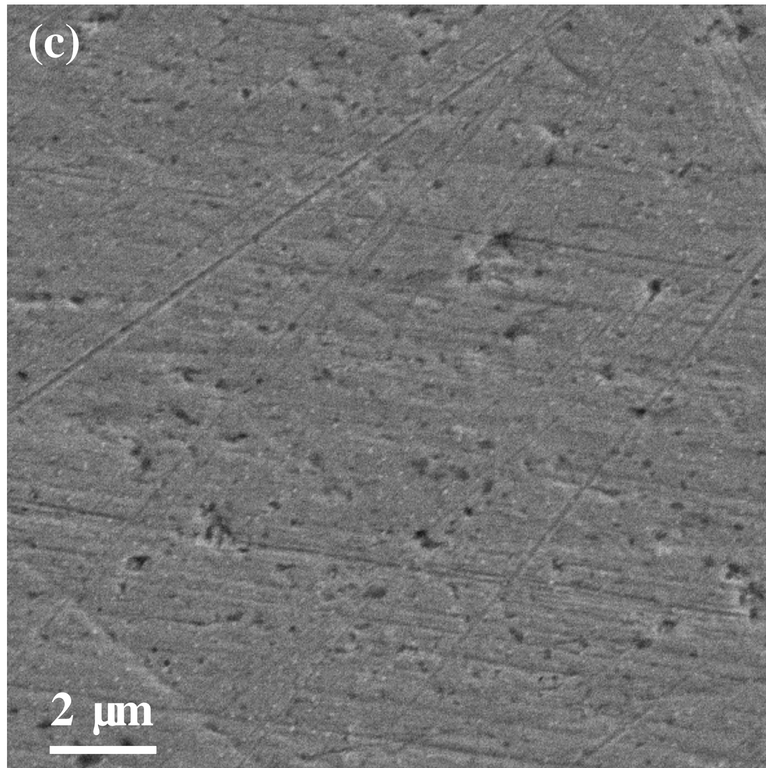

Fig. 5.5. SEM images of corss-sectioned sintered silver joints fabricated with (a) zero drying pressure, (b) 3 MPa drying pressure, and (c) 10 MPa drying pressure.

The relative density of a sintered joint was estimated from the microstructure. About 15 SEM images for each sample were taken on the cross-sectional area of the sintered silver joint. Each SEM image was subjected to image analysis, and the calculated porosities from all the images were averaged to obtain the porosity of the joint.

As shown in Fig. 5.6, the relative densities of sintered silver joints fabricated under 0 MPa, 3 MPa and 10 MPa are calculated to be 85.5±1.5%, 95.3±2.7% and 98.7±0.5%, respectively. Since all the samples were fabricated without pressure during the sintering stage at 275 ℃, it is evident that pressure during the sintering stage is not necessary for high sintered joint density. While it is difficult to obtain a microstructure image before the paste undergoes sintering because the particles have not formed a strongly bonded network, we can infer from the sintered microstructure that the application of pressure during drying has a strong effect on the sintered joint.

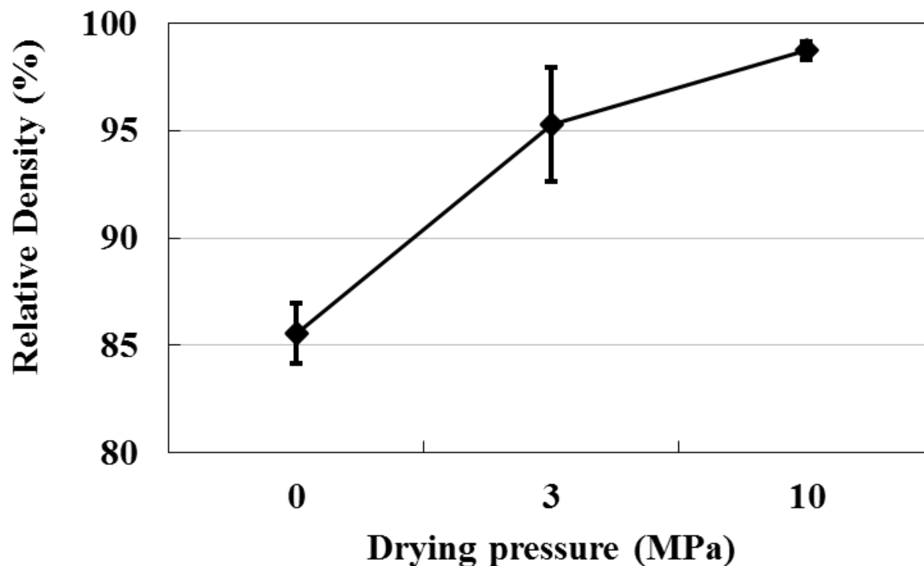

Fig. 5.6. Relative density of sintered nanosilver joint vs. drying pressure.

Even with a high weight loading, the paste, which consists of silver particles and flakes, has a relatively low volume loading. Thus, if the particles retain their position in space as

a result of the constraint imposed by the substrate and chip, a very porous dried layer is obtained with a far lower number of particle to particle contacts than would be possible with a printed layer that is unconstrained or has one of the surfaces open. During sintering, the interparticle contacts undergo necking that grows over time, drawing silver atoms from the interior of the particles through a combination of grain boundary and volume diffusion. This phenomenon causes the particle centers to move closer together while reducing interparticle voids, resulting in densification. With a lower coordination among particles, a porous microstructure will result. Applying pressure during sintering forces the particles into higher coordination, thus resulting in higher density and an increase in bond strength [88-91].

The same effect may be achieved when pressure is applied during drying while the paste is still wet. In this case, the green density before sintering will already be higher than that of the paste dried without pressure. Because of the lubricating effect of the wet organics, the rearrangement of the particles into a denser packing may be easier to achieve than when the paste has become rigid with the loss of solvents, which keep the binder soft, as in the case when pressure is applied only during sintering. Thus, it would appear that the die-shear strength is more responsive to the application of pressure during drying than during sintering. Furthermore, applying pressure during drying should produce an even denser microstructure and higher strength, as has already been demonstrated here and by others [32].

An added advantage of subjecting the joint under pressure while sample drying is that it will prevent drying-induced cracking as the solvent is leaving and the paste is undergoing shrinkage. A detailed internal stress analysis was shown in the simulation.

5.3.3. Simulation of internal stress evolution

The internal x-y in-plane stress of nanosilver joint layer under different external applied pressures (from 0 to 10 MPa) during drying are shown in Fig. 5.7. Each individual figure presents a stress distribution of the paste in the upper right quarter of chip attachment with the given pressure and time shown below. The internal vertical stress of nanosilver joint layer under different external applied pressures (from 0 to 10 MPa) during drying are shown in Fig. 5.8.

The analysis of internal stresses of paste indicates that both in-plane internal stress and vertical internal stress of nanosilver paste in the chip attachment decrease with increasing the external applied pressure during drying. As shown in Fig. 5.7 and Fig. 5.8, with external applied pressure during 180 ℃ drying, the in-plane internal stress and vertical internal stress are both reduced comparing to the same heating state with zero external pressure. At any given location, lower internal stress means the lower possibility to generate defects in the paste (such as cracking and debonding), thus lead to a higher bonding quality.

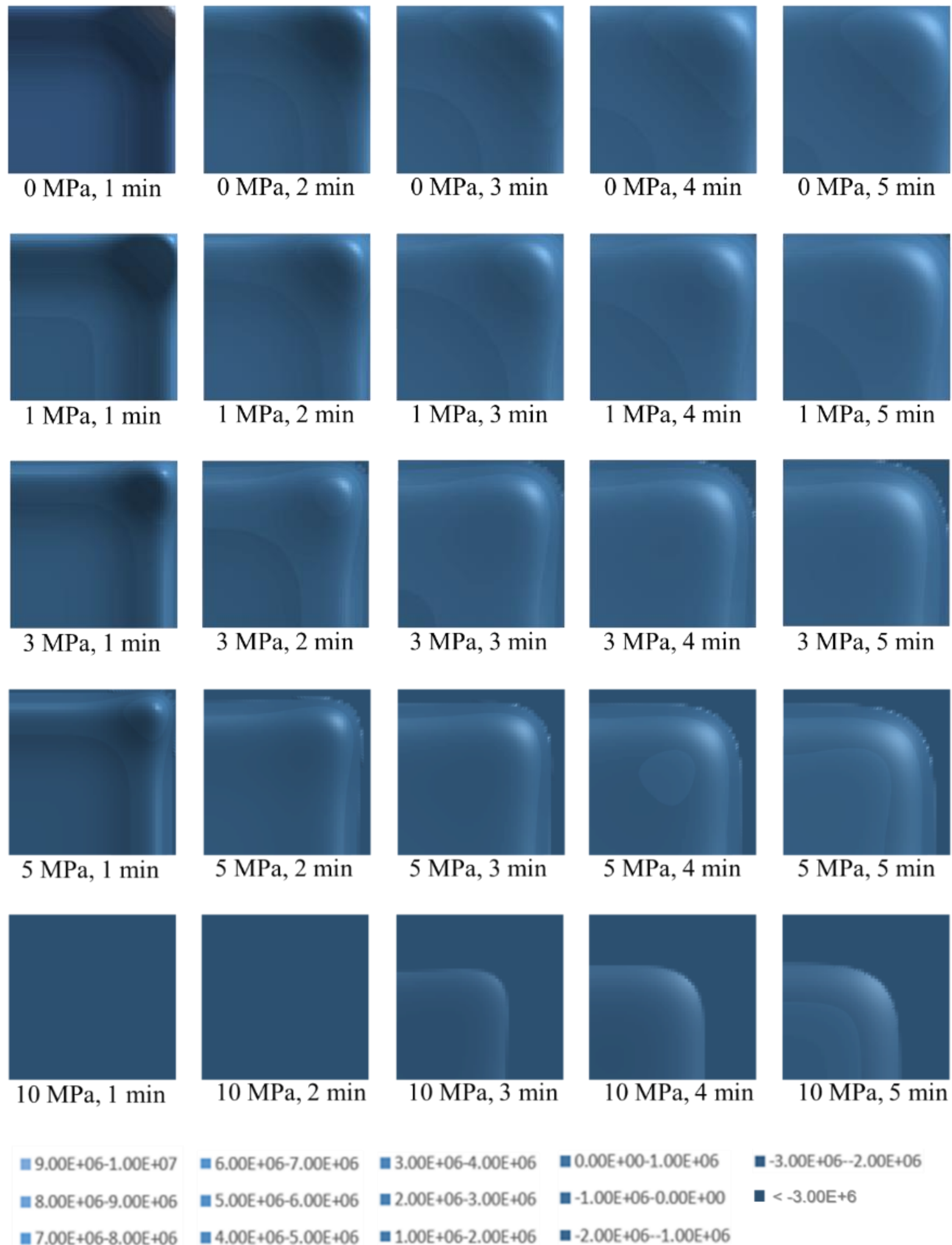

Fig. 5.7. Distribution of x-y in-plane internal stress of nanosilver paste between 10 × 10 mm^2 chip and substrate at 180 ℃ drying under 0 to 10 MPa external pressure for 1 to 5 minutes. For reason of symmetry, only a quarter of the paste is considered in the simulation. In each figure, the left bottom corner is the center of the chip and the right top corner is the corner of the chip.

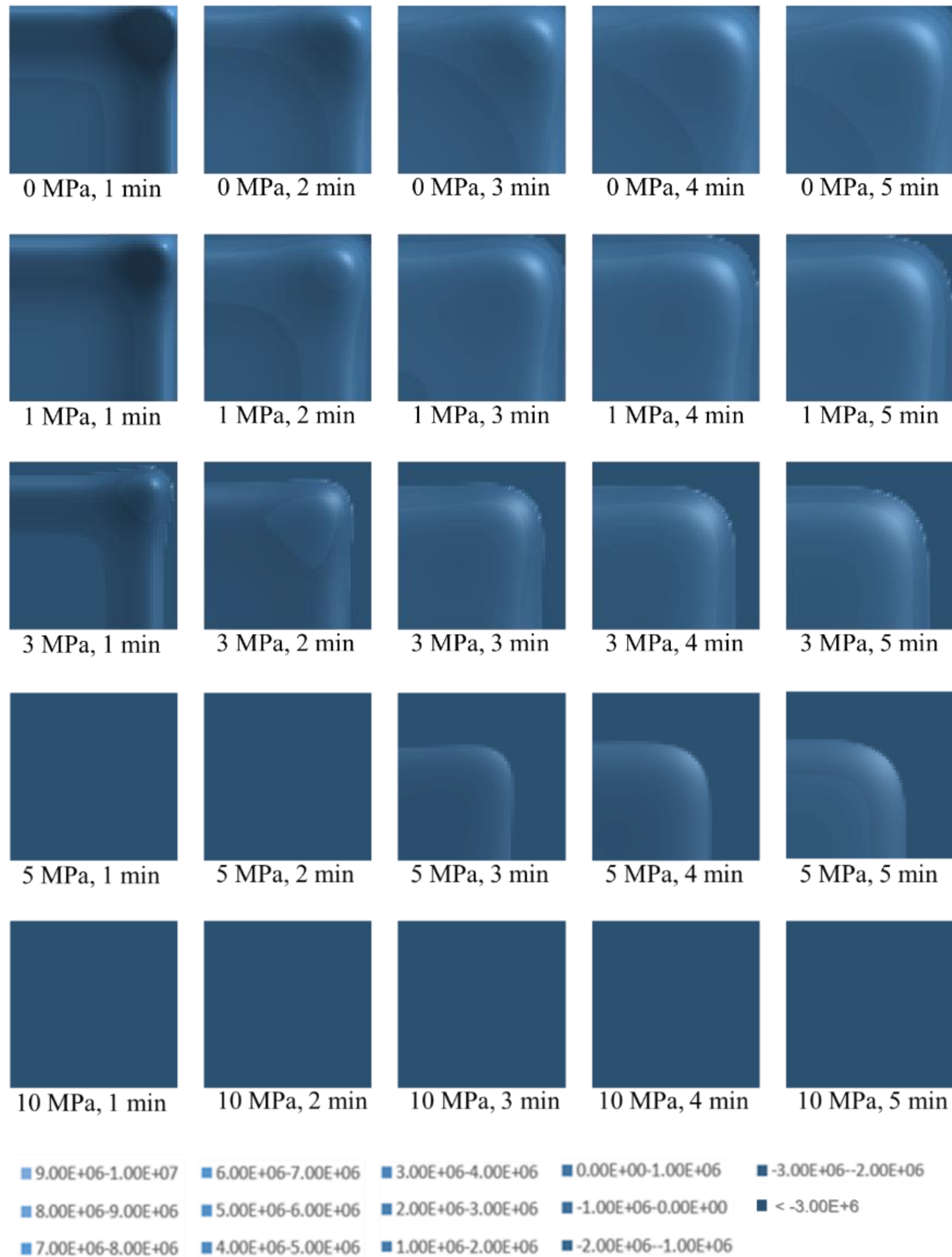

Fig. 5.8. Distribution of vertical internal stress of nanosilver paste between 10×10 mm^2 chip and substrate at 180 ℃ drying under 0 to 10 MPa external pressure for 1 to 5 minutes. For reason of symmetry, only a quarter of the paste is considered in the simulation. In each figure, the left bottom corner is the center of the chip and the right top corner is the corner of the chip.

To present the quantitative results, Table 5.2 and Table 5.3 are listed to show the simulated results of the minimum and maximum internal stresses of the paste in the chip attachment during 180 ℃ drying for 1 to 5 minutes. Because only the internal stresses those are higher than zero may cause cracking or delamination in the paste, the stresses above zero are highlighted in the tables, as a warning of the possible formation of defects in the sintered silver bond-line. The simulation results indicate that:

(1). In the chip attachments with low external applied pressures (0, 1 and 3 MPa), the x-y in-plane internal stress in some part of paste region can be greater than zero, which may cause cracking problem in the silver joint layers;

(2). In the chip attachments with low external applied pressures (0 and 1 MPa), the vertical internal stress in some part of paste can exceed zero, which may cause partial delamination problem and reduce the die-shear strength of chip attachment;

(3). In the chip attachments with high external applied pressures (3 MPa above), both the x-y in-plane and vertical internal stresses are less than zero, which means there are no tensile stresses to cause cracking or delamination problems.

The analysis were in agreement with the experimental results as shown in Fig. 5.4.

Table 5.2: Minimum and maximum x-y in-plane internal stress (in MPa) of the paste in the chip attachment during drying under different external applied pressures.

Drying time / Applied pressure	1 minute		2 minute		3 minute		3 minute		5 minute	
	Min	Max	Min	Max	Min	Max	Min	Max	Min	Max
0 MPa	-0.6	7.3	-0.5	3.9	-0.4	2.7	-0.5	2.1	-1.0	1.7
1 MPa	-1.0	5.2	-0.1	2.4	-2.8	1.5	-3.5	1.1	-3.9	0.8

3 MPa	-2.0	2.0	-7.5	0.3	-9.2	-0.1	-9.7	-0.2	-9.7	-0.2
5 MPa	-8.0	-0.1	-14.0	-1.0	-15.7	-1.0	-15.9	-0.9	-15.5	-0.8
10 MPa	-23.1	-3.6	-30.5	-3.1	-31.8	-2.6	-31.2	-2.1	-29.9	-1.8

Table 5.3: Minimum and maximum vertical internal stress (in MPa) of the paste in the chip attachment during drying under different external applied pressures.

Drying time / Applied pressure	1 minute		2 minute		3 minute		3 minute		5 minute	
	Min	Max	Min	Max	Min	Max	Min	Max	Min	Max
0 MPa	-1.2	4.7	-1.7	2.1	-3.5	1.3	-4.3	0.9	-4.5	0.7
1 MPa	-1.9	2.1	-7.3	0.3	-9.0	-0.0	-9.5	-0.1	-9.4	-0.1
3 MPa	-12.1	-1.2	-18.5	-1.7	-20.0	-1.5	-19.9	-1.3	-19.3	-1.1
5 MPa	-22.4	-3.5	-29.7	-3.1	-31.0	-2.5	-30.4	-2.1	-29.1	-1.7
10 MPa	-48.0	-7.5	-57.8	-5.7	-58.5	-4.6	-56.5	-3.7	-53.7	-3.2

5.4. Summary

In this chapter, large-area chip attachments with the chip size of 10×10 mm^2 were fabricated by nanosilver LTJT with different external applied drying pressure from 0 to 10 MPa and pressureless sintering. The die-shear strength of chip attachments and the microstructures of sintered silver bond-line were evaluated. Numerical simulation were also applied to study the evolution of internal stress of nanosilver paste in the chip attachment during the drying process. Several conclusions can be drawn:

Microstructures of sintered silver bond-line show that defects of voids and cracks can be observed when the samples are fabricated with external applied pressure below 3 MPa during drying. The portion of defects decreases with increasing the external applied pressure, resulting in high die-shear strength.

Numerical simulation of the internal stress evolution of nanosilver paste in the chip attachment during drying under different external applied pressures shows that both x-y in-plane stress and vertical stress of the nanosilver paste decrease with increasing external applied drying pressure. Furthermore, when the applied drying pressure is above 3 MPa, the vertical internal stress will be always below zero during drying, which means no delamination will occur; when the applied drying pressure is above 5 MPa, the x-y in-plane stress will be always below zero and will not induce cracks in the nanosilver bond-line. The simulated results are in good agreement with the experimental data.

Chapter 6. Effects of temperature ramp rate and drying time on sintered silver bond-line

6.1. Introduction

Other than pressure, the time and temperature during drying stage are significant factors to the final quality of sintered silver bond-line. Practically, the application of pressure requires hot press, which is not standard soldering equipment for chip. Therefore, the study of the time and temperature effects during drying stage on the quality of sintered silver bond-line is not only a fundamental research but also a practical approach to improve the nanosilver LTJT process based on soldering equipment (such as belt furnace). For nanosilver LTJT drying process, the highest drying temperature is set to 180°C to ensure solvent thoroughly moving out. Therefore, the combination factors of time and temperature - temperature ramp rate and low temperature drying time - was studied in this chapter. A series of experiments was carried out to evaluate the effect of temperature ramp rate and time of drying on the bonding strength of the sintered nanosilver chip attachment, and the experimental results were analyzed and compared with the simulated results.

6.2. Experimental procedures

6.2.1. Sample preparation

Alumina mechanical chips, direct-bond-copper (DBC) substrates and the nanosilver paste were used for fabricating the chip attachments. The nanosilver paste (nanoTach type K) was supplied by NBE Technologies, LLC, Blacksburg, Virginia. The copper layer on the DBC substrate was 200 μm, and the sandwiched alumina thickness was 380 μm. The

thickness of the mechanical chips was 1000 μm, which was preferred for ease of die shearing. The surfaces of the DBC copper and the mechanical chips were metalized with silver of a few hundred nanometers thick. There were two different lateral dimensions of the mechanical chips: 3×3 mm^2 and 6×6 mm^2. The mechanical chips were mounted on 10×15 mm^2 of DBC substrates.

To attach chips to substrates by LTJT silver sintering, the process was described as follows: first, the nanosilver paste was dispensed on the substrate; second, the chip was mounted on the paste and the wet thickness of nanosilver paste for die-attach was controlled to be 37 μm with the help of a thickness controller; and last, the attachment was heated in air following the heating profiles. The schematic and the setup of the thickness controller are shown in Fig. 6.1. As the distance between the press tip and the flat base plate was set precisely by tuning the micrometer, the nanosilver bond-line can be controlled at any desired wet thickness.

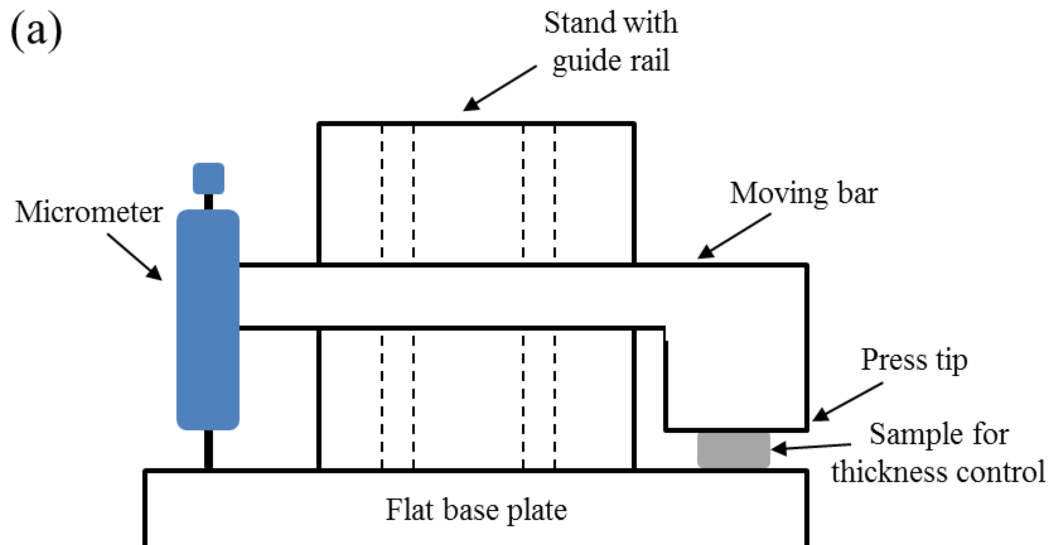

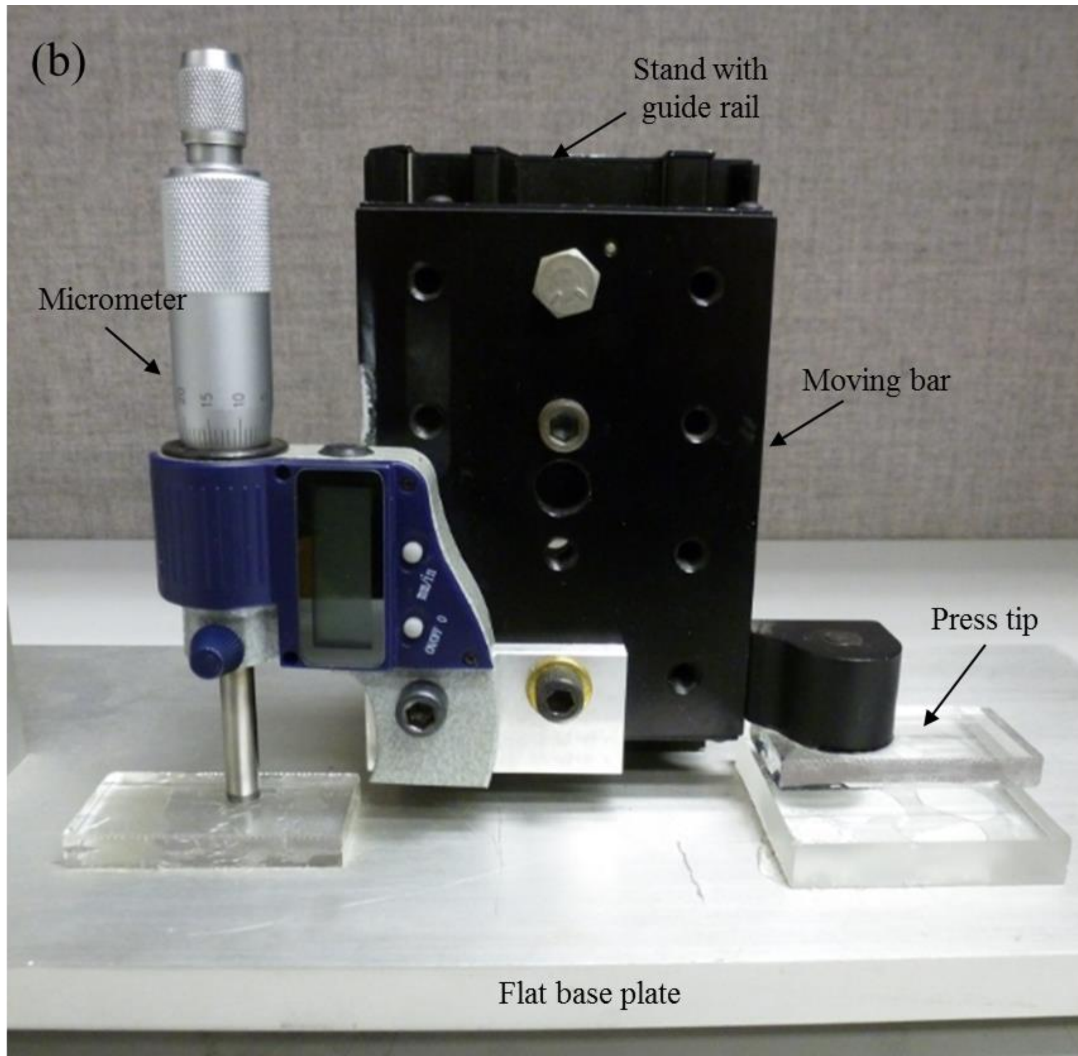

Fig. 6.1. (a) Schematic of thickness control for initial nanosilver paste bond-line and (b) the custom built thickness controller setup.

The schematic of heating profile is shown in Fig. 6.2. It consists of the drying stage and the sintering stage. In this study, the sintering stage was kept constant with the temperature of 260°C and the time of 10 minutes. The drying stage can be further divided into three different sub stages: pre-drying stage, temperature ramp stage, and holding stage. Pre-drying stage is the time period for the chip attachment soaking at room temperature (24°C); temperature ramp stage is for heating the chip attachment from room temperature to 180°C, of which different ramp rates may apply; holding stage is for the

chip attachment drying at a relatively high temperature (180°C) to ensure the sufficient solvent removal. In order to evaluate the effect of drying rate on the quality of sintered silver joint, drying profiles with different temperature ramp rates were used to fabricate the nanosilver chip attachments. For the fair comparison, the total time duration of the temperature ramp stage and holding stage in each case was kept constant as 156 minutes. Additionally, the "overnight" effect, which pre-dries the chip attachment in room temperature before heating, was also evaluated in the study. Table 6.1 shows the different drying process parameter combinations. For each combination, three replicates were fabricated.

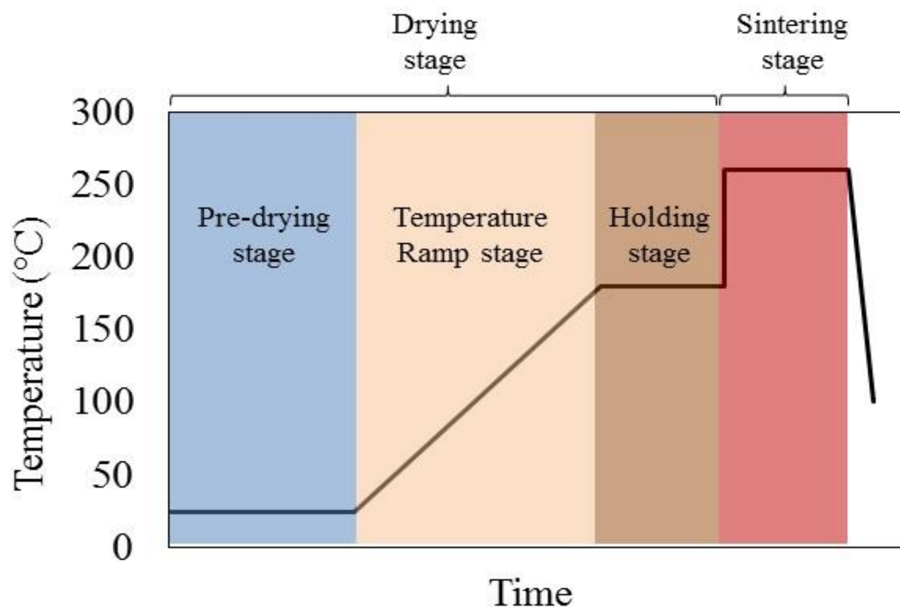

Fig. 6.2. Schematic of heating profile for nanosilver chip attachment fabrication

Table 6.1: Parameter combinations of different pre-drying time, temperature ramp rate and holding time in drying stage.

Group No.	Chip size (mm^2)	Pre-dying time (min)	Temperature ramp rate (°C/min)	Holding time (min)
A	3 × 3	0	1	0

B	3 × 3	0	3	104
C	3 × 3	0	7.5	135
D	3 × 3	1440	3	104
E	6 × 6	0	1	0
F	6 × 6	0	3	104
G	6 × 6	0	7.5	135
H	6 × 6	1440	3	104

6.2.2. Die-shear testing

The bonding quality of nanosilver sintered chip attachments was estimated by the die-shear test. The test was conducted by the equipment of Nordson DAGE 4000 Multipurpose Bondtester at the shearing speed of 300 μm/s. The test equipment is shown in Fig. 6.3.

Fig. 6.3. Nordson DAGE 4000 Multipurpose Bondtester.

6.2.3. Numerical simulation of the stress and strain evolution

Numerical simulation of the internal stress and strain evolution of nanosilver paste was applied according to the different process profiles during drying. In order to simulate the experimental process conditions, three sequential heating segments were used for pre-drying stage, temperature ramp stage and holding stage. In this study, no external pressure was applied during the entire drying process.

The input parameters nanosilver paste drying are shown in Table 6.2.

Table 6.2: Input parameters of nanosilver chip attachment during drying.

		Case A	Case B	Case C	Case D	Case E	Case F	Case G	Case H
Meshing of grids (quarter chip)		15×15	15×15	15×15	15×15	30×30	30×30	30×30	30×30
Chip dimension (mm^2)		3 ×3	3 ×3	3 ×3	3 ×3	6 ×6	6 ×6	6 ×6	6 ×6
Initial solvent concentration		0.17	0.17	0.17	0.17	0.17	0.17	0.17	0.17
Heating segment		3	3	3	3	3	3	3	3
Segment 1	Initial temperature (K)	297	297	297	297	297	297	297	297
	Temperature ramp rate (K/s)	0	0	0	0	0	0	0	0
	Time duration (s)	0	0	0	86400	0	0	0	86400
Segment 2	Initial temperature (K)	297	297	297	297	297	297	297	297
	Temperature ramp rate (K/s)	0.017	0.05	0.125	0.05	0.017	0.05	0.125	0.05

	Time duration (s)	9360	3120	1248	3120	9360	3120	1248	3120
Segment 3	Initial temperature (K)	453	453	453	453	453	453	453	453
	Temperature ramp rate (K/s)	0	0	0	0	0	0	0	0
	Time duration (s)	0	6240	8112	6240	0	6240	8112	6240

6.3. Results and discussion

6.3.1. Die-shear strength of chip attachments

The die-shear strength of chip attachments are shown in Table 6.3. The effects of temperature ramp rate and overnight pre-drying on the die-shear strength of sintered nanosilver chip attachment are shown in Fig. 6.4. Furthermore, the effect of chip size on the die-shear strength is also discussed.

Table 6.3: Die-shear strength of nanosilver chip attachments fabricated with different heating parameter combinations.

Group No.	Chip size (mm^2)	Pre-dying time (min)	Temperature ramp rate (°C/min)	Holding time (min)	Die-shear strength		
A	3 ×3	0	1	0	41.9*	40.6	37.1
B	3 ×3	0	3	104	27.0	24.3	30.1
C	3 ×3	0	7.5	135	12.5	19.1	11.2
D	3 ×3	1440	3	104	30.9	32.7	38.0
E	6 ×6	0	1	0	30.2	23.7	29.1
F	6 ×6	0	3	104	12.1	11.4	7.8
G	6 ×6	0	7.5	135	5.4	3.7	3.3
H	6 ×6	1440	3	104	17.0	26.1*	22.9

"*" represents that the mechanical chip cracked during test.

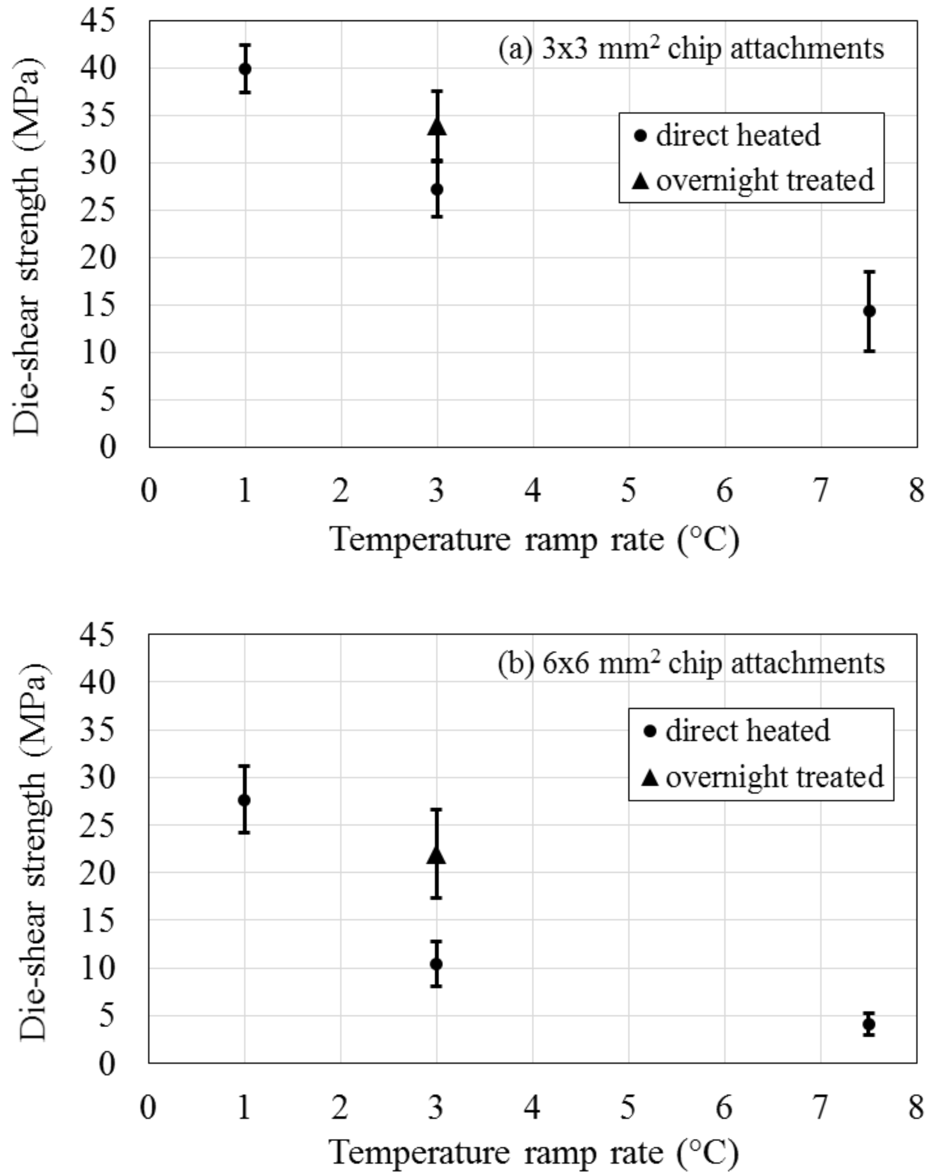

Fig. 6.4. Die-shear strength vs. temperature ramp rate for (a) 3×3 mm^2 and (b) 6×6 mm^2 chip attachments.

The effect of temperature ramp rate during drying on the final die-shear strength of sintered nanosilver chip attachment is obvious. For both cases of 3×3 mm^2 and 6×6 mm^2 chip attachments, die-shear strength decreases with increasing the temperature ramp rate. The results indicates that the slow temperature ramp rate of drying process can enhance the mechanical strength of sintered silver joint. The possible reason can be

explained as follows: if some part of the paste is completely dried, the viscosity of this part will be extremely high and that part can hardly be compressed. Usually the edges of paste are firstly dried, and these dried edges will provide as solid frames to prevent the further shrinkage of paste even when the center parts get dried. A slow temperature ramp rate can keep the nanosilver paste at a relatively low temperature for longer time, which provides more time for solvent escaping from the center part of paste and for paste shrinking before the edges getting. The high temperature ramp rate, in the contrast, will fast dry the edges of nanosilver paste under the chip and prevent further shrinkage of the paste. Higher shrinkage of nanosilver paste in the drying condition implies higher green density before silver sintering, and can lead to higher sintered silver density, which performs higher bonding strength.

The same explanation can also be applied to the "overnight" drying effects, which refers to the 24 hours pre-drying of chip attachments at room temperature before heating up. As pre-drying stage offers an initial drying at a low temperature for a longer time, more solvent in the center part of the paste can escape before the paste in the edge parts becoming harder. Therefore, the layers of nanosilver paste with the overnight treatment can achieve a higher shrinkage than the ones that without overnight treatment, and the higher shrinkage leads to higher green density of the nanosilver paste and higher sintered density of nanosilver joint. The pre-drying stage plays an important role in furthering paste shrinkage before sintering and helps to obtain the high bonding strength of sintered silver joints.

The size of chips also has an effect on the bonding strength of sintered nanosilver chip attachments. Applying the same heating profile on chip attachments with different chip

sizes, we can obtain different die-shear strength on the sintered nanosilver joint. By comparing samples in group A with samples in group E, samples in group B with samples in group F, samples in group C with samples in group G, and samples in group D with samples in group H, it is found that the die-shear strength of samples in groups with 3×3 mm^2 chip size are always higher than the samples in groups with 6×6 mm^2 chip size with the same heating profile. This is because at any given temperature, the solvent in the chip attachment with smaller chip area is always easier to escape. It implies that for small area chip attachments, when the edges of nanosilver paste are dried and becoming hard, most solvent in the paste has gone, and shrinkage of paste has already completed. In the contrast, for large area chip attachments, a larger amount of solvent will remain in the center part of the nanosilver paste when the edges of the paste are dried and becoming hard, and the paste can hardly shrink any more even the rest solvent is still leaving. Low shrinkage leads to low green density of the nanosilver paste and also low sintered density of nanosilver joint, which presents low die-shear strength.

6.3.2. Simulation of internal stress and shrinkage of nanosilver paste

The evolution of maximum internal stresses of the nanosilver paste in 3×3 mm^2 chip attachments with different heating process (from case A to D) are shown in Fig. 6.5, Fig. 6.6, Fig. 6.7, and Fig. 6.8. The distributions of x-y in-plane stress and vertical stress at four typical stages (stress initiation, stress increase, stress maximum, and stress relaxation) are also shown in the figures.

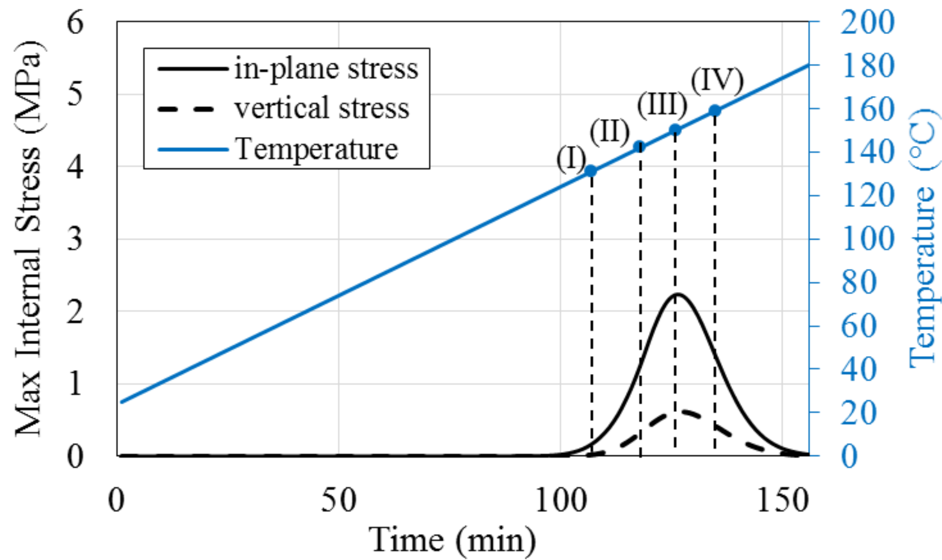

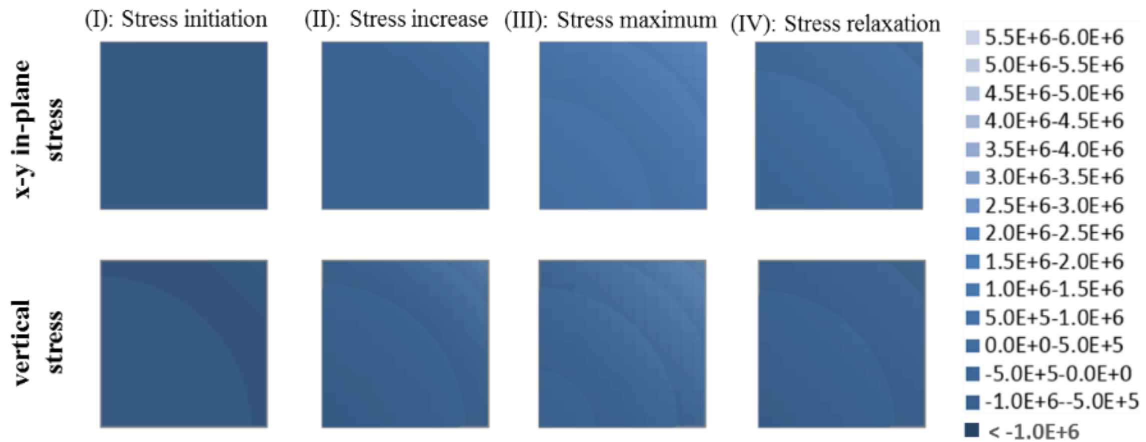

Fig. 6.5. The top plot is the maximum x-y in-plane internal stress and maximum vertical internal stress of nanosilver paste in a 3 × 3 mm^2 chip attachment during heating profile A (heat from room temperature to 180°C with temperature ramp rate 1°C/min). The bottom figures show the distribution of internal stresses of nanosilver paste at the time points of (I), (II), (III), and (IV). For reason of symmetry, only a quarter of the paste is considered in the simulation. In each figure, the left bottom corner is the center of the chip and the right top corner is the corner of the chip.

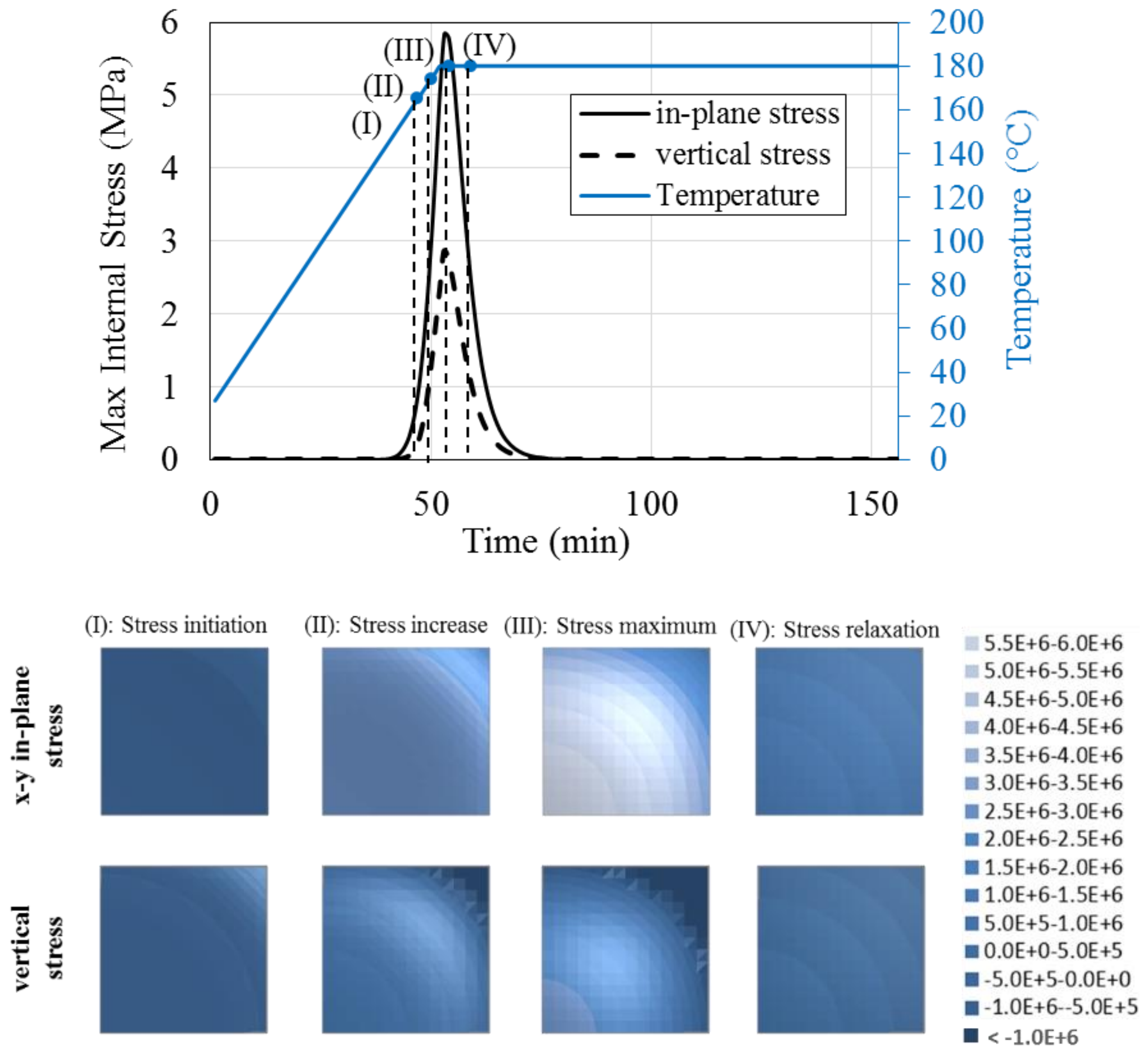

Fig. 6.6. The top plot is the maximum x-y in-plane internal stress and maximum vertical internal stress of nanosilver paste in a 3×3 mm^2 chip attachment during heating profile B (heat from room temperature to 180°C with temperature ramp rate of 3°C/min, and hold at 180°C for 104 minutes). The bottom figures show the distribution of internal stresses of nanosilver paste at the time points of (I), (II), (III), and (IV). For reason of symmetry, only a quarter of the paste is considered in the simulation. In each figure, the left bottom corner is the center of the chip and the right top corner is the corner of the chip.

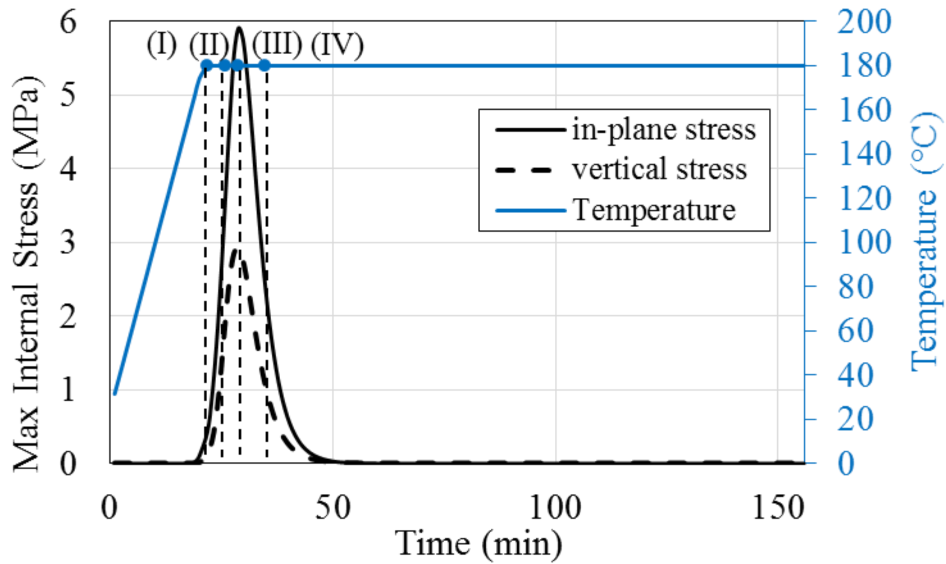

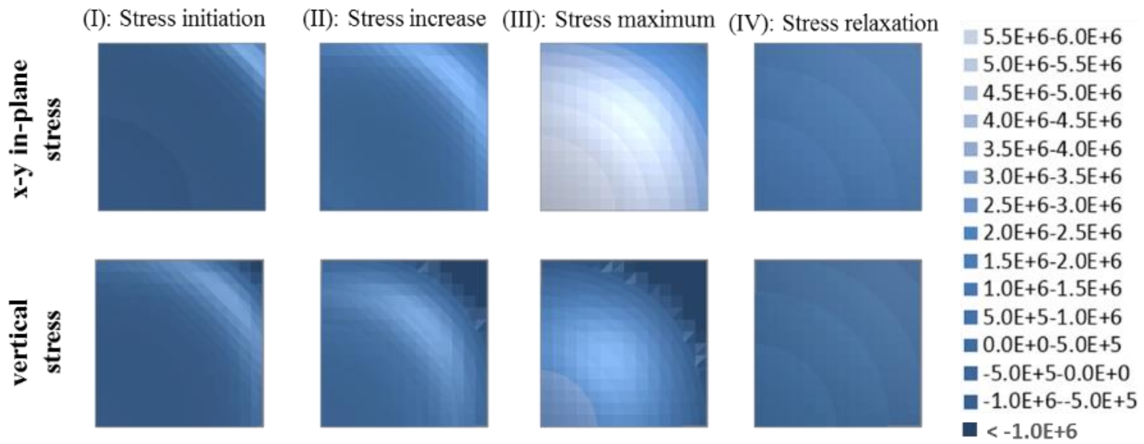

Fig. 6.7. The top plot is the maximum x-y in-plane internal stress and maximum vertical internal stress of nanosilver paste in a 3 × 3 mm^2 chip attachment during heating profile C (heat from room temperature to 180°C with temperature ramp rate of 7.5°C/min, and hold at 180°C for 135 minutes). The bottom figures show the distribution of internal stresses of nanosilver paste at the time points of (I), (II), (III), and (IV). For reason of symmetry, only a quarter of the paste is considered in the simulation. In each figure, the left bottom corner is the center of the chip and the right top corner is the corner of the chip.

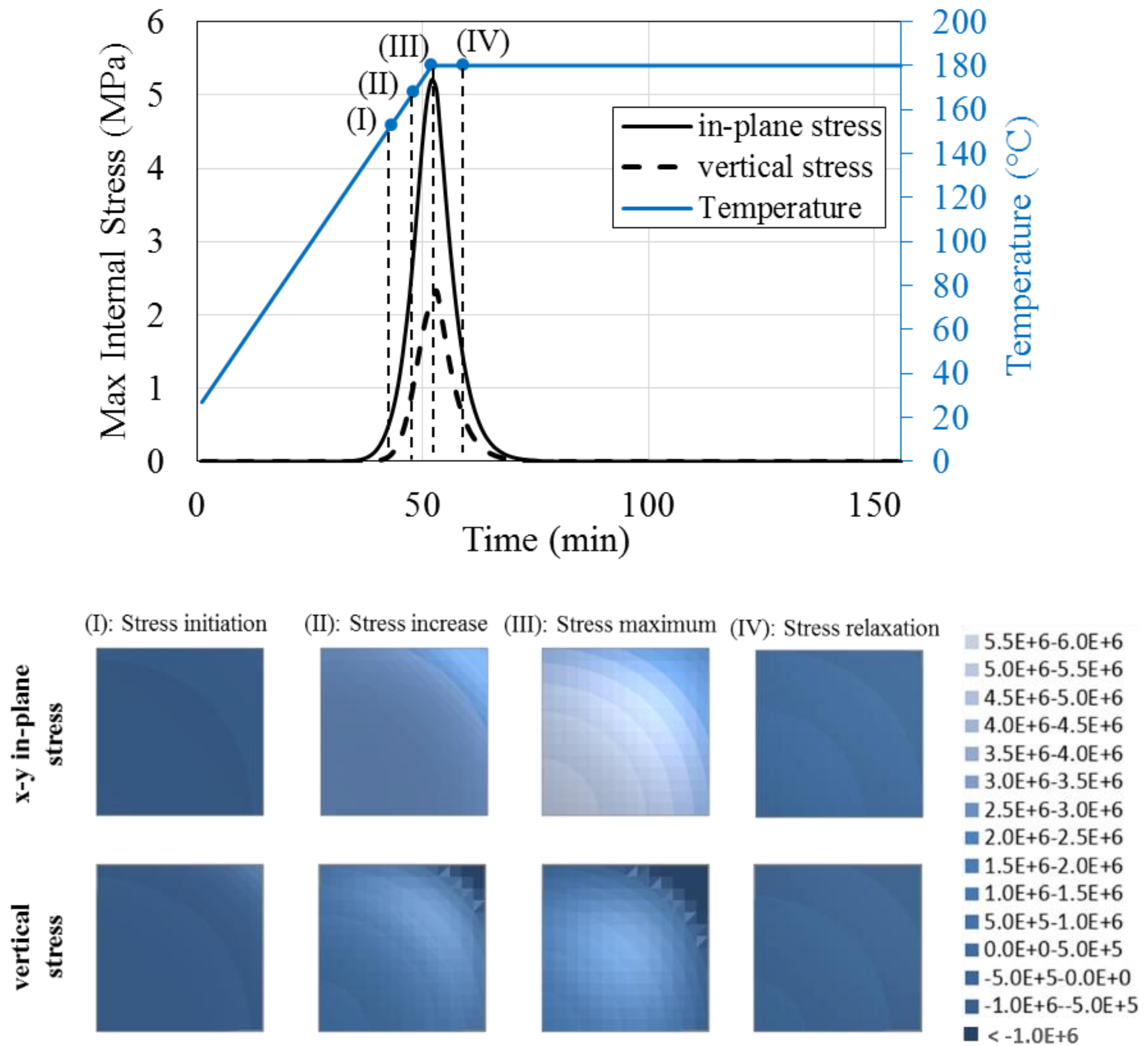

Fig. 6.8. The top plot is the maximum x-y in-plane internal stress and maximum vertical internal stress of nanosilver paste in a 3 $\times$3 mm^2 chip attachment during heating profile D (after room temperature treatment for 24 hours, then heat from room temperature to 180°C with temperature ramp rate of 3°C/min, and hold at 180°C for 104 minutes). The bottom figures show the distribution of internal stresses of nanosilver paste at the time points of (I), (II), (III), and (IV). For reason of symmetry, only a quarter of the paste is considered in the simulation. In each figure, the left bottom corner is the center of the chip and the right top corner is the corner of the chip.

During the early stage of drying, the internal stresses are relatively low because of the low viscosity of the paste at that time. As the solvent moves out, the viscosity of paste become higher and the maximum internal stress increases. At the end of drying, as the solvent has almost gone, the paste stops shrinking and there is no more induced stress by the change of strain. Therefore, the internal stress will release to zero when the drying completes.

In the 3×3 mm^2 chip attachments, for 1°C/min temperature ramp rate, the maximum internal stresses are generated at the temperature around 150°C. The maximum x-y in-plane internal stress is 2.2 MPa and maximum vertical internal stress is 0.6 MPa. For 3°C/min temperature ramp rate, the maximum internal stresses are generated at 180°C temperature holding stage. The maximum x-y in-plane internal stress is 5.8 MPa and maximum vertical internal stress is 2.8 MPa. For 7.5°C/min temperature ramp rate, the maximum internal stresses are also generated at 180°C. The maximum x-y in-plane internal stress is 5.9 MPa and maximum vertical internal stress is 2.9 MPa. The slow temperature ramp rate helps to keep the solvent leave slow at relatively low temperatures, which induces low internal stresses. The maximum internal stresses in the condition of 3°C/min ramp rate and in the condition of 7.5°C/min ramp rate are almost the same, and the reason is that the maximum stresses for both cases are induced at the temperature holding stage with constant temperature of 180 ℃. The similar heating conditions lead to the similar evolution of the internal stress.

Fig. 6.8 shows the maximum internal stress after 24 hours room temperature treatment, which is referred to as "overnight treatment". After overnight treatment, a heating profile of 3°C/min to 180°C and 104 minutes holding time was applied. The maximum internal

stresses are generated at 180°C temperature holding stage. The maximum x-y in-plane internal stress is 5.2 MPa and maximum vertical internal stress is 2.2 MPa. The maximum internal stresses of the paste in the chip attachment after overnight treatment only slightly differ from those without overnight treatment. Because the internal stresses are related to the solvent change rate, high internal stress will generate at high temperature (with high solvent change rate). During the stage of overnight treatment at room temperature, the paste in the chip attachment can be partially dried before heating, without generate high internal stress. However, the simulated results indicates that overnight treatment has insignificant effect on the maximum internal stress during heating process, by comparing Fig. 6.8 with Fig. 6.6.

The evolution of maximum internal stress of the nanosilver paste in 6×6 mm^2 chip attachments with different heating profiles (from case E to H) are shown in Fig. 6.9, Fig. 6.10, Fig. 6.11, and Fig. 6.12. The distributions of the x-y in-plane stress and the vertical stress at four typical stages (stress initiation, stress increase, stress maximum, and stress relaxation) are also shown in the figures.

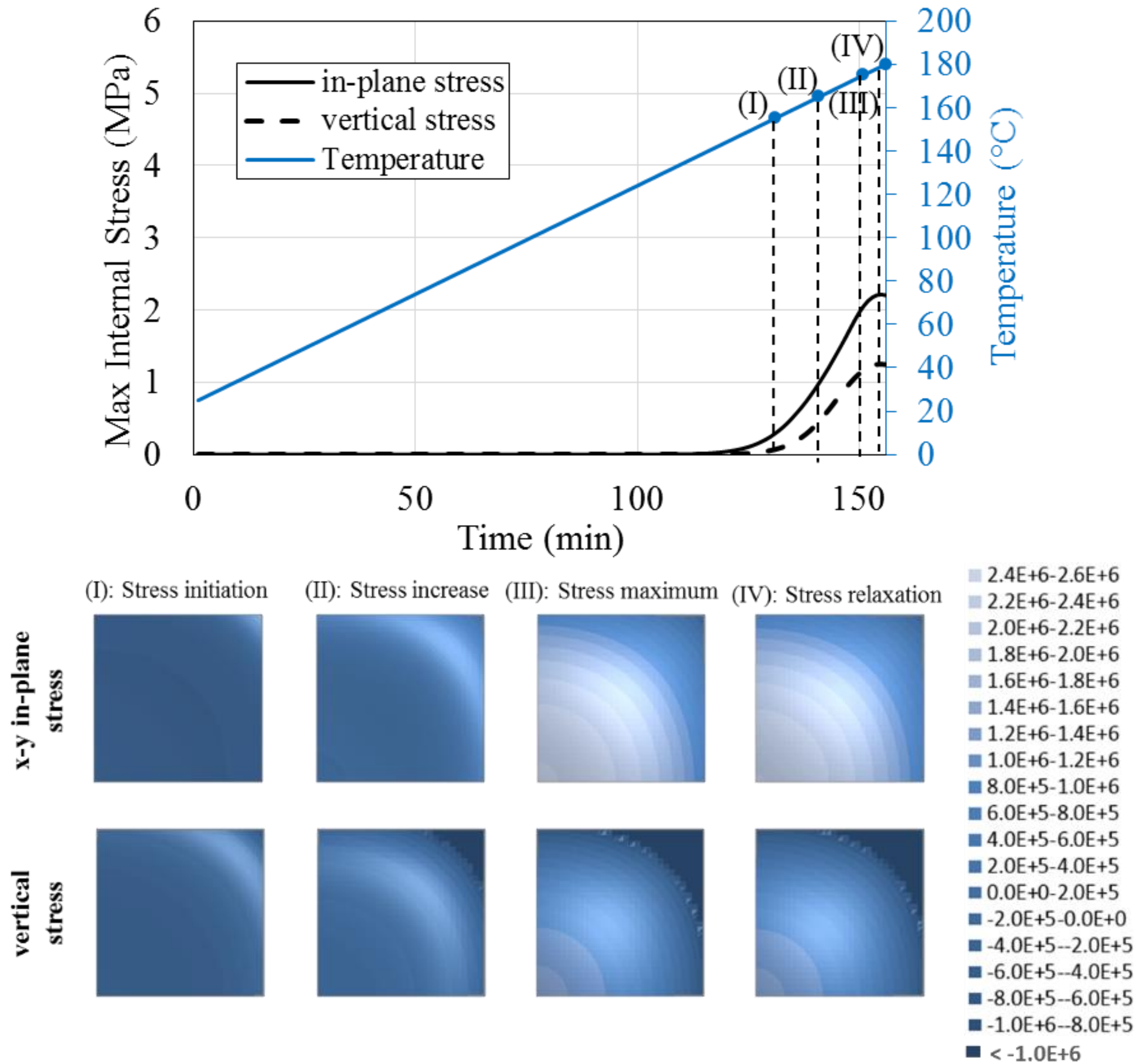

Fig. 6.9. The top plot is the maximum x-y in-plane internal stress and maximum vertical internal stress of nanosilver paste in a 6×6 mm^2 chip attachment during heating profile E (heat from room temperature to 180°C with temperature ramp rate 1°C/min). The bottom figures show the distribution of internal stresses of nanosilver paste at the time points of (I), (II), (III), and (IV). For reason of symmetry, only a quarter of the paste is considered in the simulation. In each figure, the left bottom corner is the center of the chip and the right top corner is the corner of the chip.

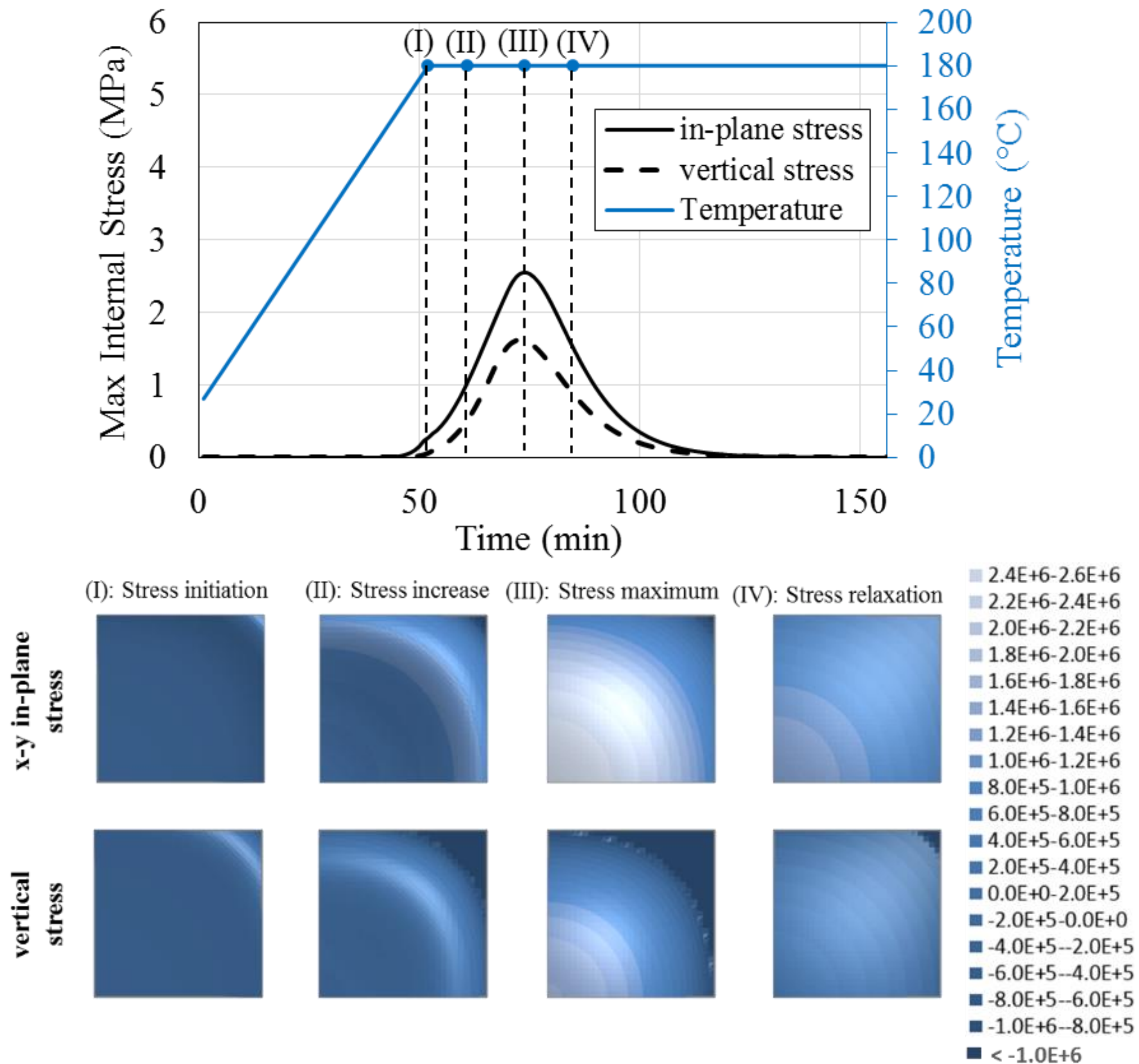

Fig. 6.10. The top plot is the maximum x-y in-plane internal stress and maximum vertical internal stress of nanosilver paste in a 6 $\times$6 mm^2 chip attachment during heating profile F (heat from room temperature to 180°C with temperature ramp rate of 3°C/min, and hold at 180°C for 104 minutes). The bottom figures show the distribution of internal stresses of nanosilver paste at the time points of (I), (II), (III), and (IV). For reason of symmetry, only a quarter of the paste is considered in the simulation. In each figure, the left bottom corner is the center of the chip and the right top corner is the corner of the chip.

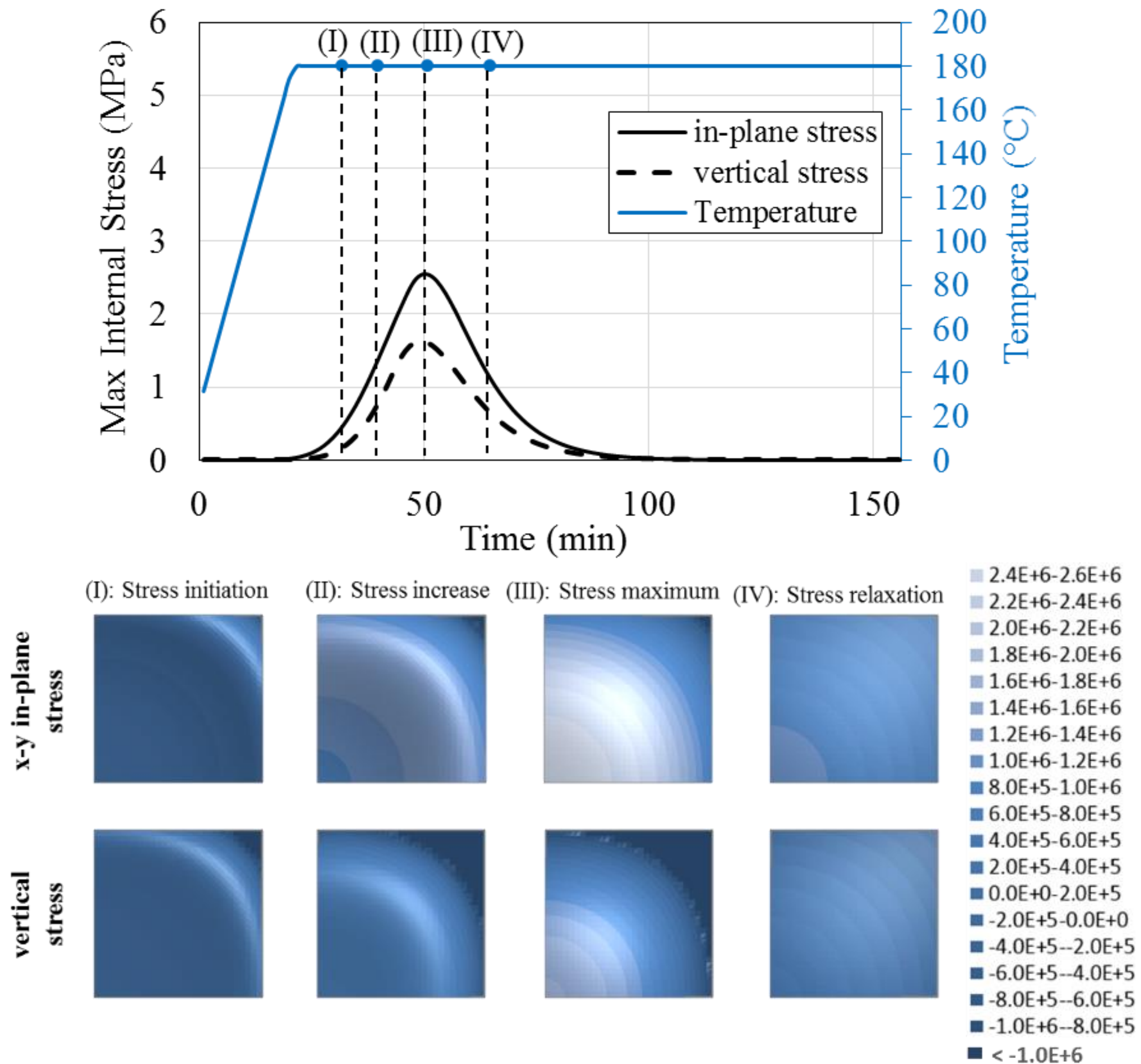

Fig. 6.11. The top plot is the maximum x-y in-plane internal stress and maximum vertical internal stress of nanosilver paste in a 6 × 6 mm^2 chip attachment during heating profile G (heat from room temperature to 180°C with temperature ramp rate of 7.5°C/min, and hold at 180°C for 135 minutes). The bottom figures show the distribution of internal stresses of nanosilver paste at the time points of (I), (II), (III), and (IV). For reason of symmetry, only a quarter of the paste is considered in the simulation. In each figure, the left bottom corner is the center of the chip and the right top corner is the corner of the chip.

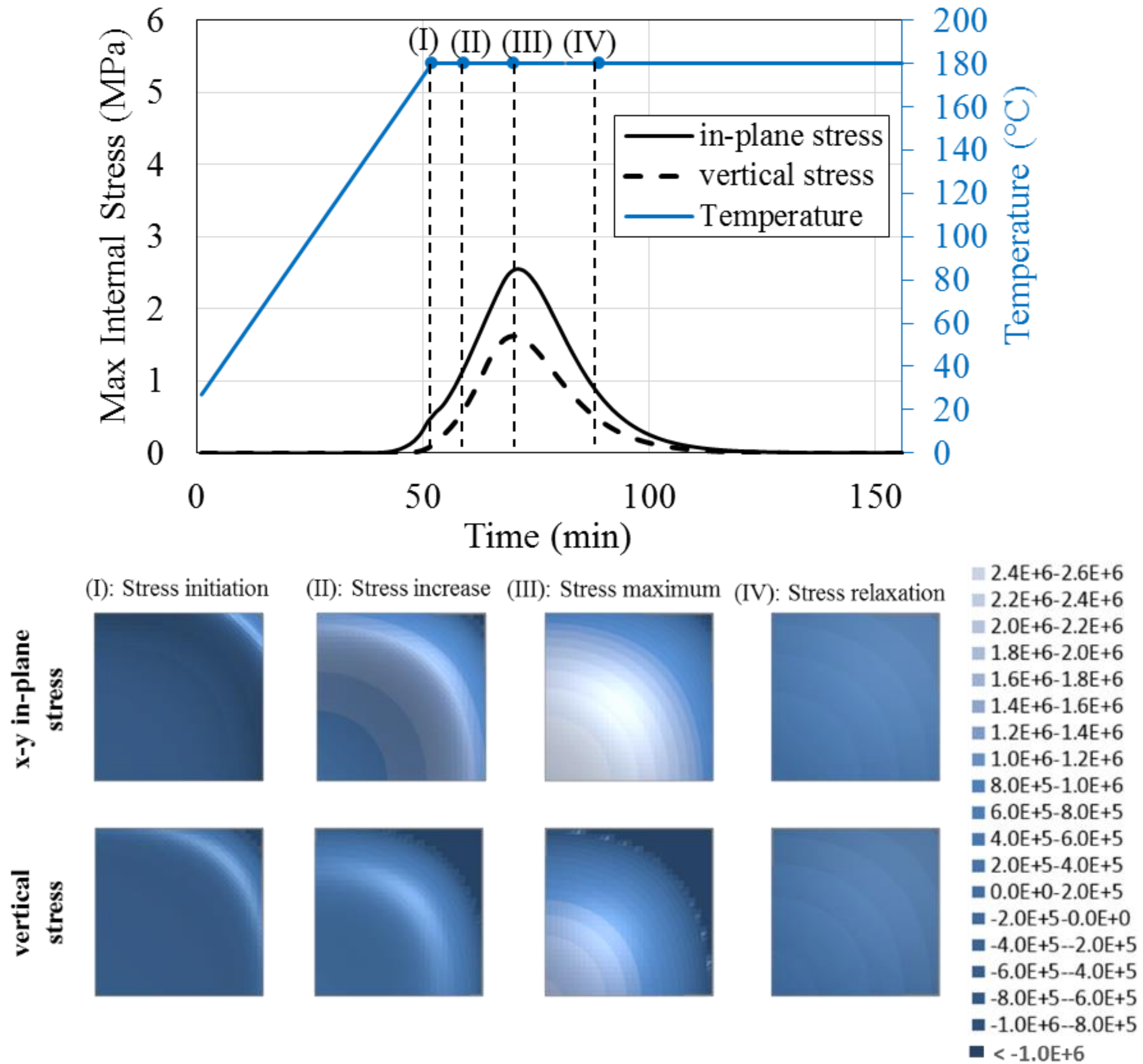

Fig. 6.12. The top plot is the maximum x-y in-plane internal stress and maximum vertical internal stress of nanosilver paste in a 6 $\times$6 mm^2 chip attachment during heating profile H (after room temperature treatment for 24 hours, then heat from room temperature to 180°C with temperature ramp rate of 3°C/min, and hold at 180°C for 104 minutes). The bottom figures show the distribution of internal stresses of nanosilver paste at the time points of (I), (II), (III), and (IV). For reason of symmetry, only a quarter of the paste is considered in the simulation. In each figure, the left bottom corner is the center of the chip and the right top corner is the corner of the chip.

In the 6 $\times$ 6 mm^2 chip attachments, for 1°C/min temperature ramp rate, the maximum internal stresses are generated at 179°C. The maximum x-y in-plane internal stress is 2.2 MPa and the maximum vertical internal stress is 1.3 MPa. Because of the slow temperature ramp rate, the paste does not have sufficient time to drying at relatively high temperatures, and the simulation does not show the completed stress relaxation region. For 3°C/min and 7.5°C/min temperature ramp rates, the maximum internal stresses are generated at 180°C temperature holding stage. The stress evolution in both cases are similar, with the maximum x-y in-plane internal stress of 2.6 MPa and the maximum vertical internal stress of 1.6 MPa. Fig. 6.12 shows the maximum internal stress versus time after 24 hours overnight treatment. After overnight treatment, a heating profile of 3°C/min to 180°C and 104 minutes holding time was applied. The maximum internal stresses during the whole process are generated at 180°C with the x-y in-plane internal stress of 2.6 MPa and vertical internal stress of 1.6 MPa. The stress analysis indicates that the maximum internal stress evolution of the paste in the chip attachment after overnight treatment is almost the same as that without overnight treatment.

According to the viscous model, the internal stress is related to the change rate of solvent concentration. For small area chip attachment, because the solvent can escape quickly from the paste, the change of solvent concentration is high, especially at high temperatures. The high solvent change rate will cause high internal stress in the paste. Meanwhile, because the solvent escapes quickly, the chip attachment can be thoroughly dried in a short time, which enables quick relaxation of the internal stress. For large area chip attachment, solvent in the paste cannot escape quickly even at high temperatures, and will not cause high change rate of solvent concentration. Therefore, the internal stress

of nanosilver paste in large area chip attachments at high temperature is usually smaller than that in small area chip attachments. However, the stress relaxation time for the paste in large area chip attachments is longer than that in the small area chip attachments.

From the analysis above, it is found that the temperature ramp rate and the overnight treatment do not significantly affect the maximum internal stress of nanosilver paste in chip attachments during drying process. However, the temperature ramp rate and the overnight treatment do affect the die-shear strength of the nanosilver chip attachments. It implies that except for the internal stress, other behavior of nanosilver paste during drying also has effect on the bonding strength of sintered silver joints. Since shrinkage of paste during drying is an important factor that affects the green density of nanosilver paste, the shrinkage profile of nanosilver paste under the different drying conditions from case A to H was studied. Relative green density can be calculated by the ratio of theoretical thickness with full density to real thickness after shrinkage. Table 6.4 shows the final shrinkage and estimated relative green density of the nanosilver paste after drying with different drying profiles (from case A to H).

Table 6.4: Simulated final shrinkage with estimated green density of nanosilver chip attachments after drying with different heating parameter combinations.

Case No.	Chip size (mm^2)	Pre-dying time (min)	Temperature ramp rate (°C/min)	Holding time (min)	Final shrinkage (%)	Relative green density (%)	Die-shear Strength (MPa)
A	3×3	0	1	0	36.83	50.25	39.9±2.5
B	3×3	0	3	104	36.42	49.92	27.1±2.9
C	3×3	0	7.5	135	35.43	49.15	14.3+4.2

D	3 × 3	1440	3	104	36.84	50.25	33.9±3.7
E	6 × 6	0	1	0	35.72	49.38	27.7±3.5
F	6 × 6	0	3	104	33.81	47.95	10.4±2.3
G	6 × 6	0	7.5	135	31.82	46.55	4.1±1.1
H	6 × 6	1440	3	104	35.36	49.10	22.0±4.6

Shrinkage is corresponding to the relative green density of nanosilver paste, as higher shrinkage will make the dried nanosilver paste denser, which can lead to higher green density. The high green density indicates the high sintered density of nanosilver paste, and enables high die-shear strength [32]. From Fig. 6.13, it can be concluded that the die-shear strength increases with increasing relative green density. Some exceptions were found: samples fabricated with heating profile A (3 × 3 mm^2 chip, 1°C/min ramp rate) and samples fabricated with heating profile D (3 × 3 mm^2 chip, overnight and 3°C/min ramp rate) have similar green densities but with different die-shear strength. The explanation is that the maximum internal stresses of nanosilver paste with heating profile D are higher than that with heating profile A, and the high internal stresses reduce the bonding strength of sintered silver joint. Similar situation can be found in samples fabricated with heating profile H (6 × 6 mm^2 chip, overnight and 3°C/min ramp rate) and samples fabricated with heating profile C (3 × 3 mm^2 chip, 7.5°C/min ramp rate), and the same explanation can be applied.

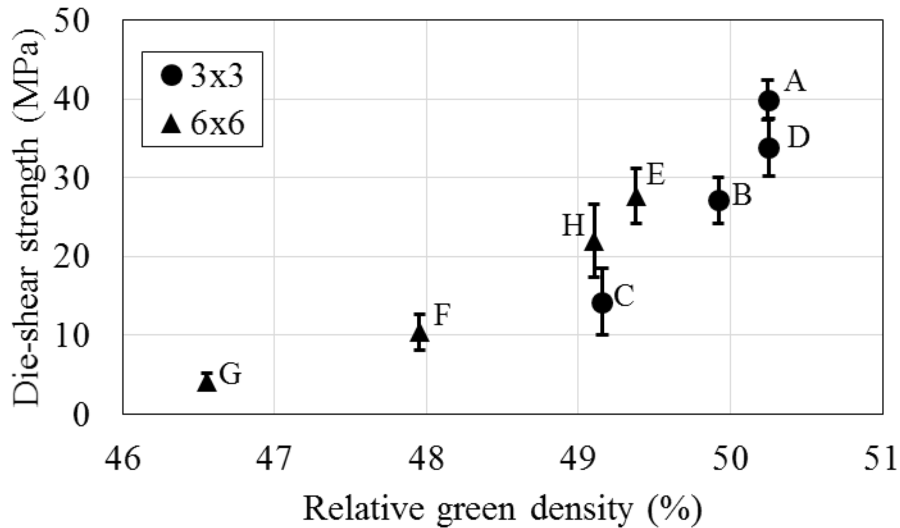

Fig. 6.13. Die-shear strength (experiment) vs. relative green density (simulation) of nanosilver chip attachment with different drying parameter combinations (case A to H).

6.4. Summary

In this chapter, chip attachments with the chip sizes of 3×3 mm^2 and 6×6 mm^2 were fabricated by nanosilver LTJT with different drying profiles. The effects of different room temperature pre-drying time (0 hour and 24 hours) and different temperature ramp rates (1°C/min, 3°C/min, and 7.5°C/min) on the bonding quality of the sintered nanosilver chip attachments were studied. The die-shear strength of chip attachments was evaluated. Numerical simulation were also applied to study the evolution of internal stresses and shrinkage of nanosilver paste in chip attachment during drying process. Several conclusions can be drawn:

The die-shear strength of sintered chip attachments increases with decreasing the temperature ramp rate during drying process. The room temperature pre-drying stage (overnight treatment) also helps increase the bonding strength of sintered nanosilver chip

attachments. The die-shear strength of large-area chip attachments (6×6 mm^2) is lower than that of small-area chip attachment (3×3 mm^2) with the same drying profile.

Numerical simulation of the internal stress evolution of nanosilver paste in the chip attachment during drying with different temperature ramp rates and overnight treatment shows that the maximum internal stresses are generated at the time when the paste is almost dry, and they are weakly affected by the temperature ramp rate or overnight treatment, as long as the maximum stresses are generated after the temperature reaches the maximum drying temperature. Furthermore, the maximum internal stresses are influenced by the size of chip attachments. In general, the internal stress is not strongly related to the bonding strength of sintered nanosilver chip attachments, or at least, the internal stress are not the major factor to determine the bonding strength.

Numerical simulation of the shrinkage evolution of nanosilver paste in chip attachment during drying shows that the shrinkage is strongly affected by the temperature ramp rate and overnight treatment, as the final shrinkage increases with decreasing the temperature ramp rate and with increasing overnight treatment time. Since the shrinkage of nanosilver paste in drying represents its green density, it is implied that a slow temperature ramp rate during drying and a long time room temperature pre-drying stage can increase the green density of nanosilver paste before sintering, thus can increase the strength of the sintered nanosilver bond-line.

Chapter 7. Summary and conclusions

7.1. Summary of the study

This study is focused on the analysis of the drying behavior of nanosilver paste in the chip attachment and process development for nanosilver-enabled low-temperature joining technique (LTJT). A diffusion-viscous model was developed for better understanding of the drying behavior in nanosilver LTJT. An algorithm for numerical simulation was developed and realized by C++ code, and it can simulate the drying behavior of nanosilver paste between the chip and the substrate. Furthermore, the effects of the drying parameters on the bonding quality of sintered nanosilver chip attachments were evaluated by experiments and numerical simulation. These drying parameters include external applied drying pressure, temperature ramp rate, and drying time, etc. Based on the analysis, a nanosilver LTJT process which limits the hot-pressing at a temperature below 200 ℃ was developed for bonding large-area chips.

In Chapter 2, a 2D model that was based on diffusion theory and viscous mechanics was developed to determine the stress evolution of nanosilver paste in a chip attachment during drying process. A numerical simulation algorithm of the model was developed and realized by a C++ program, which can simulate the 2D diffusion process of solvent moving with internal stress and strain evolution. With the help of program, the evolution of the solvent concentration distribution, internal stress distribution, and strain can be simulated for any drying profile with different combinations of time, temperature and external applied pressure.

In Chapter 3, the drying process of nanosilver paste in the chip attachment was simulated with the model. The drying behavior such as weight loss, shrinkage and internal stress

evolution in paste layer was demonstrated. The simulation results were in good agreement with the experimental data, which proved the validation of the diffusion-viscous model of the nanosilver paste drying in the chip attachment.

In Chapter 4, a design of experiments involving hot-pressing process parameters of nanosilver LTJT was carried out. The analysis shows that bonding quality increases with all evaluated process factors (drying time, drying pressure, sintering time, and sintering pressure), and no strong interaction is detected between any two factors. An improved nanosilver LTJT process which limits the external applied pressure to a temperature below 200 ℃ was developed. A nearly perfect, crack/void free joint layer with over 30 MPa bonding strength can be obtained for large-area chip (up to 10×10 mm^2) attachment with this process.

In Chapter 5, the effect of drying pressure on the bonding quality of the sintered silver bond-line was demonstrated. Large-area chip attachments were fabricated by nanosilver LTJT with different external applied drying pressure from 0 to 10 MPa. The die-shear strength of chip attachments and the microstructure of sintered silver bond-line were evaluated. Numerical simulation were also applied to study the evolution of internal stress of nanosilver paste in the chip attachment during drying process. The analysis indicates that the application of pressure helps decrease both x-y in-plane and vertical internal stresses, which can reduce the crack in the silver bond-line and the interface delamination.

In Chapter 6, the effects of different room temperature pre-drying time and different temperature ramp rates on the bonding quality of sintered nanosilver chip attachment were studied. The analysis indicates that the internal stress of nanosilver paste in chip

attachment is weakly influenced by the temperature ramp rate and overnight treatment. The shrinkage is strongly affected by the temperature ramp rate and overnight treatment, as the final shrinkage increases with decreasing the temperature ramp rate and with increasing overnight treatment time. High shrinkage can increase the green density of nanosilver paste before sintering, thus increase the sintered density and the strength of sintered nanosilver bond-line.

7.2. Suggestions for future work

In this study, a model and an algorithm of nanosilver paste drying between chip and substrate were developed, and the behavior of nanosilver paste during drying can be simulated. Though the simulation shows the similar trend as experiments, the accuracy of the simulated results can be further improved. Several suggestions are made to improve the model for simulation:

First, the physical properties of nanosilver paste need to be accurately measured. In the numerical simulation, some properties such as viscosity of paste, Poisson's ratio of paste, and diffusivity coefficient of solvent were either determined from approximation or simplified as constant. With more accurate physical properties (especially property profiles versus time, temperature, and concentration), the simulation results will be more accurate.

Second, the failure criteria of paste cracking and interface delamination need to be determined. As the model can be used to simulate the internal stress of nanosilver paste in chip attachment during drying, it is still unknown at what point the dried paste will rupture. Furthermore, after the failure of nanosilver paste at some locations, the stress

distribution should change. It is believed that the rupture stress of nanosilver paste is not a constant value but related to the localized solvent concentration. With failure criteria, it is possible to determine the exact time and location of the defect formation and can more accurately simulate the stress distribution.

References

[1] D. Frear and P. Vianco, "Intermetallic growth and mechanical behavior of low and high melting temperature solder alloys," *Metallurgical and Materials Transactions A,* vol. 25, pp. 1509-1523, 1994.

[2] Y. Wu, J. A. Sees, C. Pouraghabagher, L. A. Foster, J. L. Marshall, E. G. Jacobs, and R. F. Pinizzotto, "The formation and growth of intermetallics in composite solder," *Journal of Electronic Materials,* vol. 22, pp. 769-777, 1993.

[3] A. Sunwoo, J. Morris, and G. Lucey, "The growth of Cu-Sn intermetallics at a pretinned copper-solder interface," *Metallurgical Transactions A,* vol. 23, pp. 1323-1332, 1992.

[4] (2004). *Maxim Wafer-Level Package Assembly Guide*. Available: http://www.maximintegrated.com/app-notes/index.mvp/id/3377

[5] (2011). *SMT Board Assembly Process Recommendations*. Available: http://www.altera.com/literature/an/an353.pdf

[6] K. Suganuma, "Advances in lead-free electronics soldering," *Current Opinion in Solid State and Materials Science,* vol. 5, pp. 55-64, 2001.

[7] E. Wood and K. Nimmo, "In search of new lead-free electronic solders," *Journal of Electronic Materials,* vol. 23, pp. 709-713, 1994.

[8] C. Wu, D. Yu, C. Law, and L. Wang, "Properties of lead-free solder alloys with rare earth element additions," *Materials Science and Engineering: R: Reports,* vol. 44, pp. 1-44, 2004.

[9] K. Kim, S. Huh, and K. Suganuma, "Effects of intermetallic compounds on properties of Sn–Ag–Cu lead-free soldered joints," *Journal of Alloys and Compounds,* vol. 352, pp. 226-236, 2003.

[10] W. Choi, E. Yeh, and K. Tu, "Mean-time-to-failure study of flip chip solder joints on Cu/Ni (V)/Al thin-film under-bump-metallization," *Journal of applied physics,* vol. 94, pp. 5665-5671, 2003.

[11] B. Vandevelde, M. Gonzalez, P. Limaye, P. Ratchev, and E. Beyne, "Thermal cycling reliability of SnAgCu and SnPb solder joints: a comparison for several IC-packages," *Microelectronics Reliability,* vol. 47, pp. 259-265, 2007.

[12] M. Zwolinski, J. Hickman, H. Rubin, Y. Zaks, S. McCarthy, T. Hanlon, P. Arrowsmith, A. Chaudhuri, R. Hermansen, and S. Lan, "Electrically conductive adhesives for surface mount solder replacement," *Components, Packaging, and Manufacturing Technology, Part C, IEEE Transactions on,* vol. 19, pp. 241-250, 1996.

[13] J. Jagt, P. Beris, and G. Lijten, "Electrically conductive adhesives: A prospective alternative for SMD soldering?," *Components, Packaging, and Manufacturing Technology, Part B: Advanced Packaging, IEEE Transactions on,* vol. 18, pp. 292-298, 1995.

[14] R. Gomatam and K. L. Mittal, *Electrically Conductive Adhesives*: BRILL, 2008.

[15] R. S. Rorgren and J. Liu, "Reliability assessment of isotropically conductive adhesive joints in surface mount applications," *Components, Packaging, and Manufacturing Technology, Part B: Advanced Packaging, IEEE Transactions on,* vol. 18, pp. 305-312, 1995.

[16] H. L. Hvims, "Conductive adhesives for SMT and potential applications," *Components, Packaging, and Manufacturing Technology, Part B: Advanced Packaging, IEEE Transactions on,* vol. 18, pp. 284-291, 1995.

[17] H. B. e. al., "Factors that influence the electrical contact resistance of isotropic adhesive joints during climate chamber testing," *Proc. Adhesives Electron.,* 1996.

[18] M. J. Yim, Y. Li, K.-s. Moon, K. W. Paik, and C. Wong, "Review of recent advances in electrically conductive adhesive materials and technologies in electronic packaging," *Journal of adhesion science and technology,* vol. 22, pp. 1593-1630, 2008.

[19] Y. Li and C. Wong, "Recent advances of conductive adhesives as a lead-free alternative in electronic packaging: materials, processing, reliability and applications," *Materials Science and Engineering: R: Reports,* vol. 51, pp. 1-35, 2006.

[20] U. Scheuermann and P. Wiedl, "Low temperature joining technology - a high reliability alternative to solder contacts," presented at the 3rd Workshop on metal ceramic materials for functional applications, Austria, 1997.

[21] E. Schulze, C. Mertens, and A. Lindemann, "Low Temperature Joining Technique - a Solution for Automotive Power Electronics," presented at the PCIM, Nurnberg, Germany, 2009.

[22] H. Schwarzbauer and R. Kuhnert, "Novel large area joining technique for improved power device performance," *Industry Applications, IEEE Transactions on,* vol. 27, pp. 93-95, 1991.

[23] C. Gobl and J. Faltenbacher, "Low temperature sinter technology die attachement for power electronic applications," presented at the Conference on Integration Power Systems (CIPS), Nurnberg, 2010.

[24] J. N. Calata, T. G. Lei, and G. Q. Lu, "Sintered nanosilver paste for high-temperature power semiconductor device attachment," *International Journal of Materials & Product Technology,* vol. 34, pp. 95-110, 2009.

[25] E. Schulze, C. Mertens, and A. Lindemann, "Pure Low Temperature Joining Technique power module for automotive production needs," presented at the Integrated Power Electronics Systems (CIPS), 2010 6th International Conference on, 2010.

[26] T. Wang, X. Chen, G. Q. Lu, and G. Y. Lei, "Low-temperature sintering with nano-silver paste in die-attached interconnection," *Journal of Electronic Materials,* vol. 36, pp. 1333-1340, 2007.

[27] U. Scheuermann, and P. Beckedahl, "The Road to the Next Generation Power Module - 100% Solder free Design," presented at the The 5th International Conference on Integrated Power Electronics Systems (CIPS 2008), Nuremberg, Germany, 2008.

[28] U. Scheuermann, "Reliability challenges of automotive power electronics," *Microelectronics Reliability,* vol. 49, pp. 1319-1325, 2009.

[29] J. Glazer, "Microstructure and Mechanical-Properties of Pb-Free Solder Alloys for Low-Cost Electronic Assembly - a Review," *Journal of Electronic Materials,* vol. 23, pp. 693-700, 1994.

[30] Z. Zhang and G. Q. Lu, "Pressure-assisted low-temperature sintering of silver paste as an alternative die-attach solution to solder reflow," *IEEE Transactions on Electronics Packaging Manufacturing,* vol. 25, pp. 279-283, 2002.

[31] G. Lei, "Thermo-Mechanical Reliability of Low-Temperature Sintered Attachments on Direct Bonded Aluminum (DBA) Substrate for High-Temperature Electronics Packaging," Ph.D., Materials Science and Engineering, Virginia Polytechnic Institute and State University, 2010.

[32] M. Knoerr and A. Schletz, "Power semiconductor joining through sintering of silver nanoparticles: Evaluation of influence of parameters time, temperature and pressure on density, strength and reliability," presented at the Integrated Power Electronics Systems (CIPS), 2010 6th International Conference on, 2010.

[33] J. G. F. Bai and G. Q. Lu, "Thermomechanical reliability of low-temperature sintered silver die attached SiC power device assembly," *IEEE Transactions on Device and Materials Reliability,* vol. 6, pp. 436-441, 2006.

[34] M. Knoerr, S. Kraft, and A. Schletz, "Reliability assessment of sintered nano-silver die attachment for power semiconductors," in *Electronics Packaging Technology Conference (EPTC), 2010 12th*, 2010, pp. 56-61.

[35] G. Q. Lu, J. N. Calata, G. Y. Lei, and X. Chen, "Low-temperature and Pressureless Sintering Technology for High-performance and High-temperature Interconnection of Semiconductor Devices," presented at the Thermal, Mechanical and Multi-Physics Simulation Experiments in Microelectronics and Micro-Systems, 2007. EuroSime 2007. International Conference on, 2007.

[36] G. Q. Lu, J. N. Calata, Z. Y. Zhang, and J. G. Bai, "Lead-free, low-temperature sintering die-attach technique for high-performance and high-temperature packaging," *Proceedings of the Sixth IEEE CPMT Conference on High Density Microsystem Design and Packaging and Component Failure Analysis (Hdp'04),* pp. 42-46, 2004.

[37] J. G. Bai, Z. Z. Zhang, J. N. Calata, and G. Q. Lu, "Low-temperature sintered nanoscale silver as a novel semiconductor device-metallized substrate interconnect material," *IEEE Transactions on Components and Packaging Technologies,* vol. 29, pp. 589-593, 2006.

[38] T. G. Lei, J. N. Calata, G. Q. Lu, X. Chen, and S. F. Luo, "Low-Temperature Sintering of Nanoscale Silver Paste for Attaching Large-Area (> 100 mm(2)) Chips," *IEEE Transactions on Components and Packaging Technologies,* vol. 33, pp. 98-104, 2010.

[39] G. W. Scherer, "Theory of drying," *Journal of the American Ceramic Society,* vol. 73, pp. 3-14, 1990.

[40] S. Ghosal, A. Emami-Naeini, Y. P. Harn, B. S. Draskovich, and J. P. Pollinger, "A physical model for the drying of gelcast ceramics," *Journal of the American Ceramic Society,* vol. 82, pp. 513-520, 1999.

[41] R. Dwivedi, "Drying behaviour of alumina gels," *Journal of materials science letters,* vol. 5, pp. 373-376, 1986.

[42] T. Sherwood, "The drying of solids—I," *Industrial & Engineering Chemistry,* vol. 21, pp. 12-16, 1929.

[43] T. Sherwood, "The drying of solids—II," *Industrial & Engineering Chemistry,* vol. 21, pp. 976-980, 1929.

[44] T. Sherwood, "The Drying of Solids—III1 Mechanism of the Drying of Pulp and Paper," *Industrial & Engineering Chemistry,* vol. 22, pp. 132-136, 1930.

[45] J. Van Brakel, "Pore space models for transport phenomena in porous media review and evaluation with special emphasis on capillary liquid transport," *Powder Technology,* vol. 11, pp. 205-236, 1975.

[46] K. Watson, "An instantaneous profile method for determining the hydraulic conductivity of unsaturated porous materials," *Water Resources Research,* vol. 2, pp. 709-715, 1966.

[47] G. Bramhall, "The validity of Darcy's law in the axial penetration of wood," *Wood Science and Technology,* vol. 5, pp. 121-134, 1971.

[48] F. A. Dullien, *Porous media: fluid transport and pore structure*: Access Online via Elsevier, 1991.

[49] S. B. Nasrallah and P. Perre, "Detailed study of a model of heat and mass transfer during convective drying of porous media," *International Journal of Heat and Mass Transfer,* vol. 31, pp. 957-967, 1988.

[50] P. Debye and R. L. Cleland, "Flow of Liquid Hydrocarbons in Porous Vycor," *Journal of applied physics,* vol. 30, pp. 843-849, 1959.

[51] G. W. Scherer and R. M. Swiatek, "Measurement of permeability II. Silica gel," *Journal of non-crystalline solids,* vol. 113, pp. 119-129, 1989.

[52] V. Gekas and I. Lamberg, "Determination of diffusion coefficients in volume-changing systems—application in the case of potato drying," *Journal of Food Engineering,* vol. 14, pp. 317-326, 1991.

[53] L. Hassini, S. Azzouz, R. Peczalski, and A. Belghith, "Estimation of potato moisture diffusivity from convective drying kinetics with correction for shrinkage," *Journal of Food Engineering,* vol. 79, pp. 47-56, 2007.

[54] S. Pang, "Relationship between a diffusion model and a transport model for softwood drying," *Wood and Fiber Science,* vol. 29, pp. 58-67, 1997.

[55] K. Sakata, "A study on moisture diffusion in drying and drying shrinkage of concrete," *Cement and Concrete Research,* vol. 13, pp. 216-224, 1983.

[56] Z. Bažant and L. Najjar, "Drying of concrete as a nonlinear diffusion problem," *Cement and Concrete Research,* vol. 1, pp. 461-473, 1971.

[57] Z. Bažant and L. Najjar, "Nonlinear water diffusion in nonsaturated concrete," *Matériaux et Construction,* vol. 5, pp. 3-20, 1972.

[58] Z. P. Bazănt and W. J. Raftshol, "Effect of cracking in drying and shrinkage specimens," *Cement and Concrete Research,* vol. 12, pp. 209-226, 1982.

[59] A. A. J. Ketelaars, "Drying deformable media kinetics, shrinkage and stresses," *Drying Technology,* vol. 12, pp. 983-987, 1994.

[60] T. C. Powers, "A discussion of cement hydration in relation to the curing of concrete," in *Highway Research Board Proceedings*, 1947.

[61] J. Hanson, "Effects of Curing and Drying Enviroments on Splitting Tensile Strength of Concrete," in *ACI Journal Proceedings*, 1968.

[62] S. E. Pihlajavaara, *On the main features and methods of investigation of drying and related phenomena in concrete* vol. 100: University of Helsinki., 1965.

[63] M. A. Biot, "Theory of propagation of elastic waves in a fluid-saturated porous solid. II. Higher frequency range," *The Journal of the Acoustical Society of America,* vol. 28, p. 179, 1956.

[64] M. A. Biot, "Theory of propagation of elastic waves in a fluid-saturated porous solid. I. Low-frequency range," *The Journal of the Acoustical Society of America,* vol. 28, p. 168, 1956.

[65] R. K. Bordia and G. W. Scherer, "On constrained sintering—I. Constitutive model for a sintering body," *Acta Metallurgica,* vol. 36, pp. 2393-2397, 1988.

[66] R. K. Bordia and G. W. Scherer, "On constrained sintering—II. Comparison of constitutive models," *Acta Metallurgica,* vol. 36, pp. 2399-2409, 1988.

[67] M. Biot, "Theory of Stress-Strain Relations in Anisotropic Viscoelasticity and Relaxation Phenomena," *Journal of applied physics,* vol. 25, pp. 1385-1391, 1954.

[68] R. Christensen, *Theory of viscoelasticity: an introduction*: Access Online via Elsevier, 1982.

[69] G. W. Scherer and G. W. Scherer, *Relaxation in glass and composites*: Wiley New York (NY) et al., 1986.

[70] A. G. Evans and C. Hsueh, "Behavior of large pores during sintering and hot isostatic pressing," *Journal of the American Ceramic Society,* vol. 69, pp. 444-448, 1986.

[71] R. Raj and R. Bordia, "Sintering behavior of bi-modal powder compacts," *Acta Metallurgica,* vol. 32, pp. 1003-1019, 1984.

[72] R. Bordia and R. Raj, "Sintering behavior of ceramic films constrained by a rigid substrate," *Journal of the American Ceramic Society,* vol. 68, pp. 287-292, 1985.

[73] G. W. Scherer, "Sintering inhomogeneous glasses: Application to optical waveguides," *Journal of non-crystalline solids,* vol. 34, pp. 239-256, 1979.

[74] G. W. Scherer and T. Garino, "Viscous sintering on a rigid substrate," *Journal of the American Ceramic Society,* vol. 68, pp. 216-220, 1985.

[75] G. W. Scherer, "Viscous Sintering under a Uniaxial Load," *Journal of the American Ceramic Society,* vol. 69, pp. C-206-C-207, 1986.

[76] G. W. Scherer, "Viscous Sintering with a Pore-Size Distribution and Rigid Inclusions," *Journal of the American Ceramic Society,* vol. 71, pp. C447-C448, 1988.

[77] T. J. Garino and H. K. Bowen, "Kinetics of Constrained-Film Sintering," *Journal of the American Ceramic Society,* vol. 73, pp. 251-257, 1990.

[78] G. W. Scherer, "Viscous sintering of particle-filled composites," *American Ceramic Society bulletin,* vol. 70, pp. 1059-1063, 1991.

[79] G.-Q. Lu, R. C. Sutterlin, and T. K. Gupta, "Effect of Mismatched Sintering Kinetics on Camber in a Low-Temperature Cofired Ceramic Package," *Journal of the American Ceramic Society,* vol. 76, pp. 1907-1914, 1993.

[80] L. Mayor and A. Sereno, "Modelling shrinkage during convective drying of food materials: a review," *Journal of Food Engineering,* vol. 61, pp. 373-386, 2004.

[81] N. Wang and J. G. Brennan, "Changes in structure, density and porosity of potato during dehydration," *Journal of Food Engineering,* vol. 24, pp. 61-76, 1995.

[82] M. Perez and A. Calvelo, "Modeling the thermal conductivity of cooked meat," *Journal of Food Science,* vol. 49, pp. 152-156, 1984.

[83] S. F. Li and H. M. Ong, "Infinite dilution diffusion coefficients of several alcohols in water," *Journal of Chemical and Engineering Data,* vol. 35, pp. 136-137, 1990.

[84] G. D. Smith, *Numerical solution of partial differential equations: finite difference methods*: Oxford University Press, 1985.

[85] O. S.-b. Mass, T. E. C. A. Order, and S.-W. Schemes, "Numerical methods for partial differential equations," 1992.

[86] T. Wang, M. H. Zhao, X. Chen, G. Q. Lu, K. Ngo, and S. F. Luo, "Shrinkage and Sintering Behavior of a Low-Temperature Sinterable Nanosilver Die-Attach Paste," *Journal of Electronic Materials,* vol. 41, pp. 2543-2552, 2012.

[87] K. Xiao, J. Calata, K. Ngo, D. Ibitayo, and G.-Q. Lu, "Large-Area Chip Attachment by Sintering Nanosilver Paste: Process Improvement by Nondestructive Characterization," *Transactions of The Japan Institute of Electronics Packaging,* vol. 4, pp. 101-109, 2011.

[88] R. L. Coble, "Sintering Crystalline Solids. I. Intermediate and Final State Diffusion Models," *Journal of applied physics,* vol. 32, pp. 787-792, 1961.

[89] R. L. Coble, "Sintering Crystalline Solids. II. Experimental Test of Diffusion Models in Powder Compacts," *Journal of applied physics,* vol. 32, pp. 793-799, 1961.

[90] M. N. Rahaman, *Ceramic processing and sintering*. New York: M. Dekker, 1995.

[91] M. N. Rahaman, L. C. Dejonghe, and M. Y. Chu, "Effect of Green Density on Densification and Creep during Sintering," *Journal of the American Ceramic Society,* vol. 74, pp. 514-519, 1991.

Appendix A: C++ code and input format for numerical simulation of nanosilver paste drying in the chip attachment

C++ source code of the main modules

The C++ source code can be compiled and executed in Microsoft Visual C++ 2010 Express. The code of some main modules are shown below:

(1). Determine of the time increment dt.

```
double dtDetermine(double dx, double dy, double T0, double RT, double time){
	//element length: dx, dy
	//initial temperature: T0
	//temperatre ramp rate: RT
	//Segment duration time: time
	double dt, Dmax, Tmax, dxy;
	if(RT<=0.0)
		Tmax=T0;
	else
		Tmax=T0+RT*time;
	Dmax=D(Tmax);
	if(dx<=dy)
		dxy=dx;
	else
		dxy=dy;
	dt=0.2;
	while(dt>=dxy*dxy/(4.0*Dmax))
		dt=dt/2;
	return dt;
}
```

(2). Determine of new solvent concentration profile.

```
double DiffusionProfile(double **Cl, double **dCl, double **Clnew, double D, double
Jxy, double den0, long int k1, long int k2, double dx, double dy, double dt){
	//old concentration profile: Cl[k1][k2]
	//concentration change rate: dCl=(Clnew-Cl)/dt
	//new concentration profile: Clnew
	//diffusivity of liquid: D
	//mass flux rate: Jxy
	//number of meshed elements: k1, k2
	//element length: dx, dy
	//time step: dt
```

```
	long int i, j;
	double Clave;

	for(i=1;i<=k1;i++)
		Cl[0][i]=Cl[1][i];
	for(j=0;j<=k2;j++)
		Cl[j][0]=Cl[j][1];

	for(i=k1-1;i>=1;i--){
		Clnew[k2][i]=Cl[k2-1][i]*exp(-Jxy*dy/(den0*D*1000.0));
		dCl[k2][i]=(Clnew[k2][i]-Cl[k2][i])/dt;
	} //horizental edge

	for(j=k2-1;j>=1;j--){
		Clnew[j][k1]=Cl[j][k1-1]*exp(-Jxy*dx/(den0*D*1000.0));
		dCl[j][k1]=(Clnew[j][k1]-Cl[j][k1])/dt;
	} //vertical edge

	//Fick's 2nd law
	for(j=k2-1;j>=1;j--){
		for(i=k1-1;i>=1;i--){
			dCl[j][i]=D/(dx*dx)*(Cl[j][i+1]+Cl[j][i-1]-
2.0*Cl[j][i])+D/(dy*dy)*(Cl[j+1][i]+Cl[j-1][i]-2.0*Cl[j][i]);
			Clnew[j][i]=dt*dCl[j][i]+Cl[j][i];
		}
	}

	Clave=0.0;
	for(j=1;j<=k2;j++)
		for(i=1;i<=k1;i++)
			Clave+=Cl[j][i];
	Clave=Clave/(k1*k2);

	return Clave;
	//return average Cl
}
```

(3). Determine the stress distribution.

```
double StressDistribution(double **sx, double **sz, double *smm, double **Cl, double
**dCl, double **Ep, double **v, double **def, long int k1, long int k2, double Papp,
double den0, double denl, double Cl0, double a1, double a2){
	//stress at X direction: sx
	//stress at Z direction: sz
```

```
//concentration profile: Cl
//concentration rate profile: dCl
//viscosity of paste element as function of (Cl): Ep
//Poisson's ratio of paste element as function of (Cl): v
//free strain rate of elements as function of (Cl): def
//number of meshed elements: k1, k2
//external applied pressure: Papp
//initial density of paste: den0
//density of liquid: denl
//initial liquid concentration: Cl0
//define empirical formula: Va/V0=a1*(Cl0-Cl)^a2

double dez, v;
long int i, j;
for (j=1;j<=k2;j++){
        for(i=1;i<=k1;i++){
                //ef[i]=(den0/denl*(Cl[i]-Cl0)+a1*pow((Cl0-Cl[i]),a2))/3.0;
                def[j][i]=telldef(Cl[j][i]);
                Ep[j][i]=tellEp(Cl[j][i]);
                v[j][i]=tellv(Cl[j][i]);
        }
}//calculate def, Ep, v at different locations [j][i]

double temp1, temp2;
temp1=0.0;
temp2=0.0;
for(j=1;j<=k2;j++){
        for (i=1;i<=k1;i++){
                temp1+=Ep[j][i]*def[j][i];
                temp2+=Ep[j][i];
        }
}
dez=(temp1*(1.0+v)-Papp*k1*k2*(1.0-v-2.0*v*v))/(temp2*(1.0-v)); //calculate
strain rate at Z direction

smm[0]=Ep[1][1]*(v*dez-(v+1.0)*def[1][1])/(1.0-v-2.0*v*v); //smm[0]=sx min
smm[1]=Ep[1][1]*dez/(1.0+v)+sx[1][1]; //smm[1]=sz min
smm[2]=smm[0]; //smm[2]=sx max
smm[3]=smm[1]; //smm[3]=sz max

for(j=1;j<=k2;j++){
        for(i=1;i<=k1;i++){
                sx[j][i]=Ep[j][i]*(v*dez-(v+1.0)*def[j][i])/(1.0-v-2.0*v*v);
                sz[j][i]=Ep[j][i]*dez/(1.0+v)+sx[j][i];
                if(sx[j][i]<smm[0])
                        smm[0]=sx[j][i];
```

```
                if(sx[j][i]>smm[2])
                        smm[2]=sx[j][i];
                if(sz[j][i]<smm[1])
                        smm[1]=sz[j][i];
                if(sz[j][i]>smm[3])
                        smm[3]=sz[j][i];
            }
    } //calculate stress at X and Z direction at different locations [j][i]
    return dez;
}
```

(4). The main loop

```
int main(array<System::String ^> ^args)
{
    //input parameters
    long int k1, k2, dk1out, dk2out, Seg;
    double l1, l2, Cl0, den0, denl, T0, RT, P0, RP, time, dtout, **Cl;
    //number of meshed elements: k1, k2
    //output meshed elements increment: dkout
    //number of profile segments: Seg;
    //chip length: l1, l2
    //initial liquid concentration: Cl0
    //initial density of paste: den0
    //density of liquid: denl
    //Segment T-P-t profile intial temperature: T0
    //temperature ramp rate: RT
    //Segment T-P-t profile initial pressure: P0;
    //pressure ramp rate: RP;
    //Segment time duration: time;
    //output time increment step: dtout (dtout>=1s)
    //concentration profile: Cl[])

    //internal parameters
    double dt, dx, dy, D, Jxy, Temp, Papp, Ttotal, Clave, dez, ez, **Clnew, **dCl,
**Ep, **sx, **sz, **def, smm[4];
    long int i, j, tstep, tstep2, l, count;
    //time increment step: dt (dt<=0.2s)
    //element length: dx, dy
    //liquid diffusivity: D
    //mass flux rate: Jxy
    //temperature: Temp
    //external pressure: Papp
    //passed time: Ttotal
    //Average liquid concentration: Clave
```

```
	//strain rate at Z direction: dez
	//strain at Z direction: ez
	//new concentration profile: Clnew[k2][k1]
	//concentration profile change rate: dCl[k2][k1]
	//viscosity: Ep[k2][[k1]
	//stress at X direction: sx[k2][k1];
	//stress at Z direction: sz[k2][k1];
	//free strain rate: def[k2][k1];
	//mimimum and maximum stress: smm[0]=sx min, smm[1]=sz min, smm[2]=sx
max, smm[3]=sz max;

	Input(k1, k2, l1, l2, Cl0, den0, denl, dk1out, dk2out, dtout, Seg); //define
simulation parameter and material properties
	Input(Cl); //define initial concentration

	//initialize
	Clnew=new double* [k2+1];
	dCl=new double* [k2+1];
	Ep=new double* [k2+1];
	sx=new double* [k2+1];
	sz=new double* [k2+1];
	def=new double* [k2+1];
	for(j=0;j<=k2;j++){
		Clnew[j]=new double [k1+1];
		dCl[j]=new double [k1+1];
		Ep[j]=new double [k1+1];
		sx[j]=new double [k1+1];
		sz[j]=new double [k1+1];
		def[j]=new double [k1+1];
	}

	dx=l1/(2.0*k1);
	dy=l2/(2.0*k2);
	Ttotal=0.0;
	ez=0.0;

	for(count=1;count<=Seg;count++){
		fin1>>T0>>RT>>P0>>RP>>time;

		dt=dtDetermine(dx, dy, T0, RT, time); //find dt
		tstep=(long int)(time/dt); //number of calculation loops
		tstep2=(long int)(dtout/dt); //nunber of output loops

		//check point
		cout<<"Segment "<<count<<": dt="<<dt<<"\tstep needed:
"<<tstep<<endl;
```

```
            //check point end

            Temp=T0;
            Papp=P0;
            for(l=1;l<=tstep;l++){
                        Ttotal+=dt;
                        Temp+=RT*dt;
                        D=D(T); //define D(T)
                        Jxy=J(T, Cl); //define J(T,Cl)=a3*exp(-a4/T)*Cl;
                        Papp+=RP*dt;
                        Clave=DiffusionProfile(Cl, dCl, Clnew, D, Jxy, den0, k1, k2, dx,
dy, dt);
                        dez=StressDistribution(sx, sz, smm, Cl, dCl, Ep, v, def, k1, k2,
Papp, den0, denl, Cl0, a1, a2);
                        ez+=dez*dt;
                        for(j=0;j<=k2;j++)
                                    for(i=0;i<=k1;i++)
                                                Cl[j][i]=Clnew[j][i];

                        //output
                        if(l%tstep2==0){
                                    output(Ttotal, Temp, Clave, ez, dez, smm[0], smm[1],
smm[2], smm[3]);
                                    output(Cl, sx, sz);
                        }
            }
      }
      delete [] (Cl, Clnew, dCl, Ep, def, sz, sx);  //release memory
      cout<<"Simulation completed!"<<endl;
      getchar();
      return 0;
}
```

The details of input and output functions are not shown in the source code above.

Input file format

The input parameters for simulation can be saved as a text file of the name of "profile2D.txt". The initial solvent concentration profile need to be saved as "Concentration0.txt". The input format are shown below:

number of grids in x direction; number of grids in y direction;

chip length in x direction (m); chip length in y direction (m);

nomalized solvent concentration; initial density of paste (g/cm^3); initial density of solvent (g/cm^3);

grid increment for output in x direction; grid increment for output in y direction; time increment for output (>=1.0s);

number of heating segments;

[for each heating segment]

initial temperature T0 (K); temperature ramp RT (K/s); initial pressure P0 (Pa); pressure ramp RP (Pa/s); duration time (s);

For example, a 0.003 m $\times$ 0.005 m chip attachment heated from 297 K with temperature ramp rate of 0.05 K/s for 3120 s with no pressure (segment 1), and then heated at 453 K with 0 K/s temperature ramp rate under 150 Pa uniaxial pressure for 6240 s (segment 2). The number of meshing grids for a quarter chip are 30 $\times$ 50. The output grids in x direction is one out of 3, the output grids in y direction is one out of 2, and the output time increment is 60 s. The output parameters are shown below. Row 3 of output are properties of nanosilver paste, which is not explicit in the heating case.

"Profile2D.txt"

```
30;     50;
0.003;  0.005;
0.17;   4.01;   1.0;
3       2       60.0
2
```

297.0 0.05 0.0 0.0 3120.0

453.0 0.0 150.0 0.0 6240.0

“Concentration0.txt”

0.17 0.17 … 0.17

0.17 0.17 … 0.17

. . … .

. . … .

0.17 0.17 … 0.17

(30 columns and 50 rows)

Appendix B: Mechanical properties and creep behavior of sintered nanosilver joint layer

Experimental Procedures

The nanosilver paste (from NBE Tech, LLC) was printed on alumina substrates, dried at 50 ℃, 100 ℃ and 180 ℃, then sintered at 275 ℃ on hot plate for 10 minutes. The drying and sintering profile is shown in Fig. B.1. The sintered nanosilver paste, which was in thin film shape with the thickness ranging from 50 μm to 75 μm, was considered as a homogenous and isotropic material in macro scale, as shown in Fig. B.2. The sintered films were then cut to smaller samples with the dimensions of 20.0 × 4.0 mm^2, for the mechanical properties tests.

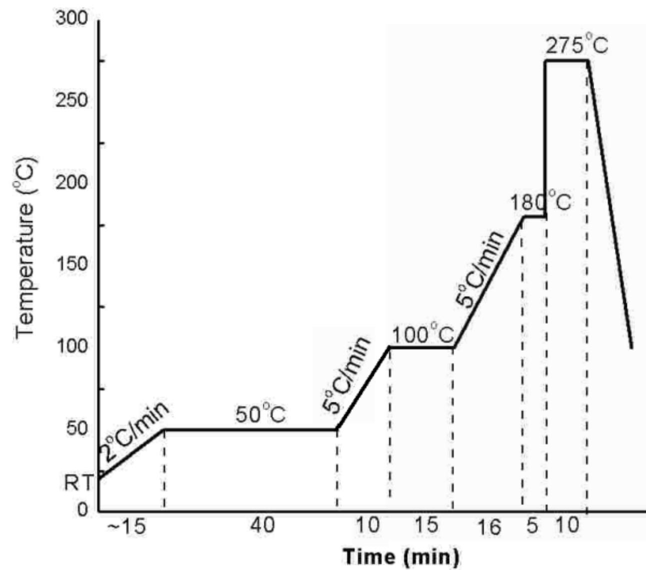

Fig. B.1. Drying and sintering profile of open-faced nanosilver paste.

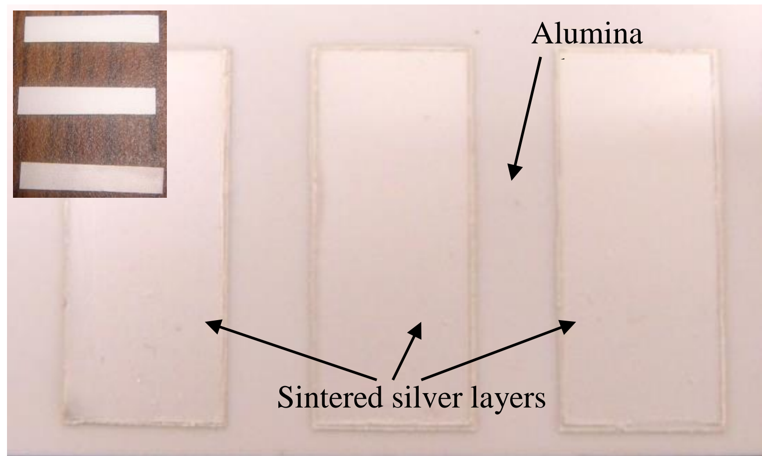

Fig. B.2. Sintered nanosilver paste films on alumina substrate, the inset shows the final samples used in the mechanical properties testing.

The uniaxial tension tests were carried out by using the equipment of Dynamic Mechanical Analysis (DMA) Q800 series. Since the displacement of samples during the test was relatively small, a force-controlling testing method was applied for the tension tests. The force ramp rate was controlled between 2N/min and 3N/min in order to make sure the tensile stress ramp rate was 10.0 MPa/min. Samples were tested at 25 ℃, 50 ℃, 100 ℃, 150 ℃ and 200 ℃, respectively. Three repetitions were tested at each temperature.

A series of creep tests for sintered nanosilver paste were carried out using the equipment of DMA. According to the preliminary results from the tension tests, the constant tensile stress that applied in the creep test was set to 10 MPa in order to keep an intermediate value comparing to the ultimate stress. Tests were done at 75 ℃, 100 ℃, 150 ℃, 200 ℃ and 250 ℃, respectively.

Experimental Results

Stress-strain curves at different temperatures

As shown in Fig. B.3, the stress-strain curves of simple uniaxial tension at different temperatures indicate that the mechanical behavior of sintered nanosilver paste is strongly related to the temperature. Fig. B.4 and Fig. B.5 show the statistical values of some internal mechanical properties of the sintered paste. The Young's modulus is 18 GPa at room temperature, 11 GPa at 100 ℃ and 4 GPa at 200 ℃; ultimate stress is 55 MPa at room temperature, 34 MPa at 100 ℃, and 17 MPa at 200 ℃. Both Young's modulus and ultimate stress decrease with increasing temperature, and the ultimate failure strain increases with increasing temperature. The ultimate strain is 0.6% at room temperature, 0.8% at 100 ℃, and 1.8% at 200 ℃. Compared to those properties in room temperature, the Young's modulus and the ultimate stress at 200°C decrease approximately 80% and 70%, respectively. The ultimate strain at 200 ℃ increases approximately 200% comparing to that in room temperature.

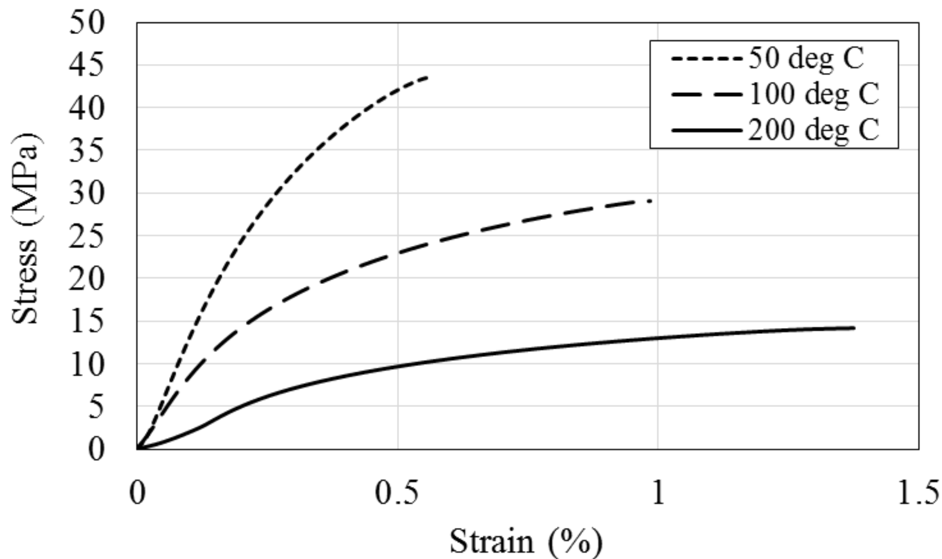

Fig. B.3. Stress-Strain relationships at different temperatures.

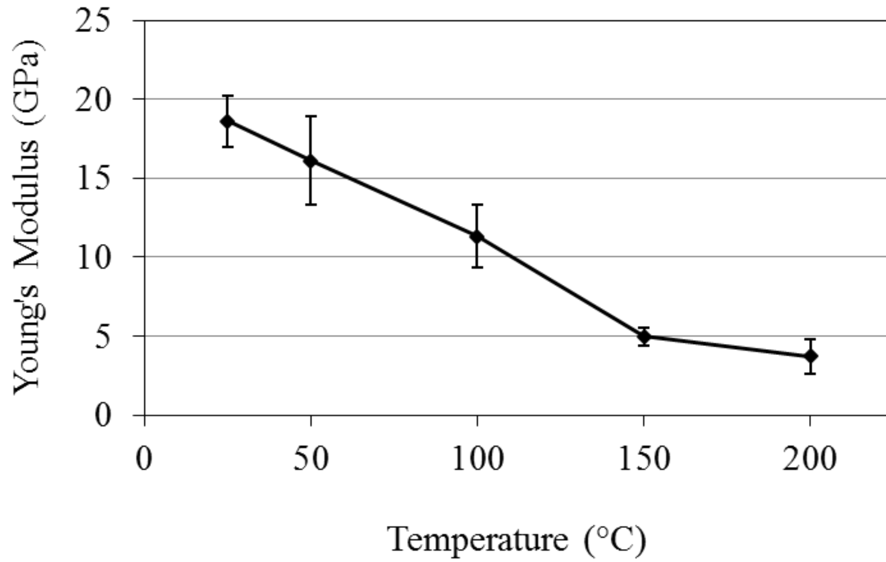

Fig. B.4. Young's modulus of sintered silver layers at different temperatures.

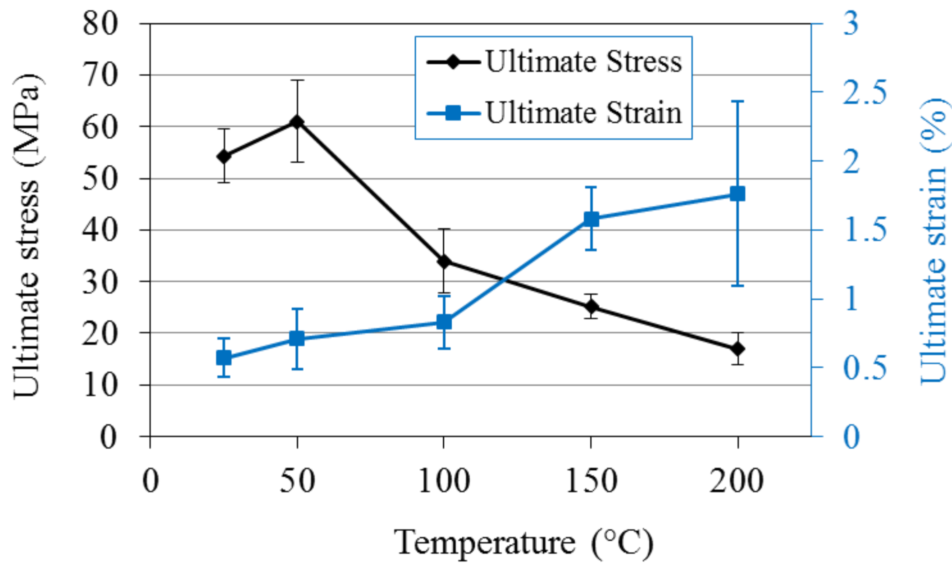

Fig. B.5. Ultimate stress and strain of sintered silver layers at different temperatures.

Creep behavior of sintered paste at different temperatures

Creep behavior reveals the viscosity of materials. From the constant stress tests, we obtained the strain-time curves of sintered nanosilver paste at different temperatures, and observed the typical creep behavior. Fig. B.6 shows a strain-time curve of creep of

nanosilver sinter layer at 75 ℃, in which three different states (transient, steady and unstable) can be seen clearly.

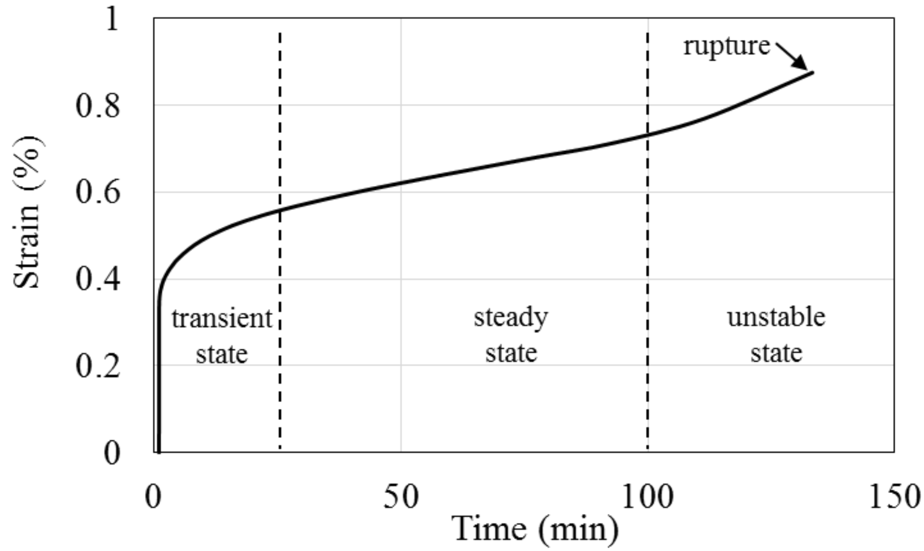

Fig. B.6. Strain-time curve during creep under 10MPa constant stress at 75 ℃

Table B.1: Data from constant stress tension creep tests of sintered nanosilver layers.

T (℃)	1/T (K^{-1})	Steady-state strain rate (sec^{-1})	Rapture time (sec)	Rupture Strain (%)
250	0.001912	5.6E-04	66	4.2
200	0.002114	2.8E-04	36	1.5
150	0.002364	2.0E-05	740	2.3
100	0.002681	6.5E-07	5514	0.8
75	0.002874	3.8E-07	7940	0.87

Table B.1 shows the data of creep tests for sintered nanosilver layers. It indicates that under a constant tensile stress, the steady-state strain rate and rupture strain generally increase with increasing temperature, while the rupture time decreases with increasing temperature. The activation energy of creep for the sintered nanosilver pastes can be also estimated by fitting the data using the equation below:

$$\dot{\varepsilon}_{ss} = A_1 \sigma^n e^{-\frac{Q_c}{RT}} \quad \text{(Eq. B.1)}$$

Where $\dot{\varepsilon}_{ss}$ is the steady-state strain rate; σ is the applied stress; Q_c is the activation energy for creep; T is the absolute temperature; R is gas constant; A_1 and n are fitting parameters.

The fitting curve is shown in Fig. B.7. The activation energy of sintered nanosilver paste for creep is roughly estimated to be 70 KJ/mol, which is higher than conventional solders (about 40-50 KJ/mol). The creep testing result indicates that the sintered silver paste has a higher creep resistance than conventional solders.

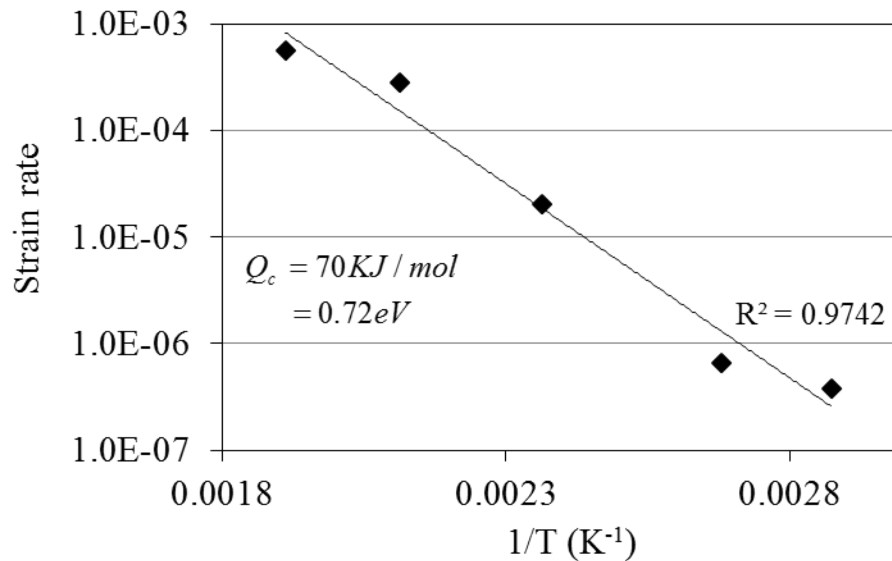

Fig. B.7. Curve fitting for determining the activation energy of sintered silver layer.

Conclusions

Both uniaxial tension tests and constant stress creep tests for sintered nanosilver paste were carried out. The tension tests of sintered paste reveal that the mechanical behavior is strongly dependent on temperature. Young's modulus and ultimate stress decrease with

increasing temperature, and the ultimate strain increases with increasing temperature. Compared with the mechanical properties in room temperature, the Young's modulus and ultimate stress decrease about 80% and 70% respectively at 200 ℃. And the ultimate strain at 200 ℃ increases approximately 200%. The creep test shows that under a constant tensile stress, both the steady-state strain rate and ultimate rupture strain increase with increasing temperature, while the rupture time decreases with increasing temperature. The activation energy of creep for the sintered nanosilver layer is estimated to be 70 KJ/mol, which is higher than the conventional solders. These experimental results can provide a better understanding in the mechanical behavior of sintered nanosilver paste at different temperatures and can be used in modeling of numerical simulations.

Appendix C: Nondestructive characterization of the bonding of silicon device attachments by curvature measurement

The bonding strength of device attachment can be evaluated by die-shear test. However, die-shearing is a destructive characterization technique, which is not a cost-saving method for the bonding characterization. Furthermore, as the silicon devices become thinner and thinner in today's improving technologies, it is hard to take the die-shear test for a silicon device attachment with the thickness less than 100 μm, especially for large area chip attachments (i.e., >100 mm^2). Therefore, new characterization technique for bonding evaluation is demanded. In this topic, a nondestructive characterization of the device attachments bonding by curvature measurement was demonstrated.

Theory

The rationale for using the device curvature as a metric for bond strength is shown below. Because of the existence of a mismatch between the coefficients of thermal expansion (CTE) of the silicon chip and DBC substrate, a sintered sample would develop a curvature after sintering. If the adjacent layers of the sample are perfectly bonded, the ideal curvature of the sample can be determined just by the material properties themselves. According to C.H. Hsueh's model, (C.H. Hsueh, "Modeling of elastic deformation of multilayers due to residual stresses and external bending," Journal of Applied Physics, vol. 91, pp. 9652-9656, 2002.), the theoretical curvature of a perfect bonded chip attachment can be calculated by knowing the initial and final temperatures, Young's modulus, coefficient of thermal expansion, and thickness of each layer. Below is a mathematica code to calculate the theoretical curvature by inputting the mechanical

properties and geometric dimensions of each layer of materials. The input parameters in the demonstration are from a structure of silicon chip bonded on DBC substrate by nanosilver joint, as shown in Fig. C.1.

```
(* parameters input here *)
M = 0; (*external moment *)
T1 = 275;
T2 = 25;
Es = 120 000 000 000; (* copper with 12 mil *)
EE1 = 300 000 000 000; (* Al2O3 with 15 mil *)
EE2 = 120 000 000 000; (* copper with 12 mil *)
EE3 = 10 000 000 000; (*nano-silver with 15um *)
EE4 = 185 000 000 000; (* silicon with 500um *)
as = 0.0000165; (* copper CTE *)
a1 = 0.0000081; (* Al2O3 CTE *)
a2 = 0.0000165; (* copper CTE *)
a3 = 0.0000189; (* silver CTE *)
a4 = 0.0000026; (* silicon CTE *)
ts = 0.0002;
t1 = 0.00038;
t2 = 0.0002;
t3 = 0.000015;
t4 = 0.0005;
(* no matter how many layers there are,
just input the parameters in Array EE (Young's modulus), t (thickness) and a (CTE) *)
EE = {EE1, EE2, EE3, EE4};
t = {t1, t2, t3, t4};
a = {a1, a2, a3, a4};
```

$$h[i_] := \sum_{j=1}^{i} t[[j]];$$

$$c = \frac{(T2 - T1) * \left(Es * ts * as + \sum_{i=1}^{Dimensions[EE][[1]]} (EE[[i]] * t[[i]] * a[[i]])\right)}{Es * ts + \sum_{i=1}^{Dimensions[EE][[1]]} (EE[[i]] * t[[i]])};$$

$$tb = \frac{-Es * ts * ts + \sum_{i=1}^{Dimensions[EE][[1]]} (EE[[i]] * t[[i]] * (2 * h[i-1] + t[[i]]))}{2 * \left(Es * ts + \sum_{i=1}^{Dimensions[EE][[1]]} (EE[[i]] * t[[i]])\right)};$$

$$k = \left(3 * \left(Es * (c - as * (T2 - T1)) * ts * ts - \sum_{i=1}^{Dimensions[EE][[1]]} (EE[[i]] * t[[i]] * (c - a[[i]] * (T2 - T1)) * (2 * h[i-1] + t[[i]]))\right) + 6 * M\right) \Big/ \left(Es * ts * ts * (2 * ts + 3 * tb) + \sum_{i=1}^{Dimensions[EE][[1]]} (EE[[i]] * t[[i]] * (6 * h[i-1] * h[i-1] + 6 * h[i-1] * t[[i]] + 2 * t[[i]] * t[[i]] - 3 * tb * (2 * h[i-1] + t[[i]])))\right)$$

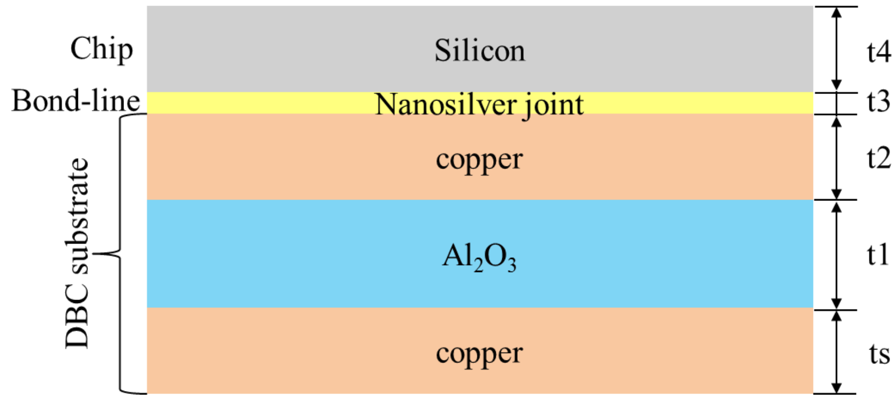

Fig. C.1. Structure of a silicon chip bonded on a DBC substrate.

In real cases, the measured curvature is always lower than the ideal curvature because the interfacial bonding is not perfect. However, the difference between the ideal and real curvatures can still reveal the quality of the bonding: the stronger the bond, the higher the measured curvature, assuming the attachment layer (sintered nanosilver) does not experience internal changes that dissipate the curvature. Obviously, this method will only be useful if the materials being bonded have non similar CTEs and the surfaces being bonded are not further deformed.

Experiments

The test samples consisted of direct bond copper (DBC) substrate and silicon or alumina mechanical chips bonded together with sintered nanosilver paste. The thickness of the copper and alumina layers of DBC were 200 μm and 380 μm, respectively. In lieu of actual devices, 200 μm thick silicon chips and 1000 μm thick alumina chips were used. The DBC substrate had a coating of silver while the chips was coated with a metallization consisting of 150 nm Cr, 200 nm Ni and 250 nm Ag in succession by physical vapor deposition (PVD). The silver coatings were necessary for adhesion to the sintered silver.

The DBC substrates and chips were cut into 14 × 14 mm^2 and 10 × 10 mm^2 pieces, respectively, for sample fabrication. The silicon chip attachments have flat surface, which were be used for curvature measurement, while the alumina chip attachments were thick enough for die-shear testing.

The silver paste attachment layer was deposited as a double print on the DBC substrate. An initial layer of nanosilver paste was printed with a wet print thickness of 50 μm and dried at 180 ℃ for 30 minutes after heating at a ramp rate of 5 ℃/min. The second layer was printed on the dried paste with an estimated wet print thickness of 5 μm. The silicon chip was mounted on the printed paste, and the assembly was heated up with different heating conditions. The fabricated silicon attachments were used to measure the bended curvature, and the fabricated alumina attachments were used to measure the die-shear strength. Two silicon replicates and three alumina replicates were fabricated for each heating condition.

The curvature of the sintered silicon chip attachment surface was measured with a Dektak 150 profilometer, and die-shear strength of the alumina chip attachment was measured with a ComTen 95 tensile tester. The fabrication process conditions with measured curvature or die-shear strength are shown in Table C.1.

Table C.1: Curvature of silicon attachments and die-shear strength of alumina attachments with different fabricating process parameters.

Drying time (min)	Drying pressure (MPa)	Sintering time (min)	Sintering pressure (MPa)	Curvature (m^{-1})		Die-shear strength (MPa)		
1	0	30	0	0.34	0.29	5.3	16.5	11.3
5	0	30	3	0.90	0.88	30.1	31.1	31.6
1	3	30	3	0.82	0.88	32.8	39.0	30.4

5	3	30	0	0.92	0.73	33.6	35.6	34.2
1	0	10	3	0.95	0.40	25.0	11.2	14
5	0	10	0	0.39	0.34	6.6	5.1	4.7
1	3	10	0	0.91	0.43	5.6	19.9	10.7
5	3	10	3	0.57	0.93	35.5	39.9	32.1

The theoretical calculated curvature is 2.25 m^{-1} for the given materials properties. All the measured curvatures were smaller than the theoretical calculated curvature. It is likely that the actual samples did not achieve the infinite bonding between the material layers such that the resulting curvature is lower than the ideal or theoretical value. Nevertheless, it should not detract from the utility of the curvature measurement technique as a nondestructive method for evaluating the bond quality achieved with the sintered nanosilver paste. It should be just a matter of properly calibrating the technique against some baseline measurements.

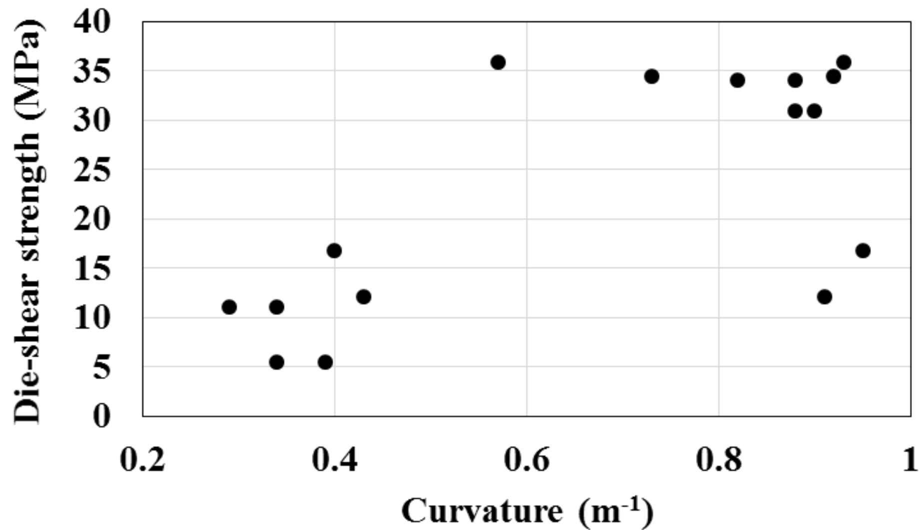

Fig. C.2. Correlation of curvature with die-shear strength.

The plot of measured curvature versus die-shear strength is shown in Fig. C.2. Since the correlation of curvature and die-shear strength was not from the same samples, we were not able to obtain an exact strength-curvature relationship. However, despite a few exceptions, the relationship between the curvature and strength is still obvious. It can be concluded that the die-shear strength increases with increasing the curvature. For the experimental sample configuration, a curvature above 0.5 m^{-1} is required for a strong bonding quality with the die-shear strength of 30-40 MPa.